Universität Potsdam
Mathematisch-Naturwissenschaftliche Fakultät
Institut für Physik und Astronomie
Ultraschnelle Dynamik in kondensierter Materie

Polyelectrolyte Multilayers for Plasmonics and Picosecond Ultrasonics

Dissertation

zur Erlangung des akademischen Grades
doctor rerum naturalium
(Dr. rer. nat.)
in der Wissenschaftsdisziplin: Experimentalphysik

eingereicht an der
Mathematisch-Naturwissenschaftlichen Fakultät
der Universität Potsdam

von
Steffen Mitzscherling
geboren am 05.11.1983 in Berlin

Gutachter: Prof. Dr. Matias Bargheer
              Prof. Dr. Svetlana Santer
              Prof. Dr. Andreas Fery

Februar 2015

Abstract

This thesis investigates the application of polyelectrolyte multilayers in plasmonics and picosecond acoustics. The observed samples were fabricated by the spin-assisted layer-by-layer deposition technique that allowed a precise tuning of layer thickness in the range of few nanometers.

The first field of interest deals with the interaction of light-induced localized surface plasmons (LSP) of rod-shaped gold nanoparticles with the particles' environment. The environment consists of an air phase and a phase of polyelectrolytes, whose ratio affects the spectral position of the LSP resonance.
Measured UV-VIS spectra showed the shift of the LSP absorption peak as a function of the cover layer thickness of the particles. The data are modeled using an average dielectric function instead of the dielectric functions of air and polyelectrolytes. In addition using a measured dielectric function of the gold nanoparticles, the position of the LSP absorption peak could be simulated with good agreement to the data. The analytic model helps to understand the optical properties of metal nanoparticles in an inhomogeneous environment.

The second part of this work discusses the applicability of PAzo/PAH and dye-doped PSS/PAH polyelectrolyte multilayers as transducers to generate hypersound pulses. The generated strain pulses were detected by time-domain Brillouin scattering (TDBS) using a pump-probe laser setup. Transducer layers made of polyelectrolytes were compared qualitatively to common aluminum transducers in terms of measured TDBS signal amplitude, degradation due to laser excitation, and sample preparation.
The measurements proved that fast and easy prepared polyelectrolyte transducers provided stronger TDBS signals than the aluminum transducer. AFM topography measurements showed a degradation of the polyelectrolyte structures, especially for the PAzo/PAH sample.
To quantify the induced strain, optical barriers were introduced to separate the transducer material from the medium of the hypersound propagation. Difficulties in the sample preparation prohibited a reliable quantification. But the experiments showed that a coating with transparent polyelectrolytes increases the efficiency of aluminum transducers and modifies the excited phonon distribution.
The adoption of polyelectrolytes to the scientific field of picosecond acoustics enables a cheap and fast fabrication of transducer layers on most surfaces. In contrast to aluminum layers the polyelectrolytes are transparent over a wide spectral range. Thus, the strain modulation can be probed from surface and back.

Zusammenfassung

Diese Doktorarbeit behandelt die Verwendung von Multischichtsystemen aus Polyelektrolyten in den Fachgebieten der Plasmonik und der Pikosekunden-Akustik. Die verwendeten Proben wurden mit dem Spincoater-gestützten Layer-by-Layer-Verfahren hergestellt. Diese Methode ermöglichte die Einstellung Schichtdicke mit einer Präzision von wenigen Nanometern.

Im Bereich der Plasmonik wurde die Wechselwirkung von Oberflächenplasmonen stabförmiger Gold-Nanopartikel mit deren Umgebung untersucht. Diese Umgebung bestand aus zwei Phasen: Polyelektrolyte und Luft. Das Volumenverhältnis der Materialien bestimmte die spektrale Position des Oberflächenplasmons.
Bei zunehmender Einbettung der Goldpartikel zeigten die gemessenen UV-VIS Spektren eine Rotverschiebung der Plasmonenabsorption. Es wurde ein Modell entwickelt, das die inhomogene Umgebung der Partikel durch eine mittlere dieelekrische Funktion beschreibt. Nachdem die dielektrische Funktion der Goldpartikel in separaten Messungen bestimmt waren, konnte die Lage der Plasmonenabsorption berechnet werden. Die Berechnungen stimmten dabei mit den Messwerten überein.
Mit diesem analytischen Modell ist es möglich, die optischen Eigenschaften von metallischen Nanopartikeln in einer inhomogenene Umgebung zu verstehen.

Der zweite Teil dieser Arbeit diskutiert die Anwendbarkeit von polyelektrolytischen Multischichten aus PAzo/PAH bzw. Porphyrin-dotiertem PSS/PAH für die Erzeugung von Hyperschallpulsen. Die erzeugten Schallpulse wurden durch zeitaufgelöste Brillouin-Streuung in einem sogenannten pump-probe Aufbau detektiert. Schallerzeugende Schichten aus Polyelektrolyten wurden mit Wandlern aus Aluminium verglichen.
Die Messungen zeigten, dass die Polyelektrolyte sehr gut für die Erzeugung von Schallpulsen geeignet sind. Der einfachen Probenpräparation und der guten Effizienz steht jedoch eine geringe Zerstörschwelle gegenüber. AFM-Messungen zeigten besonders bei den PAzo/PAH Multischichten sehr starke Veränderungen in der Struktur.
Eine Quantisierung der induzierten Schallamplitude sollte durch eine optische Trennung von Wandler und Propagationmedium erreicht werden. Da die Trennschichten auch eine akustische Abkopplung bewirkten, ließen sich die Schallamplituden nicht bestimmen. Es wurde jedoch festgestellt, dass sich die Effizienz eines Aluminium-Wandlers durch das Aufbringen transparenter Polyelektrolytschichten deutlich steigern lässt.
Die Herstellung von Ultraschall-Wandlern aus Polyelektrolyten erweitert die Möglichkeiten der Pikosekunden-Akustik. Zum einen können diese Wandler schnell und kostengünstig direkt auf fast jeder Oberfläche aufgebracht werden. Zum anderen sind Polyelektrolyte in einem breiten Spektralbereich transparent. Das ermöglicht Messungen von der Vorderseite, die bei herkömmlichen Aluminium-Wandlern nicht oder nur schwer realisierbar sind.

Contents

Contents

1 Introduction

During the second half of the 20th century, artificial structures became smaller and smaller. In the 1980ies the size limit of 100 nanometer was undercut, marking the birth of nanotechnology [1]. This work focuses on structures of less than 100 nanometer size. In this range, the ratio of surface and volume is several orders of magnitude larger compared to macroscopic objects. Thus, the physical properties are dominated by the surface [2]. Especially nanoparticles of noble metals can catalyze chemical reactions [3, 4]. The strong electric fields at the particles' surfaces provide surface-enhanced Raman spectroscopy [5]. Very recently, gold nanostars were simultaneously used to catalyze a chemical reaction and detect the products [6].

Another exceptional property of metal nanoparticles is the so-called localized surface plasmon. Since the particles are smaller than the wavelength of visible light, the electron gas within the particle follows the external electromagnetic field. In resonance, a strong absorption occurs, that exceeds the absorption of bulk metal. The spectral position is well-defined and sharp. It depends on size and shape of the particle and can be tuned by changing the environment. For spherical gold nanoparticles, the localized surface plasmon resonance (LSPR) is located in the range of $500\,\mathrm{nm}$. These particles can be easily excited and heated with green lasers, enabling medical applications as drug delivery [7, 8, 9] and treatment of cancer cells [10, 11].

The research on interfaces is another focus of nanoscience. By modifying the surface, characteristics of the initial material can be changed. Examples are the growth of nanostructures, providing hydrophobicity [12, 13, 14], changing the surface charge [15] or reactivity [16, 17], and influence the biocompatibility of implants [18, 19]. The desired properties are achieved by structuring the surface or adsorption of functional materials.

In 2007, the work group *ultrafast dynamics of condensed matter* (UDKM) of Potsdam University started the research on nanostructures with incorporated gold nanoparticles, driven by a cooperation with the *Max Planck Institute of Colloids and Interfaces*. All nanostructures were fabricated by the versatile method of layer-by-layer (LbL) deposition, first introduced by Decher et al. [15]. The dip-coating method was replaced by the much faster spin-assisted LbL technique. Both methods produce well-stratified multilayers of polyelectrolytes with an accuracy of few nanometers [20, 21]. By adjusting the thickness of the polyelectrolyte spacer between adjacent layers of gold nanoparticles, the particle interaction could be measured as a function of distance [22]. Sequentially embedding of spherical particles into transparent polymer results in a red shift of the strong LSPR absorption peak. This peak shift can be explained by the change of the dielectric environment. It is predictable by effective medium theories, but all theories demand a homogeneous environment of

the particles.

Another field of UDKM's research is the generation, detection, and simulation of hypersound strain waves. Samples, usually made of crystalline perovskites structures such as SRO or LSMO, were analyzed via time-domain Brillouin scattering (TDBS) experiments. Basing on the accumulated experience and expertise with polyelectrolyte multilayers, this work first reproduced such TDBS experiments with non-crystalline polyelectrolyte samples. Therefore, the azobenzene-containing polyelectrolyte PAzo was introduced.

The cis-trans-isomerization of azobenzene due to light absorption was first described in 1937 [23]. During the second half of the 20th century, there was a wide field of research to apply azobenenes as molecular switch [24, 25, 26], for data storage [24, 27, 28], surface reliefs [29] and other applications [30, 31]. Within the last two decades the upcoming ultrafast laser technology gave us the possibility to study the switching process on ultrashort timescales [32]. In solution, the isomerization occurs within one picosecond [32]. This ultrafast switching process raised the question whether azo molecules are more effective for strain generation than other molecules. The generation of strain by ultrafast excitation of thin films of polymers was first reported by Vardeny in 1988 [33], and continued by others [34, 35].

This work treats two topics: The interaction of gold nanoparticles with their surrounding medium and picosecond acoustics. Both topics are different, but connected via the application of LbL technique for sample preparation. This work is structured as follows:

Chapter 2 explains the origin of the strong LSPR of gold nanoparticles and introduces the Maxwell-Garnett effective medium theory. This chapter also explains Brillouin scattering that is utilized for the detection of hypersound strain waves. The fabrication and characterization of samples are illustrated in chapters 3 and 4, respectively. Chapter 5 introduces a model that explains the optical properties of partially embedded particles. The dielectric functions of polyelectrolytes and air are replaced by an average function. Since the LSPR shift is much stronger for elongated particles than for spheres, we studied gold nanorods. Chapter 6 discusses the mechanical switching of azo-groups by comparing azo-containing polymer layers with other thin films made of polyelectrolytes or aluminum, respectively. The powerful layer-by-layer technique is used once more to tailor acoustic actuators with high precision.

2 Theoretical Background

2.1 Dielectric Function

The polarization and dissipation of electromagnetic waves in a medium are characterized by the dielectric function ϵ. If ϵ is known, one can calculate optical properties such as absorption and reflection spectra of this material. The key to deriving the dielectric function is the electronic polarization density $P(\omega) = \epsilon_0 \chi E(\omega)$ that is connected with the external electric field E by the susceptibility χ. This χ defines the dielectric function by a simple addition $\epsilon = 1 + \chi$.

The theoretical approach to explain the electronic system of a material starts with a harmonic oscillator model. This model describes the motion of electrons in an oscillating external electric field. The origin of the complex refractive index and dielectric function are explained by this model.

The first step to derive the polarization density is to calculate the displacement of electrons due to the external electric field E. The equation of motion of the electrons is

$$m_e \frac{\delta^2 x}{\delta t^2} + m_e \Gamma \frac{\delta x}{\delta t} + ax = eE e^{-i\omega t} \tag{2.1}$$

with electron mass m_e and scattering rate Γ. The term $a \cdot x$ describes the restoring force with displacement x and linear force constant a. The constant a defines the eigenfrequency $\omega_0 = a/m_e$ at which the system is excited in resonance. The solution of equation 2.1 is

$$x(\omega) = \frac{-e/m_e}{\omega^2 - i\omega\Gamma} E(\omega) \tag{2.2}$$

Multiplication by e leads to the induced dipole moment $p(\omega) = -ex(\omega)$. It defines the total polarization density $P(\omega) = n_e p(\omega)$ and results in

$$P(\omega) = n_e \frac{-e^2/m_e}{\omega^2 - i\omega\Gamma} E(\omega) \tag{2.3}$$

The dielectric function is related to this induced polarization density by $P = \epsilon_0(\epsilon - 1)E(\omega)$. Real and imaginary parts are

$$\epsilon_r = 1 + \omega_p^2 \frac{(\omega_0^2 - \omega^2)}{(\omega_0^2 - \omega^2)^2 + \omega^2 \Gamma^2} \quad \text{and} \tag{2.4a}$$

$$\epsilon_i = -\omega_p^2 \frac{\omega\Gamma}{(\omega_0^2 - \omega^2)^2 + \omega^2 \Gamma^2} \quad , \tag{2.4b}$$

where $\omega_p^2 = n_e e^2/\epsilon_0 m_e$ is the squared plasma frequency of the material. Figure 2.1a shows a plot of equation 2.4. The imaginary part ϵ_i is located at ω_0. It has the shape of a Lorentz distribution function.

(a) (b)
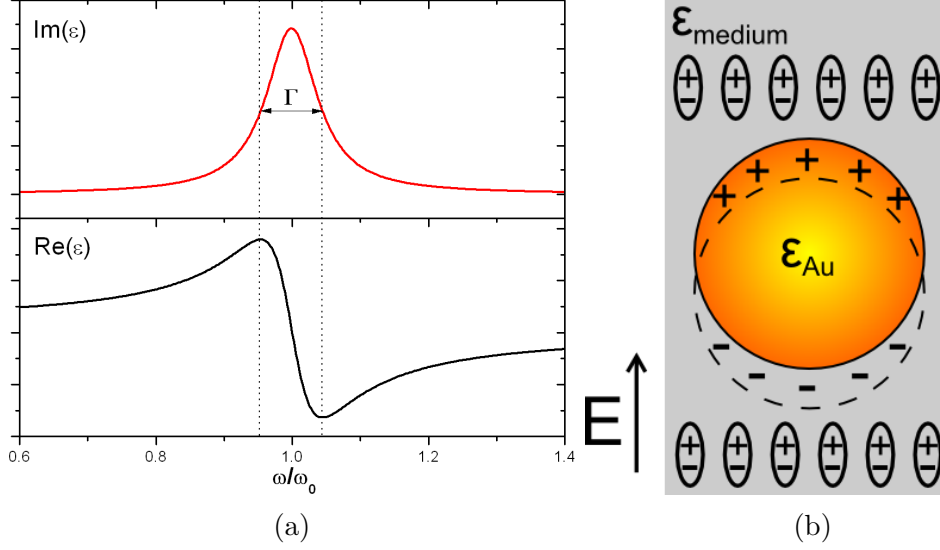
Figure 2.1: Real and imaginary part of the dielectric function of a harmonic os-
cillator (a). The plot is based on equations 2.4. Figure b) shows the
electron displacement in a metal nanoparticle due to an external elec-
tric field. The resonant oscillation of these electrons is called localized
surface plasmon.

In case of more than one absorption mechanism, the total susceptibility is the sum
of all contributions. For bulk gold, there are two mechanisms: The intraband ab-
sorption and the interband excitation. This results in $\epsilon = 1 + \chi_{IB} + \chi_{DS}$. The next
two paragraphs explain both mechanisms in detail.

Intraband Contribution in Bulk Gold   The excitation of free electrons within the
conduction band is described by the intraband susceptibility. In contrast to equation
2.1, there is no Coulomb restoring force for electrons in bulk noble metal. The force
constant a and therefore the eigenfrequency is zero. With these conditions, equation
2.4 shortens to

$$\epsilon_r = 1 - \omega_p^2 \frac{1}{(\omega^2 + \Gamma^2)} \quad \text{and} \tag{2.5a}$$

$$\epsilon_i = -\omega_p^2 \frac{\Gamma}{\omega(\omega^2 + \Gamma^2)} \quad . \tag{2.5b}$$

Both equations exhibit a resonance at $\omega = 0$. This contribution to the bulk metal
dielectric function is called Drude part. To consider the influence of the ionic lattice
on the conduction electrons, the effective electron mass m_{eff} can be used instead of
m_e. The imaginary part of the dielectric function is proportional to ω and hence,
the Drude absorption dominates in the infrared spectral range where ω is low.

Interband Contribution   The transition of electrons from the filled d-band to the
partly filled sp-band of bulk gold is called interband excitation. Band structure
calculations from Guerrisi et al. are shown in figures 2.2a and 2.2b. The calculated
dielectric function and experimentally derived values from Johnson and Christy

(a) Band structure (X) (b) Band structure (L) (c) Dielectric function
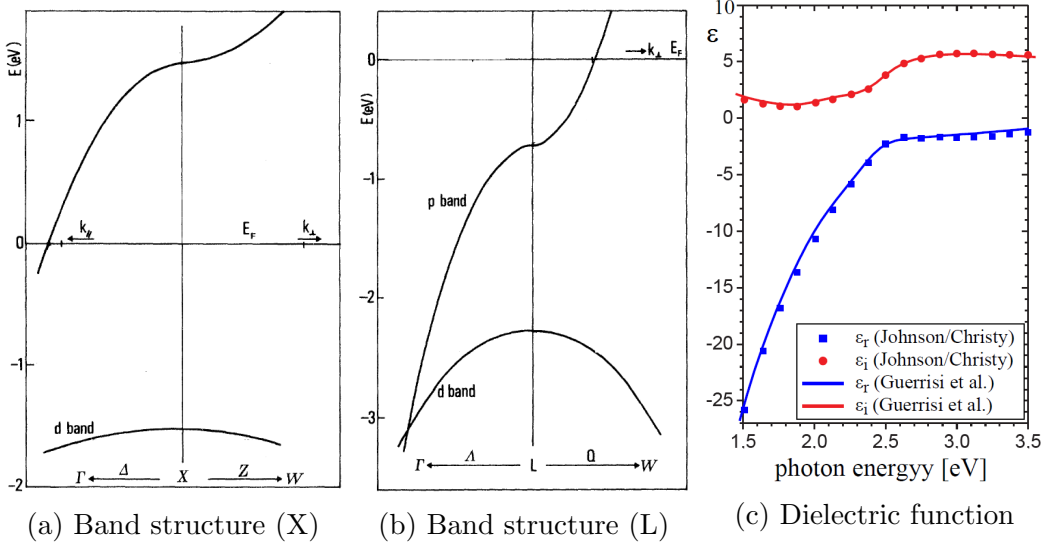
Figure 2.2: Band structure of bulk gold, calculated by Winsemius et al at X-point (a) and L-point (b) of the Brillouin zone (modified after reference [36]). The calculated dielectric function is plotted as solid line in (c). The data points were measured by Johnson and Christy [37].

are plotted in figure 2.2c [36, 37]. Below 2 eV, the Drude intraband absorption of bulk gold contributes to the dielectric function whereas above 2.2 eV the interband transitions dominate.

Dielectric Function of Gold Nanoparticles The size of a nanoparticle is below 100 nm and thereby much smaller than the wavelength of irradiation. The motion of electrons in a gold nanoparticle differs from that in bulk metal. As depicted in figure 2.1b, they can not be assumed as free electrons since restoring coulomb forces bind them to the lattice ions. In other words, the linear force term ax in equation 2.1 is not zero. Consequently, an eigenfrequency ω_0 exists, describing a collective oscillation of the electrons around the fixed lattice ions. This leads to the strong resonant absorption of metal nanoparticles. Aside from this so-called localized surface plasmon resonance (LSPR), the oscillator strength decreases rapidly to zero (see fig. 2.1a) yielding to transparency in the infrared. For higher energies, the surface plasmon absorption changes over to the weaker intraband absorption.

Since gold nanoparticles are much smaller than the wavelength of light, the interaction of this particle with the electromagnetic field can be approximated as a quasi-static problem. The phase of the harmonically oscillating electromagnetic wave is supposed to be constant over the particle volume. This reduces the problem to a particle in an electrostatic field. The harmonic time dependence can be easily added to the static solution. To calculate the electric field $E = -\nabla\Phi$, one has to

11

solve the Laplace equation $\nabla^2 \Phi = 0$. For spherical particles, the potential Φ is [38]

$$\Phi_{in} = -\frac{3\epsilon_m}{\epsilon + 2\epsilon_m} E_0 r \cos\theta \tag{2.6a}$$

$$\Phi_{out} = E_0 r \cos\theta + \frac{\epsilon - \epsilon_m}{\epsilon + 2\epsilon_m} E_0 a^3 \frac{cos\theta}{r^2}. \tag{2.6b}$$

The dielectric functions of particle and medium are ϵ and ϵ_m, respectively and a is the radius of the sphere. The angle θ determined from the axis of the external electric field E_0 and distance r are the spatial coordinates. Equation 2.6b is notable: Φ_{out} specifies the superposition of the external field and the field of a dipole located at the particle center. Introducing the dipole moment p leads to

$$\Phi_{out} = E_0 r \cos\theta + \frac{p \cdot r}{4\pi\epsilon_0\epsilon_m r^3} \tag{2.7a}$$

$$p = 4\pi\epsilon_0\epsilon_m \frac{\epsilon - \epsilon_m}{\epsilon + 2\epsilon_m} E_0. \tag{2.7b}$$

Equation 2.7b shows that the magnitude of the induced dipole moment inside a sphere is proportional to $|E_0|$. Via $p = \epsilon_0\epsilon_m\alpha E_0$ the polarizability can be introduced

$$\alpha = 4\pi a^3 \frac{\epsilon - \epsilon_m}{\epsilon + 2\epsilon_m}. \tag{2.8}$$

Finally, equation 2.8 describes the polarizablility of a sphere of sub-wavelength size in the electrostatic approximation. The resonance term is known from the Clausius-Mossotti relation. It plays a central role in the effective medium theory. Equations 2.4 describe the dielectric function deduced from the harmonically oscillating conduction electrons of the metal. This is valid for a single particle in vacuum, but a more realistic approach takes the surrounding medium into account. Several theories were developed since the beginning of 20th century. All of them treat the particle and its environment as homogeneous effective medium with dielectric function ϵ_{eff}. Good results are obtained, if the included metal particles are much smaller than the investigated wavelength of the light. In this work, the Maxwell-Garnett effective medium theory developed by J.C.M. Garnett is applied. It connects the resonance term given in equation 2.8 with a filling factor f and the dielectric function of the medium ϵ_m:

$$\epsilon_{eff} = \epsilon_m + 3f \cdot \epsilon_m \frac{\epsilon_{particles} - \epsilon_m}{\epsilon_{particles} + 2\epsilon_m}. \tag{2.9}$$

The filling factor is defined as the ratio of particle volume and total sample volume:

$$f = \frac{V_{particles}}{V_{particles} + V_m}. \tag{2.10}$$

The Maxwell-Garnett formula was developed for small filling factors ($f < 10^{-2}$), but experiments proved that it is also applicable to higher values of f [39, 40]. The formula is restricted to spherical particles and disregards their size. In this case, the plasma frequency ω_p is related to ω_0 by

$$\omega_0 = \frac{\omega_p}{\sqrt{1 + 2\epsilon_m}}. \tag{2.11}$$

It describes the position of the absorption peak, depending on the surrounding medium. The change from vacuum to medium results in a red-shifted peak. The surface plasmon absorption changes dramatically, if the shape of the nanoparticle is different. Elongated spheres (spheroids) or nanorods show two absorption peaks: one for the transverse plasmon and one for the oscillation along the length axis (longitudinal plasmon). According to equation 2.8, one would expect a dependence only on the respective dimension of the particle. In fact, the longitudinal plasmon frequency strongly depends on the aspect ratio $R = A/B$ with length A and width $B = C < A$ whereas the transverse plasmon frequency is quite fixed [41, 42, 43]. The depolarization factors P_i explain these effects. They are defined as

$$P_A = \frac{1 - e^2}{e^2} \left[\frac{1}{2e} \ln \left(\frac{1 + e}{1 - e} \right) - 1 \right] \tag{2.12a}$$

$$P_B = P_C = \frac{1 - P_A}{2} \tag{2.12b}$$

with factor $e = \sqrt{1 - R^2}$. Resonant absorption occurs, when the condition

$$\epsilon_{particle} = -\frac{(1 - P_i)\epsilon_m}{P_i} = -u_i \epsilon_m \tag{2.13}$$

is fullfilled [43]. If $\epsilon_{particle}$ and ϵ_m are known, the position of the absorption peak can be determined. The transverse plasmon peak is located around $2.4\,\text{eV}$ ($517\,\text{nm}$) and the longitudinal peak can be observed in a wide range from visible to the near infrared light. With decreasing aspect ratio, the shape factor u_i in equation 2.13 converges to a value of 2. This results in the resonance condition of spherical particles known from equation 2.8. The imaginary part of the particles' dielectric function $Im(\epsilon_{particle})$ determines the intensity of the resonance. The smaller $Im(\epsilon_{particle})$ at the resonance ω is, the closer the denominator value approaches zero and the resonance increases. The scattering rate Γ of equations 2.5a and 2.5b is equal to the linewidth of the resonance. It is connected to the relaxation time τ of the electrons by $\Gamma = 2\pi/\tau$. The relaxation of excited electrons bases on scattering with other electrons (e-e), phonons (e-ph), surfaces (e-sf), and impurities (e-imp). All contributions sum up to $\Gamma = 2\pi \left(\frac{1}{\tau_{e-e}} + \frac{1}{\tau_{e-ph}} + \frac{1}{\tau_{e-sf}} + \frac{1}{\tau_{e-imp}} \right)$.

2.2 Brillouin Scattering

The scattering of light from acoustic phonons is called Brillouin scattering. It can be interpreted as the interaction of light with time-dependent variations of the refractive index. The refactive index can vary due to thermal fluctuation of the lattice, by acoustic modes (phonons), or magnetic modes (magnons) [44]. This work focuses on the interaction of ultrashort light pulses with optically synthesized phonon wave packets. Figure 2.3 a) sketches a typical Brillouin scattering experiment. The transducer layer releases a strain wave that propagates into the medium at speed of sound. These wave packets can be assumed as Bragg grating with lattice constant $d_S = 2\pi v_S/\omega_S$ where v_S is the sound velocity and ω_S is the phonons angular

(a) (b)
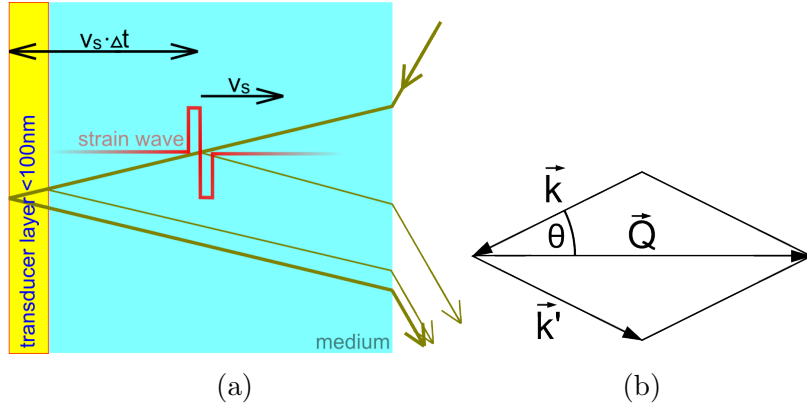
Figure 2.3: Scheme of a Brillouin scattering experiment (a). The excited transducer layer generates a strain pulse that propagates into the substrate at speed of sound. Light scatters from this strain wave and interferes with the reflection from the transducer interfaces. Constructive interference occurs, if the Laue condition (b) is fulfilled.
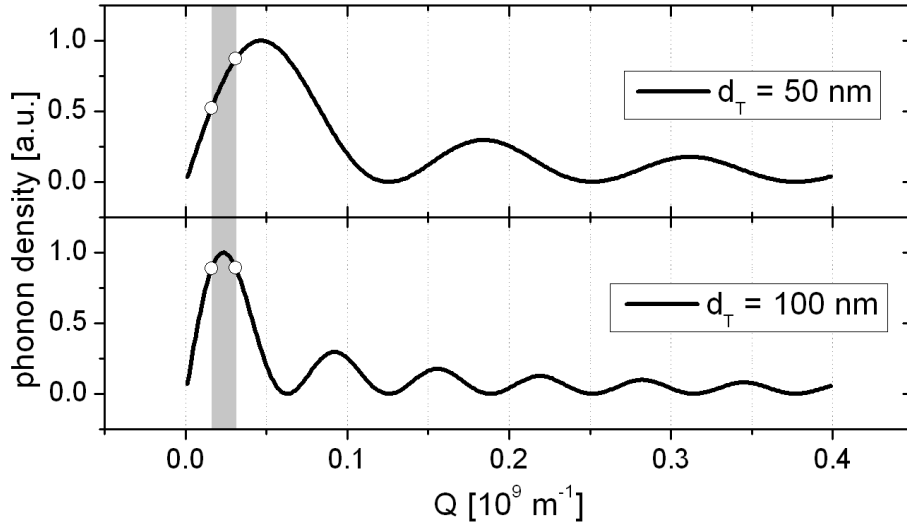
Figure 2.4: Phonon spectra of bipolar strain pulses with lengths of $50\,\text{nm}$ and $100\,\text{nm}$, respectively. The optically accessible range of the phonon spectra is marked by the grey background.

frequency [45]. Optical photons with incident angle θ and wavelength $\lambda_m = \lambda/n(\lambda)$ are diffracted if they fulfill Bragg's law

$$\lambda_m = 2d_S \sin\theta \quad . \tag{2.14}$$

In reciprocal space, the Laue equation is equivalent

$$\vec{Q} = \vec{k}' - \vec{k} \quad . \tag{2.15}$$

It describes the scattering of light with wave vector $\vec{k}$ at a phonon with wave vector $\vec{Q}$. Figure 2.3 b) shows the corresponding vector diagram. In the dimension of phonon propagation, equation 2.15 shortens to $Q = 2k_\parallel$ with $k_\parallel = k\cos\theta$. Using the relation

$$k = \frac{2\pi}{\lambda}n(\lambda) \tag{2.16}$$

results in

$$Q(\lambda) = \frac{4\pi}{\lambda}n(\lambda)\cos\theta \quad . \tag{2.17}$$

This equation calculates the phonon wave vector that can be measured with given angle and probe wavelength.

The Fast Fourier transformation (FFT) of a bipolar strain pulse results in spectral phonon density with an amplitude of

$$A_{FFT} = \frac{4\sin^2\left(\frac{1}{2}d_T Q'\right)}{Q'} \tag{2.18}$$

with wave vector

$$Q'(\lambda) = \frac{4\pi v_S n(\lambda)\cos\beta}{v_T \lambda} = \frac{v_S}{v_T}Q(\lambda) \tag{2.19}$$

Thickness and sound velocity of the transducer are d_T and v_T, respectively, whereas β describes the angle of incident light within the medium. Figure 2.4 exemplifies the phonon spectra for two different transducer thicknesses d_T. The optically accessible range is limited to the first maxima.

According to equations 2.14 and 2.15, a part of the supercontinuum probe pulse scatters from the phonon wave packet. This part interferes with the static reflections from sample interfaces, while the moving sound pulse causes a phase shift. The result is a time-dependent modulation of the reflected intensity with a period of

$$T_S(\lambda) = \frac{\lambda}{2v_S n(\lambda)\cos\theta}. \tag{2.20}$$

Such time resolved measurements are shown in chapter 6.

3 Experimental Methods I: Sample Preparation

In this work several nanolayered structures are discussed. Most of them are made of polymers, some contain gold nanoparticles, and some consist of a thin metal film. All of them are self-made in our laboratories using different methods. This chapter introduces the employed materials, gives theoretical background for sample preparation techniques, and explains the steps from making-off to the characterization of a new sample.

3.1 Materials

3.1.1 Polyelectrolytes

The different types of polyelectrolytes employed in this work, are listed in table 3.1 and schematically shown in figure 3.1. They are purchased from Sigma-Aldrich (Germany) and used without any further treatment, if not pointed out different. Poly(ethyleneimine)(PEI) is a polymer with 1500 repetition units. The monomer molar mass is 474.75 g/mol. Due to its branched structure PEI easily adsorbs on smooth surfaces providing a homogeneous distribution of surface charges. Therefore it is used as first layer on cleaned substrates. In water the protonation of amino side groups yields a positive surface charge. Poly(allylamine hydrochloride)(PAH) is a linear polyelectrolyte. The molar mass of a monomer is 93.56 g/mol. In aqueous solution it is positively charged. Poly(sodium 4-styrenesulfonate)(PSS) is an anionic polyelectrolyte with monomer molar mass of 206.19 g/mol. Before application, it was dialyzed to remove PSS fragments with few repetition units. By this treatment, the color of the PSS flakes turns from yellowish to white. Poly[1-[4-(3-carboxy-4-hydroxyphenylazo) benzenesulfonamido]-1,2-ethanediyl, sodium salt](PAzo) is an anionic polyelectrolyte containing azobenzene side chains. Therefore, it absorbs light in the near UV. The molar mass of a monomer is 369.33 g/mol.

Polyelectrolyte	Abbreviation	M_w [kDa]	charge
Poly(ethyleneimine)	PEI	750	positive
Poly(allylamine hydrochloride)	PAH	58	positive
Poly(sodium 4-styrenesulfonate)	PSS	70	negative
Poly[1-[4-(3-carboxy-4-hydroxyphenylazo) benzenesulfonamido]-1,2-ethanediyl, sodium salt]	PAzo	n/a	negative

Table 3.1: List of polyelectrolytes that were used for sample preparation
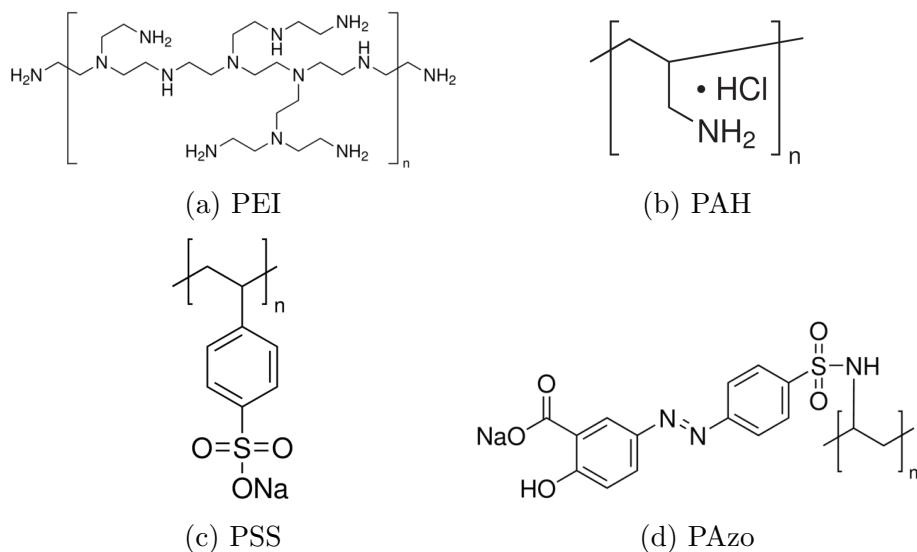
(a) PEI

(b) PAH

(c) PSS

(d) PAzo

Figure 3.1: Molecular structure of polyelectrolytes

3.1.2 Gold Nanoparticles

Gold nanoparticles have been used much longer than they are known. Since many centuries they give a bright red color to church windows. But the reason for that color differing so much from bulk gold was not understood till the beginning of the 20th century [46]. In this work, two types of particles are considered: gold nanospheres (GNSs) and gold nanorods (GNRs).

Gold Nanospheres Spherical gold nanoparticles can be produced by the wet-chemical reduction of hydrogentetrachloroaurate ($HAuCl_4$) with trisodium citrate [47]. Solution of $HAuCl_4$ ($c = 0.005\%$ wt.) is heated to the boiling point. When citrate solution is added under continuous stirring, the color of the mixture turns to blue, indicating a nucleation of gold atoms. After several minutes, monodisperse particles are formed and the color turns to dark red. The particle size depends on the amount of the sodium citrate. A higher concentration yields to a decrease of particle size [48, 49]. This procedure was first proposed by Hausner and Lynn in 1940 [47] and realized some years later by Turkevich et al. [50]. With slight modifications, it is still in use.

For this work, suspensions of GNSs were purchased from Sigma-Aldrich and BBI Solutions. Particles from Sigma-Aldrich were used as received. In pretests, some particles from BBI Solutions did not adsorb to our multilayer films. This problem could be solved by adding $0.01\,M$ of HCl. The lower pH value causes more protonations of the NH_2-groups [51]. Thus, the electrostatic attraction between the NH_2-groups of the PAH and the COOH-groups of the gold particle shell is enhanced.

Gold Nanorods Gold nanorods employed in this work were self-fabricated using a slighty modified seeded growth method reported by Sau and Murphy [52]. For the preparation of GNRs, a seed solution is necessary. It consists of a mixture of aqueous $HAuCl_4$ solution and cetyl trimethylammonium bromide (CTAB) to which

solution of $NaBH_4$ is added. The growth solution is a mixture of aqueous solutions of $HAuCl_4$, $AgNO_3$, and CTAB to that ascorbic acid and HCl are added sequentially. Finally, seed and growth solutions are mixed and the particles grow within several hours. Depending on the amount of chemical reagents, the wavelength of longitudinal plasmon resonance varies between 840 nm and 768 nm. To gain particles with absorption at lower wavelength, the aspect ratio has to be decreased. Therefore, glutathione is selectively bound to the ends of the GNRs. Exposed to growth solution, the particles grow in thickness whereas the glutathione prevents the growth in length. All particles are stabilized by a shell of the surfactant CTAB. To make the particles applicable to layer-by-layer deposition, a treatment with PSS is necessary. Therefore, the same amount of PSS solution ($c_{wt} = 0.2\%$, 0.01 M NaCl) is added dropwise to the continuously stirred GNR suspension. Afterwards, free CTAB and PSS molecules have to be removed by centrifugation. After 15 minutes at 8000 rpm ($\approx 10^4 g$), the PSS-covered particles and the remaining solution are separated. The clear solution is replaced with purified water. After a second centrifugation step, the solution has to be removed. The remaining highly concentrated GNRs are re-dispersed in 0.2 M NaCl solution. The final solution has to be stored at 4°C.

3.1.3 Substrates

The construction of nanostructures has high demands on the substrate. The surface roughness has to be lower than several nanometers. The material should be transparent for spectroscopy and conductive for scanning electron microscope (SEM) measurements.

Substrates for Optical Measurements The requirements for optical applications are best fulfilled by fused silica substrates. This glass is made of pure SiO_2 by melting quartz and recooling it in an amorphous structure. The absence of additives leads to excellent transmission in UV-VIS range from 300 nm to 2000 nm. Polished discs of fused silica were purchased from TedPella Inc. (USA). Measurements with AFM show very smooth surfaces on a nanometer scale. The discs have a size of 1 inch in diameter and a thickness of $^1/_8$ inch. Thinner substrates are not practicable. To avoid interference effects or a diluted signal, it is necessary to block backside's reflex for most reflectivity measurements. For an incident angle of 60°, this can be easily done by knife edge or iris diaphragm, if the sample is not too thin.
Since fused silica is non-conductive, it is inappropriate for high-resolution SEM measurements.

Substrates for SEM Measurements For SEM measurements mainly silicon wavers were used as substrate. Old mirrors from the optic labs also fulfill both requirements of conductivity and planarity. If SEM and optical measurements are demanded, a glass slide with a layer of indium tin oxide (ITO) can be used. But here, the substrate surface is scaly.

3.2 Sample Preparation

3.2.1 Polyelectrolyte Multilayer Structures

Structures composed of individual layers are called multilayers. Depending on the material, the layers may be stratified - as it is the case for most of the samples in this work - the layers penetrate each other on a length scale of about 10 nm [20]. The binding forces between the layers are caused by different effects. Hydrogen bonding, van der Waals interaction, $\pi - \pi$ bonding and donor-acceptor bonding are weak interaction forces. Multilayers are more stable, if the layers bind by strong coulomb forces. This is the case for polyelectrolytes that are used in this work. These molecules combine the structure of a polymer with the electrostatic properties of an electrolyte. They consist of a linear or cross-linked hydrocarbon backbone and different, charged side chains. Polyelectrolytes are composed of identical repetition units, each carrying a positive or negative charge if dissociated in water. In aqueous solution, some side chains release an ion by an entropy driven process. The rate of released ions depends on the pH value and can be influenced by adding hydrochloric acid (HCl) or sodium hydroxide (NaOH) [51]. The remaining counterpart is a charged polyelectrolyte that easily attaches to an oppositely charged surface. The alternating assembly of single layers of polyanions and polycations is known as layer-by-layer technique (LbL). This powerful method is well-known for many years. It started with the work of Iler in the 1960s, who built multilayers of charged colloidal particles [53]. Later on, single molecules and finally polyelectrolytes were applied [54, 15]. The simplicity of this method and the possibility to fabricate very smooth layers with tunable layer thickness on nanometer scale attracted broad interest. The number of publications concerning LbL technique rose from 2 in 1993 to 304 in 2014 (see fig. 3.2)[1]. New deposition methods were developed and the influence of fabrication parameters was studied.
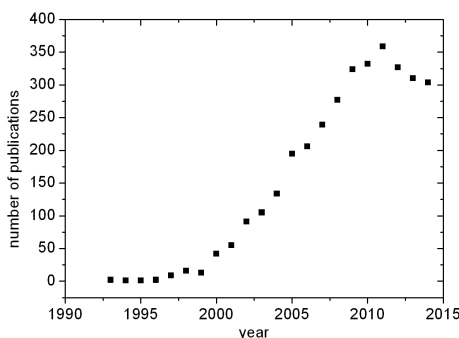
Figure 3.2: Number of publications concerning layer-by-layer deposition of polyelectrolytes during the last years.

When UDKM group started research in nanolayered structures, first samples were prepared by the dip-coating method. Since this is rather slow we switched to spin-assisted LbL technique (see 3.2.3). Another common method is spray-coating. The physical process is the same for all three cases and can be explained by competitive ion pairing [55].

---

[1]Found in web of knowledge database (www.webofknowledge.com) on 6th January 2015.

Schlenoff et al. reported that the binding energy is proportional to the number of released water molecules [56]. These water molecules form a hydration shell around polyelectrolyte in solution. Since every segment of the polyelectrolyte carries one charge, the resulting multilayer systems is very robust.

Figure 3.3: This scheme represents the adsorption of charged polyelectrolytes (PE) to an oppositely charged surface. The screening of charges by counter ions plays an important role for the layer-by-layer deposition technique. Pictures (a) and (b) show the attachment of a negative charged PE. In (c) the counter ions are solved in pure water and washed away. Pictures (d) to (f) show the same process for the next layer of an oppositely charged PE.

Influence of NaCl to Layer Growth   The growth of polyelectrolyte multilayers is depicted in figure 3.3. It considers aqueous solutions of the respective polyelectrolyte and its counterions (Na^+ or Cl^-). Some surface charges on the polymer chain are screened by these counter ions, s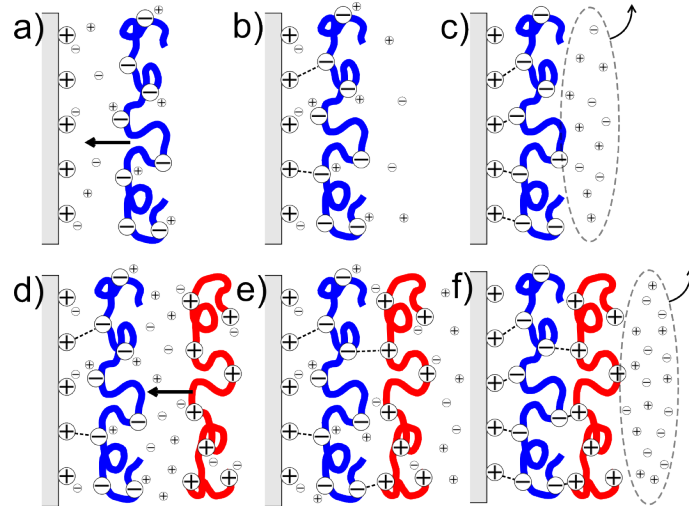o it binds weakly to an oppositely charged surface. Rinsing with pure water releases the ions. This increases the degrees of freedom and therefore the entropy rises. Finally, the counter ions are washed away and the molecule binds to the surface.

This process runs slightly different, if sodium chloride (NaCl) is added to the aqueous solution of polyelectrolytes. The presence of small ions (Na^+, Cl^-) results in a complete screening of the molecules and many free counter ions. If the solution is exposed to an oppositely charged surface, the counter ions attach to it and the molecules adsorb by strong coulomb interaction between the screening ions. Rinsing with pure water results in an increase of entropy as described before. Lvov et al. demonstrated that adding NaCl to the polyelectrolyte solutions improves the adsorbing process. Thereby, the amount of NaCl is secondary as long as the concentration of NaCl reaches the critical limit [57, 58].

Thickness of PE Multilayers   In this work, the smallest repetition unit in a multilayer sample consists of one layer of polyanions (PSS) and one layer of polykations

(PAH or PAzo, respectively). In the further course of this work, such a unit will be considered as one double layer (DL). The thickness of a typical double layer is 2.5 nm for PSS/PAH and 4.5 nm for PSS/PAzo, both confirmed with AFM, ellipsometry, and X-ray reflectivity measurements [59]. Due to self healing effect of layer defects, there is no limit to the layer number [59]. We fabricated samples of several hundred DLs and multilayer systems of more than 1000 layers were reported [60].

Applications of PE Multilayers   Layers of polyelectrolytes are interesting for many applications. They are used as functional surface coatings [61], for biomedical devices as implantates [62, 63] or drug delivery [64, 65], antireflective coatings [66] or Bragg-reflectors [67], and many more [68, 69].

A broad field of literature reports on embedded nanosized objects such as metal nanoparticles, core-shell particles or quantum dots. This technique is also used for organic objects like proteins, DNA, and charged viruses.

This work investigates the applicability of polyelectrolytes as optomechanical transducer for hypersound experiments, treated in chapter 6.

Multilayers of PSS/PAH are also suitable to embed gold nanoparticles. The particles bind to the polyelectrolytes by coulomb interaction. Additional layers of polyelectrolytes cover the particles until they are completely embedded. This stepwise process enables the understanding of interaction between particle and environment on a nanometer scale, discussed in chapter 5.

3.2.2 Cleaning

The construction of nanostructures requires a clean substrate's surface. A fast cleaning method is an ultrasonic bath in acetone for one minute, followed by rinsing with pure water and nitrogen drying. But some sonicated substrates cannot be wetted with PEI solution and therefore multilayers can not be grown. To avoid this, glass or silicon substrates were immersed in peroxymonosulfuric acid H_2SO_5, so-called piranha solution. This strongly oxidizing acid adds silanol groups to the surface, making it more hydrophilic [70]. Piranha solution has to be freshly prepared for every use by adding 1 part of concentrated sulfuric acid H_2SO_4 to 3 parts of aqueous hydrogen peroxide solution H_2O_2 ($c = 30\%$)[2]. The mixture will become hot and is very aggressive to most organic materials. It must be handled very carefully and should not be moved. After at least 10 minutes of immersion, the substrates were rinsed with purified water. Complete wetting indicates a hydrophilic and clean surface. To avoid the cleaning procedure for every sample, several substrate can be treated simultaneous. Within few hours, the H_2SO_5 breaks down to H_2SO_4 and water. These products do not affect the substrates any more. Thus, the substrates can be stored in the solution for long time.

3.2.3 Spin-Assisted Layer-by-Layer Deposition

The spin-assisted layer-by-layer technique is one of the fastest methods to produce multilayer samples. This procedure guarantees a high number of surface charges to

---

[2]Some sources recommend to add H_2O_2 to the H_2SO_4

adsorb charged molecules or particles. The clean substrates were wetted with PEI solution (c = 1% wt), spun at 3000 rpm for 10 s and rinsed with 3 drops (~60 µL) of purified water while spinning. On very hydrophobic substrates, aqueous solution of PEI will not wet the surface. Here, ethanol can be used as solvent. The other polyelectrolytes PSS, PAH, and PAzo were dissolved in water (c = 0.1% wt). An amount of 0.58 g NaCl was added to 10 mL aqueous solution, giving a concentration of 1 mol/L. It is noted that PAzo forms insoluble clusters, if water is added to a mixture of PAzo powder and NaCl. Dissolution can be enhanced by using an ultrasonic bath. The preparation of polyelectrolyte multilayers is depicted in figure
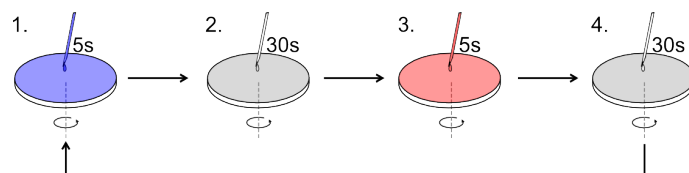

Figure 3.4: The sketch shows the successive deposition of oppositely charged polyelectrolytes (e.g. PSS and PAH). The solution is dropped onto the rotating sample (1). After few seconds, the remains are washed away (2). If the sample is dry, the next layer can be deposited (3). After washing and drying (4), the process can be continued with step 1.

3.4. During the whole process, the sample rotated at 3000 rpm. PSS or PAzo solution was dropped (~20 µL) onto the PEI-covered sample. After few seconds, the excess of polyelectrolytes was washed away by 3 drops (~60 µL) of water. When the sample was dry, the second solution (PAH) was deposited by the same work steps. Depending on humidity and temperature, it is possible to grow one double layer in 60 seconds. A much faster preparation without drying is also possible. But then, aggregates of PSS/PAH are formed within the film of solution. These aggregates bind to the surface and increase the roughness dramatically [59]. Such multilayer structures might be a good base for depositing nanoparticles of 50 nm or more in diameter.

3.2.4 Deposition of Gold Nanoparticles

Gold nanoparticles can be deposited, if the topmost layer is positively charged (PAH). For gold nanospheres, a dipping method must be applied since the surface charges of the particles are to weak for spin-assisted deposition. Therefore, the spin coater was stopped and the sample was covered completely with gold suspension. The suspension rested for at least 30 minutes up to several hours. The in plane packing density of particles depends on immersion time and concentration of the used suspension [22]. Layers of gold nanorods were prepared in the same way. But due to their cover with one monolayer of PSS, the GNRs adsorb much faster. Samples discussed in this work were prepared with an immersion time of 12 minutes. Later experiments showed that spin coating of these particles is also possible. In both cases, the rods lay in plane with random orientation (see fig. 3.5). After rinsing with water and drying, layers of polyelectrolytes can be added, starting with PAH.
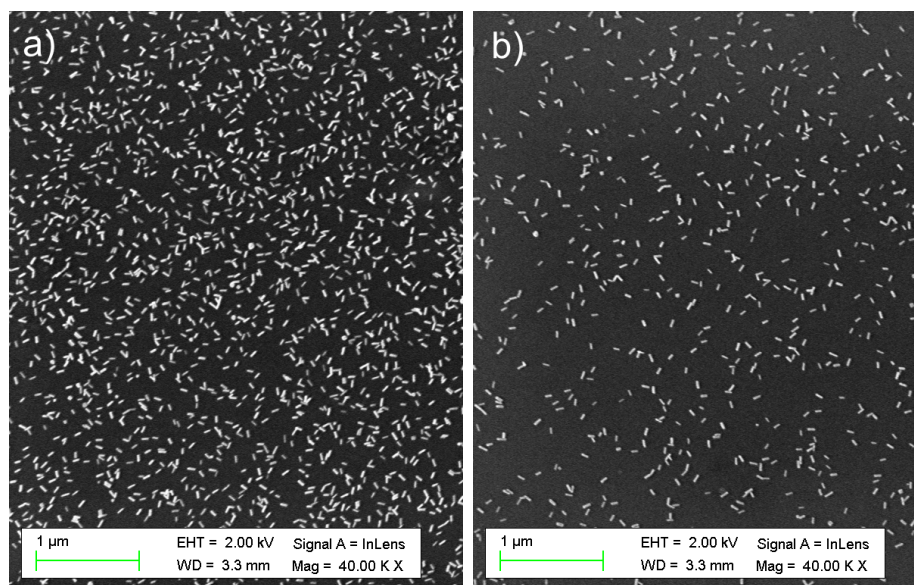
Figure 3.5: In plane distribution of GNR measured by SEM. Picture (a) shows dip-coated particles with 4 minutes immersion time. The particles in picture (b) are spin-casted (100 µL dropped on rotating sample).

3.2.5 Vapour Deposition

Thin metal films can be produced in several ways. In this work, vapour deposition was used, where a metal is evaporated in a vacuum chamber by heating. The steam condenses on the substrate, while growth rate is controlled during the process. The aluminum samples discussed in this work were grown with 0.5 nm to 1.2 nm per second.

4 Experimental Methods 2: Sample Characterization

4.1 Static Sample Characterization Methods

The development of models explaining the optical properties of gold nanoparticles, or the laser-excited dynamics within layered samples requires a very precise determination of the sample parameters. Size parameters such as particle dimensions, layer thicknesses, and subsidence depth of a particle in the embedding medium were determined by atomic force microscopy (AFM) and scanning electron microscopy (SEM). The optical characterization was carried out via UV-VIS spectroscopy and ellipsometry. The following paragraphs explain these four techniques and their specific applications for this work.

4.1.1 UV-VIS Spectroscopy

Static spectroscopy measurements were performed with an UV-VIS-NIR spectrophotometer (VARIAN CARY 5000). The measurable spectrum ranges from 200 nm to 2500 nm wavelength. The device is equipped with an integrating sphere (Ulbricht sphere), schematically shown in in figure 4.1. It detects specular and diffuse contributions of reflected and transmitted light. Both quantities were measured separately: reflection for an incident angle of $3° \, 20'$ and transmission under normal incidence. From these data, absorption can be calculated by the formula $A = 1 - T_{s,d} - R_{s,d}$. Both, transmission T_{sd} and reflection R_{sd} contain a specular (s) and a diffuse (d) scattered part in forward and backward direction, respectively. It is noted that the absorption mode of most spectrometers is not applicable for exact absorption measurements, since scattering and interference effects in thin films are not considered.

4.1.2 Atomic Force Microscopy

Atomic force microscopy (AFM) is a method to analyze the surface topography and material properties of a sample. The application of a very sharp tip achieves a height resolution in the sub-nanometer range. The tip is fixed at the end of an silicon cantilever that bends according to the position of the tip. In tapping mode, piezoelectric actuators initiate the cantilever oscillating at a frequency close to resonance. Cantilever position and phase of it's oscillation are detected by a laser, reflected from the cantilever backside. The surface topography is mapped by moving the tip over the sample. The height profiles, shown in chapter 5 were measured by this technique.

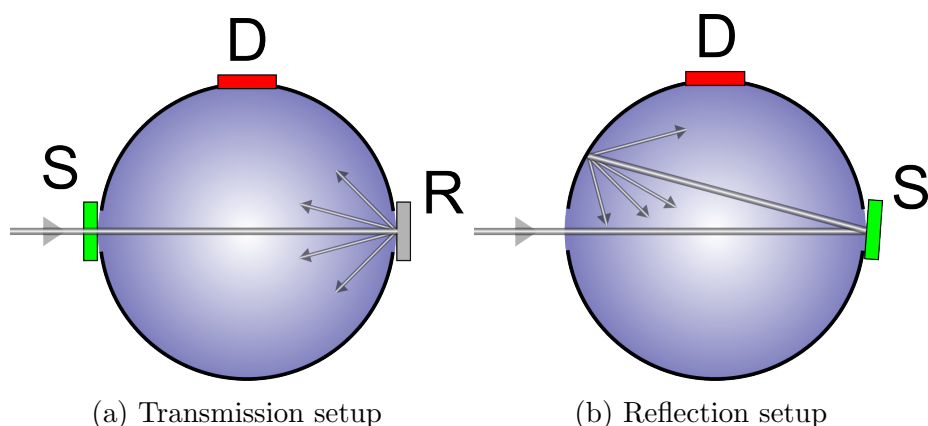(a) Transmission setup   (b) Reflection setup

Figure 4.1: Schematic view of an integrating sphere. In (a) the sample (S) is placed on the transmission port. Transmitted light is scattered on a diffuse reflector (R) and collected by the detector (D). For reflection measurements, the setup in (b) is used. The sample placed on the reflection port. It has to be slightly tilted to measure direct and diffuse reflected light.

In addition to the height profile, the elasticity of the material can be measured. Therefore, the phase of the oscillating cantilever is analyzed. Soft materials such as polymers cause a negative phase shift whereas hard materials (e.g. substrate or metal nanoparticles) show a positive shift.

AFM is also suitable to determine the thickness of a layered sample. The sample was scratched with a fine iron needle or a scalpel to remove the sample layer. The height profile scan across the scratch shows a sharp step between layer and substrate. The difference in height is the sample thickness. This method was used characterize the polyelectrolyte multilayers, discussed in chapter 6.

4.1.3 Scanning Electron Microscope

A scanning electron microscope (Zeiss Ultra Plus) is a type of electron microscope that images the interaction of a focused beam of electrons with matter. The resolution is below 1 nm and therefore comparable to an AFM. While the beam scans across the sample, secondary electrons are detected. These electrons are emitted by excited atoms, if their energy exceeds the work function of the material. The number of released electrons depends on the angle between surface and incident electron beam. By counting these electrons for each spot, the tilt of surface can be mapped. Another mode is the observation of backscattered electrons. The scattering of these primary electrons essentially depends on the material. Heavy elements provide a strong backscattering whereas light atoms show a weak signal. The resolution of that mode is a little worse than secondary electron detection, but it shows high contrast pictures for samples made of different materials.

Scanning electron microscopy is an excellent and fast method to measure the distribution or size of the gold nanoparticles, treated in chapter 5. Since the electron beam penetrates most of the polylectrolytes, surface imaging and roughness mea-

surements are not possible. To gain highest resolution, a conductive substrate is recommended.

4.1.4 Ellipsometry

An ellipsometry experiment determines thickness and refractive index of a sample for one wavelength or a broad spectrum. An incident light beam is polarized linearly by a polarizer and reflected from the sample. Before detection, the reflection passes a second polarizer that is orientated perpendicular to the first one. The reflection at a thin film causes an elliptical polarization due to interference of multiple reflections and delayed propagation in the medium. The intensity ratio of p- and s-polarized light is called Ψ. The phase shift between p- and s-polarization is Δ. Equation 4.1.4 determines the correlation between these ellipsometric parameters and the ratio of the measured reflection coefficients $R_\perp$ and $R_\parallel$.

$$\frac{R_\parallel}{R_\perp} = \tan \Psi \exp(i\Delta) \tag{4.1}$$

To extract layer thickness and refractive index, a layer model has to be established. For a known layer sequence, thickness and optical parameters are varied in an iterative procedure. Ψ and Δ are calculated using Fresnel formulas and equation 4.1.4 until the fit matches the experimental data. Layer thicknesses and refractive indices of polyelectrolyte multilayers were determined by this technique.

4.2 Time-Resolved Sample Characterization: Pump-Probe Experiment

This section gives an overview of time-resolved spectroscopy. In contrast to steady state spectroscopy, the temporal resolution of a pump-probe experiment is typically below one picosecond. This is indispensable for the picosecond acoustic experiments, treated in chapter 6.

4.2.1 Femptosecond Laser System

Ti:Sapphire Laser System   All time-resolved measurements were carried out with a laser system from Spectra Physics GmbH (Germany). This system contains three parts. The oscillator (MaiTai) provides ultrashort laser pulses with high repetition rate. These pulses are amplified by the Spitfire Pro unit, which is pumped by a high-power diode laser (Empower). A Ti:Sapphire crystal is used as active medium in the oscillator and the amplifier.
The oscillator is actively mode-locked and tunable in wavelength, ranging from 710 nm to 920 nm. According to the pulse duration below 100 fs, the spectra is broad. For all experiments of this work, the oscillator is fixed to a wavelength of 795 nm. Only 500 mW of the 1.5 W output power is used as seed beam for the amplifier. In the amplifier, this seed beam is stretched to several picoseconds to avoid
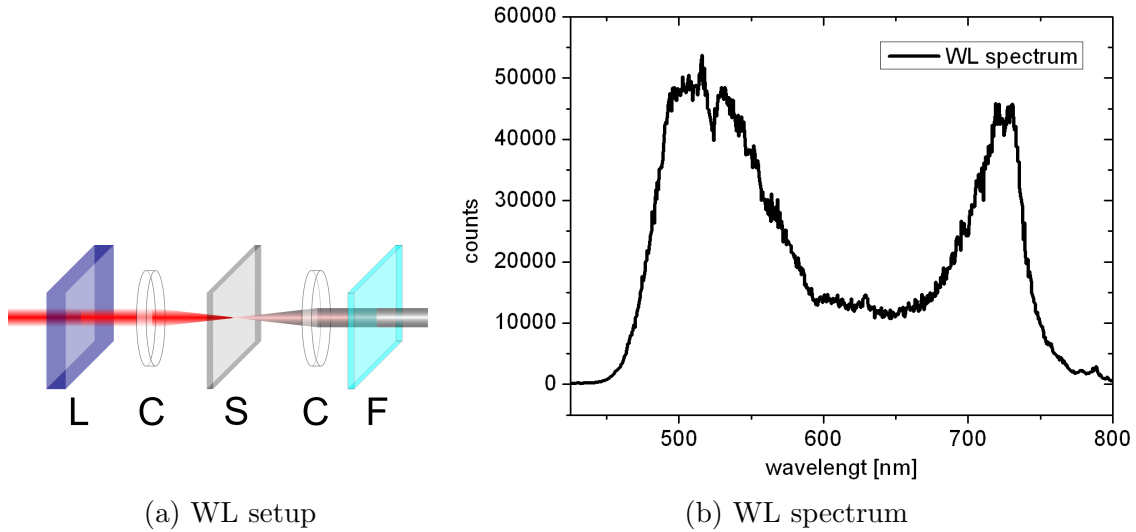
(a) WL setup

(b) WL spectrum

Figure 4.2: Schematic setup for white light generation a). The setup uses an optional λ-half plate (L) and concave lenses (C) that focus the beam into the sapphire plate (S) and collect the generated white light, respectively. The fundamental 800 nm light is cut off with a low pass filter (F). The spectral output is shown in b).

damage of the Ti:Sapphire. Pockels cells select pulses from the seed with a repetition rate of 5 kHz. Each pulse travels through the Ti:sapphire crystal several times. The crystal is pumped with a laser power of about 15 W at a wavelenght of 532 nm, provided by the Empower. Each cycle in this unit amplifies the pulse until saturation is reached. Afterwards the pulse is coupled out and compressed again. The result are ultrashort light pulses of about 120 fs duration. They are p-polarized and have a pulse energy of 0.3 mJ. The central wavelength is 795 nm with a bandwidth of 8 nm (FWHM).

4.2.2 Nonlinear Optics

Frequency Doubling   The basic wavelength of about 800 nm can be frequency-doubled for pumping and converted to white light for probing. For frequency doubling, the beam is focused into a crystal of beta-barium borite (BBO). This material is highly nonlinear and birefringent. Phase matching of incident beam and generated second harmonic is possible, if the pulses are polarized perpendicular to each other. Before using as pump beam, a separation of the fundamental 800 nm and the generated 400 nm beam should be realized by using dichroic mirrors, polarizers or filters.

White Light Generation   To probe a fully visible spectrum with one shot, white light is needed. To this end, a weak beam of 795 nm wavelength is focused into a sapphire plate. The setup is schematically shown in figure 4.2a. The high energy density generates a continuous spectrum of white light [71]. A typical spectral intensity distribution is plotted in figure 4.2b. The fundamental beam has to be
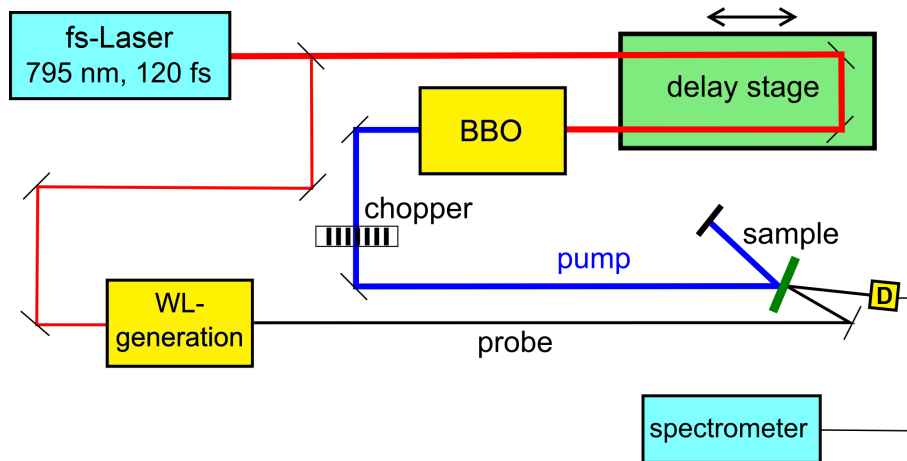
Figure 4.3: Schematic laser setup as used in this work. The sample is pumped from front side and probed from the back. The BBO for frequency-doubling is optional, depending on the desired pump wavelength.

blocked by a low pass filter, to avoid damage on the probed sample.

4.2.3 Experimental Setup

The data, discussed in chapter 6, were measured with a pump-probe setup, shown in figure 4.3. The fundamental laser beam is divided into a weak pump and a strong probe beam by a separator. The pump beam crosses a delay stage that varies temporal shift between pump and probe. The following chopper is necessary to distinguish pumped and unpumped sample (both explained in section 6.3). Not shown in figure 4.3 are $\lambda/2$-plate, polarizer, and lenses to tune the pump intensity, control its polarization, and focus the pump beam onto the sample.

The weak part of the fundamental laser generates white light that is focused onto the sample. The reflection is coupled into a glass fiber and guided into the spectrometer. The transmission was not measured, although both can be done simultaneously. Usually several reflections occur of which the reflection from the substrate-air interface might be the strongest. But it does not contain any time-dependent signal and has to be blocked.

5 Interaction of Gold Nanoparticles with the Surrounding Medium

5.1 Characterization of Gold Nanorods

5.1.1 Size Distribution Measured by SEM

The size distribution of the GNRs was measured by SEM. A single drop (~20 µL) of GNR suspension was brought onto a PEI treated silicon substrate and rested until the water evaporated completely. The pictures (d) to (f) in figure 5.1 show high resolution SEM images of the particles. At least 30 particles of each GNR type were evaluated. This evaluation shows that the particles are not monodisperse. The variations in length and diameter result in distribution of the shape factor u, as shown in figure 5.2. The shape factor u was calculated for each particle separately, using equation 2.13. An overview of particle size and related parameters is given in table 5.1.
Pictures (a) to (c) in figure 5.1 show the samples, treated on the following pages. Here, the preparation was done as described in section 3.2.3. From these measurements, the in-plane packing density is determined. It shows a very dense packing for GNRs type 1 (134 particles per μm^2) and low packing for GNRs type 2 and 3 ($23/\mu m^2$ or $11/\mu m^2$, respectively).

5.1.2 Subsidence of GNRs Measured by AFM

The following pages deal with the optical characteristics of GNR-polymer composites against the background of Maxwell-Garnett effective medium theory. Thus, it is crucial to know the portion of air and polymer in the particles' environment. The transition from uncovered particles to full embedding can be tuned by the number of cover layers. During deposition, the particles sink into the polymer layers. The initial fraction of particle surface covered with polymer is given by the depth of subsidence. To determine this value, measurements of the sample topography were done by AFM. An example of these measurements is shown in figure 5.3 a). The average height of each particle type is listed in table 5.1. The subsidence depth is the difference of particle diameter and height.

5.1.3 Optical Characterization by Steady-State Spectroscopy

The UV-VIS spectroscopy measurements were performed by using the setup described in 4.1.1. Figure 5.4 shows a series of transmission and reflection data of samples containing gold nanorods of type 1. The layering sequence is $(PSS/PAH)_8+(Rod$
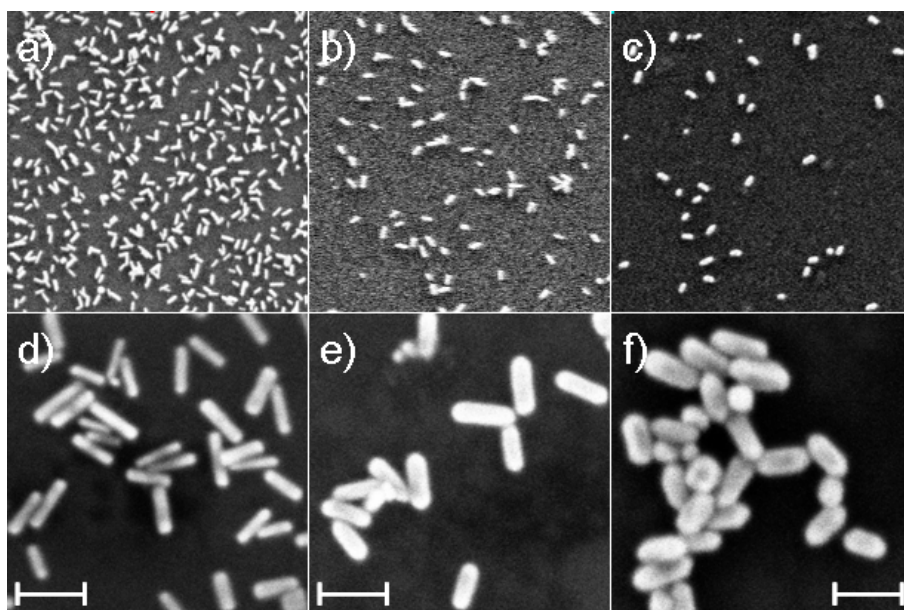
Figure 5.1: SEM pictures of the applied GNRs. Pictures (a), (b), and (c) show the packing density of GNRs type 1, 2, and 3 on an area of $2 \times 2\,\mu\text{m}$. Pictures below show the particles with higher resolution. The white bars represent $100\,\text{nm}$.
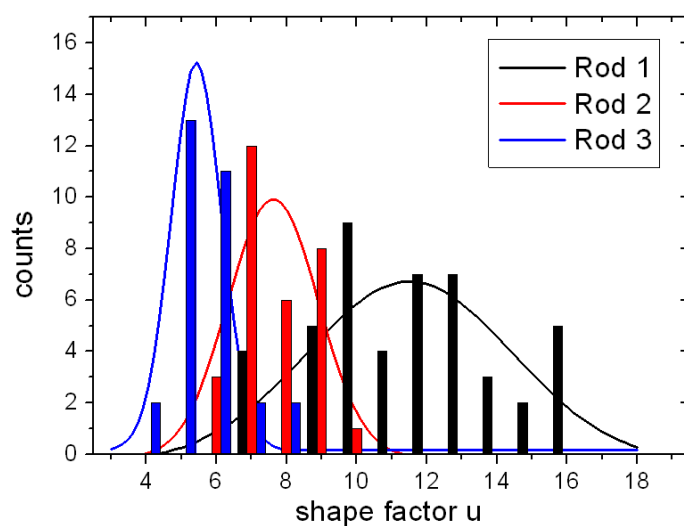
Figure 5.2: Distribution of the shape factor u for GNRs type 1, 2, and 3. Due to the variation of particle size, the Gaussian curves, shown as solid lines, barely fit the distribution.
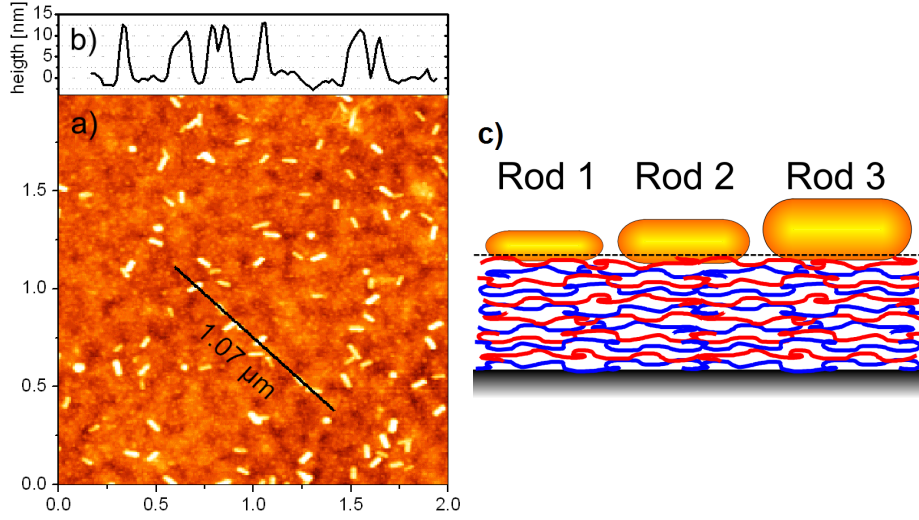
Figure 5.3: AFM topography (a) of GNR type 1 on an area of $2 \times 2\,\mu\text{m}^2$. Panel (b) shows the cross section along the black line in (a). Figure (c) illustrates subsiding particles of each type drawn-to-scale.

Type	Length L [nm]	Diameter D [nm]	Aspect ratio R (D/L)	Height H [nm]	Shape factor u	
					long	trans
Rod 1	63.4 ± 8.1	16.3 ± 1.5	3.9 ± 0.6	13.4 ± 1.5	11.93 ± 2.42	1.18 ± 0.04
Rod 2	70.1 ± 7.7	23.4 ± 2.8	3.0 ± 0.3	19.4 ± 2.3	8.27 ± 1.19	1.25 ± 0.04
Rod 3	79.0 ± 9.8	32.7 ± 2.7	2.4 ± 0.3	30.4 ± 1.2	6.15 ± 0.95	1.33 ± 0.05

Table 5.1: Size distribution of GNRs measured by SEM. The aspect ratio is length divided by diameter, determined for each particle separately. The height H of the particle on the sample was measured by AFM. The shape factor u is defined by equation 2.13.
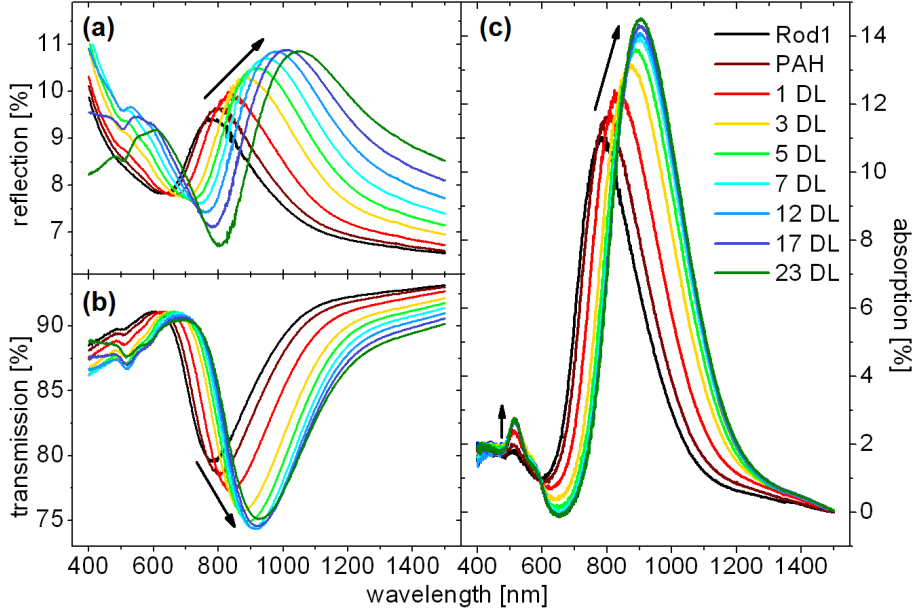
Figure 5.4: Series of reflection (a) and transmission (b) spectra of GNRs type 1 in polyelectrolyte matrix. The absorption (c) is calculated by $A = 1-T-R$. Black lines indicate the first spectrum, taken for particles at air interface. The arrows illustrate the development for increasing number of cover layers.

1/PAH)+(PSS/PAH)$_n$ where n is the number of cover layers. It starts with zero, meaning that the first spectrum was taken for particles at air interface. The arrows in the plots indicate the development with increasing n. In case of GNR type 1, the reflection spectra shifts about 270 nm to higher wavelengths. Maximum and minimum become more pronounced, but only the maximum shows saturation. At short wavelengths ($\lambda < 500$ nm), the reflection decreases for the last three spectra. This is caused by destructive interference in the thin film layer and leads to an increased transmission. The transmission spectra show two minima. The small one is located at 510 nm, showing a small decrement and almost no shift. The bigger one at 785 nm shifts strongly during the series (+145 nm) and decreases from a value of 0.80 to 0.75. Both peaks saturate within the first seven cover layers of PSS/PAH.

The absorption spectra are calculated by $A = 1-T-R$. They are dominated by the strong absorption peak at 783 nm that shifts about 120 nm to higher wavelengths and increases from 0.11 to a value of 0.14. As seen before, this effect slows down with rising cover thickness, showing saturation behavior when more than 7 DL (~17.5 nm) of PSS/PAH are added. The small peak located at 511 nm saturates when a cover of 3 DL (~9 nm) is added.

Measurements of samples containing gold nanorods type 2 and 3 are shown in figure 5.5. The same effects of shifting peaks and saturation occur, but the initial peak positions differ as well as the ratio between transverse and longitudinal plasmon absorption peak. The side peaks at 950 nm and 800 nm, respectively, are caused by clusters. The measured data are summarized in table 5.2.
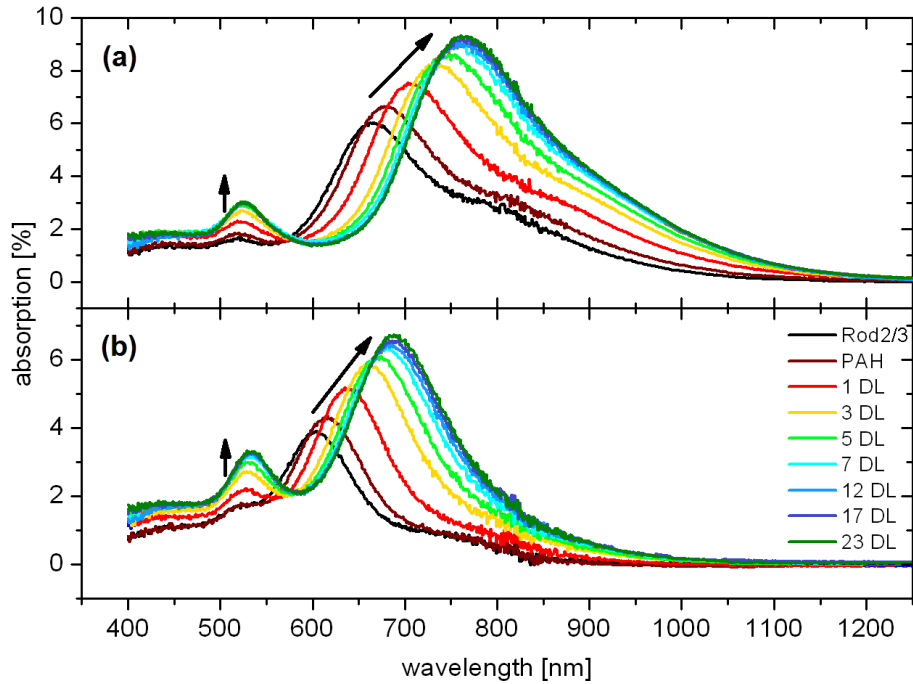
Figure 5.5: Series of calculated absorption spectra for GNR of type 2 (a) and type 3 (b). The data base upon reflection and transmission measurements of samples with increasing cover layer thickness. The spectral change is indicated by the arrows.

GNR Type	Peak position (uncovered)		Peak position (fully embedded)		Peak shift	
	long	trans	long	trans	long	trans
Rod 1	783	511	893	514	110	4
Rod 2	663	517	763	526	100	9
Rod 3	602	517	687	534	85	17

Table 5.2: Characteristics of the absorption spectra of gold nanorods at air interface and embedded in medium, respectively. All values are given in nanometers.
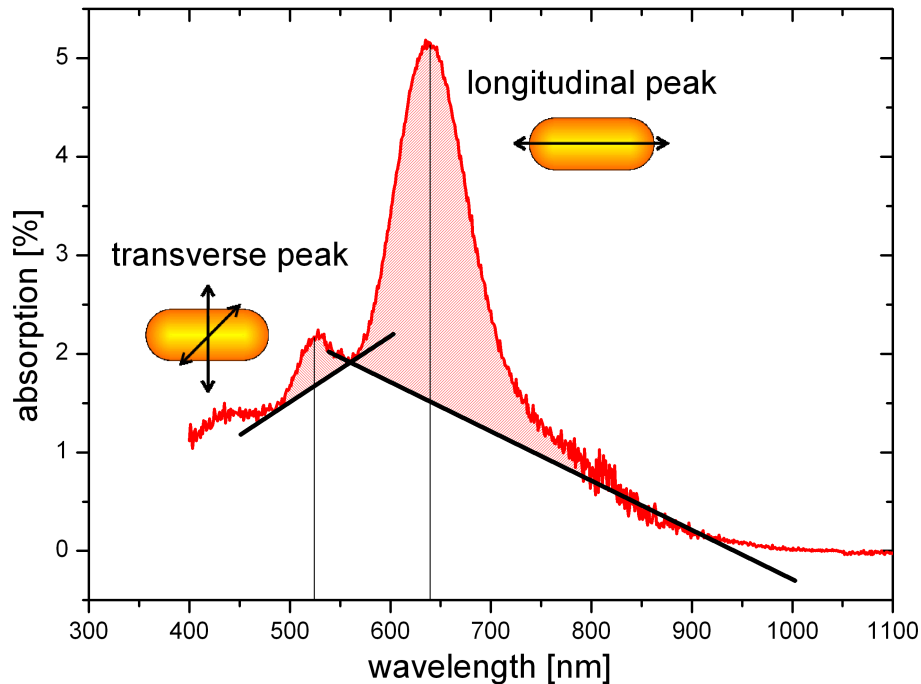
Figure 5.6: Characteristics of a GNR absorption spectrum. Transverse (left) and longitudinal plasmon absorption peak (right) are analyzed separately. The solid black lines approximate the respective underground. The highest data point above these lines define the peak positions and the shaded areas are taken as total plasmon absorption.

5.2 Data Analysis

Before discussing the measured data, a short overview of data analysis shall be given. The calculated absorption consists of tree parts. Intraband, interband, and localized surface plasmon resonance (LSPR) absorption were explained in section 2.1. Intraband and interband both depend on the material, but not on the shape of the particles. The analysis focuses on the third part, the LSPR absorption. To achieve useful values, other contributions to the absorption must be neglected. Therefore, the intraband absorption is approximated by a line from the minimum between transverse and longitudinal plasmon peak to that point in the near-infrared, where the spectra reach zero. The area above, defined by the integral $A(n) = \int A(n, \lambda) d\lambda$, is the absorption of the longitudinal plasmon peak. The same is done for the smaller transverse plasmon absorption peak, located at roughly 520 nm. Here, the line contains the constant underground of interband absorption and parts of the interband absorption (negative slope) or parts of the longitudinal plasmon absorption peak (positive slope). For both peaks, the highest data point above the particular line is taken as peak position. The full procedure is visualized in figure 5.6.

Figure 5.7: Shift of the longitudinal plasmon peak (a) and relative absorption change (b) for the three types of GNRs depending on cover layer thickness. The lines are fits of the data points, using a r^{-3} power function. The layer thickness corresponding to 95% of saturation value is marked.
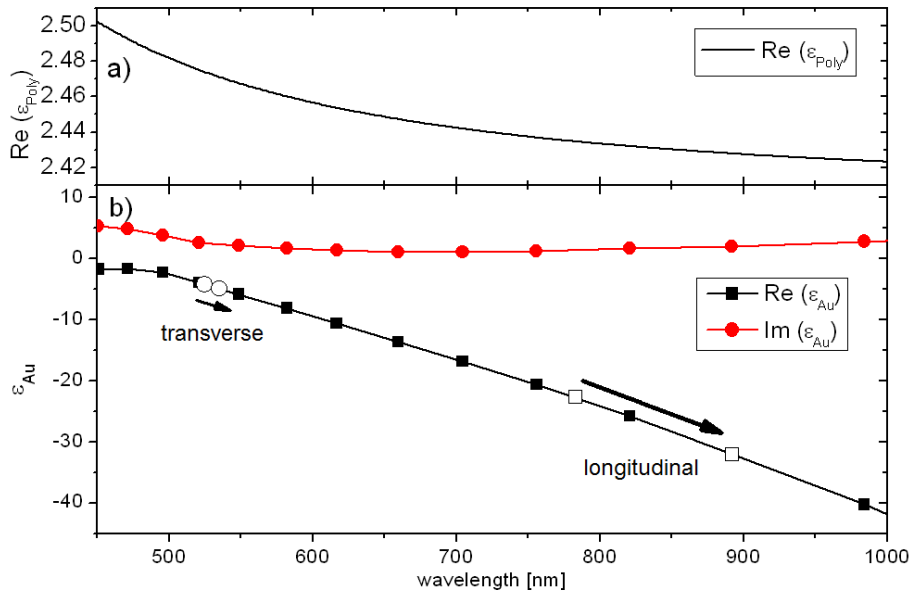
Figure 5.8: Dielectric functions of PSS/PAH multilayers (a) measured by ellipsometry, and bulk gold (b) taken from the literature [37]. Open symbols mark the measured absorption wavelengths for transverse and longitudinal LSPR, respectively. The arrows indicate the peak shift from uncovered to fully embedded particles.

5.3 Discussion

The absorption data in figures 5.4 c) and 5.5 are dominated by the LSPR absorption peaks. The influence of the cover layer thickness on the peak positions and the total change of absorption will be analyzed.

5.3.1 Redshift of the LSPR Absorption Peaks

Successive covering of the gold particles shifts the absorption to the red. This shift can be explained by the formula of resonant absorption (equ. 2.13) and the dieelectric function of gold ϵ_{Au}, depicted in figure 5.8b. The product of the shape factor u and the dielectric function of the medium ϵ_m defines the value of ϵ_{Au} at the resonance. Covering the particles increases the value of ϵ_m while u is fixed. As a result, $\epsilon_{Au} = -u\epsilon_m$ decreases and the absorption wavelength shifts to the red. Since the dielectric function of gold is almost linear in the observed spectral range, the absolute shift depends linearly on u. This explains the strong shift of the longitudinal plasmon peak ($\Delta\lambda > 85\,\text{nm}$, $u_{long} > 6$) and the comparatively weak shift of the transverse plasmon peak ($\Delta\lambda < 17\,\text{nm}$, $u_{trans} < 1.4$). It also explains that the largest shift is observed for the particles with the largest aspect ratio.

5.3.2 Saturation of the LSPR Absorption Peaks

The interaction of particles and surrounding medium is mediated by dipol-dipol interaction. The electric near field of a dipole drops with r^{-3}. Thus, the range of interaction is limited to several nanometers. This effect is visualized in figures 5.7 and 5.9. All data points of peak shift and relative absorption converge to their respective saturation values. This means that polymer added beyond the range of interaction is not affecting the LSPR absorption anymore. The data are fitted by the 3rd order power function $y(x) = a - b(x - x_0)^{-3}$. By these fits, the values of saturation a are determined. The corresponding cover layer thicknesses of saturation d_{sat} are defined as these values, where 95 % of a are reached.

Longitudinal LSPR As shown in figure 5.7a, the consecutive embedding of the GNRs shifts the longitudinal peaks by 85 nm (Rod 3) up to 110 nm (Rod 1). Compared to the peak shift, the corresponding value of saturation $d_{sat}(\Delta\lambda)$ varies only slightly around 32 nm. The intuitive connection of longitudinal LSPR and particle length becomes apparent, if the ratio of $d_{sat}(\Delta\lambda)$ and L is observed. Here, a linear dependence is given (see tab. 5.4).

Another relation can be observed for the absolute peak shift $\Delta\lambda$ and the initial peak position λ_0. The ratio $\Delta\lambda/\lambda_0$ is constant for all three particle sizes (Rod 1: 0.14, Rod 2: 0.15, Rod 3: 0.14). Jain and El-Sayed reported similar observations in their studies about plasmonic coupling of gold spheroids [72]. The connection of $\Delta\lambda$ and λ_0 is explained by the dielectric function of gold. The negative slope of the real part $Re(\epsilon_{Au})$ can be approximated as linear in the observed spectral range (see fig. 5.8b). Thus, the absorption wavelength λ is also linearly depending on the product $-u \cdot \epsilon_m$. As shown before, the peak shift depends on the same term. So initial wavelength and absolute peak shift are connected by the shape factor u.
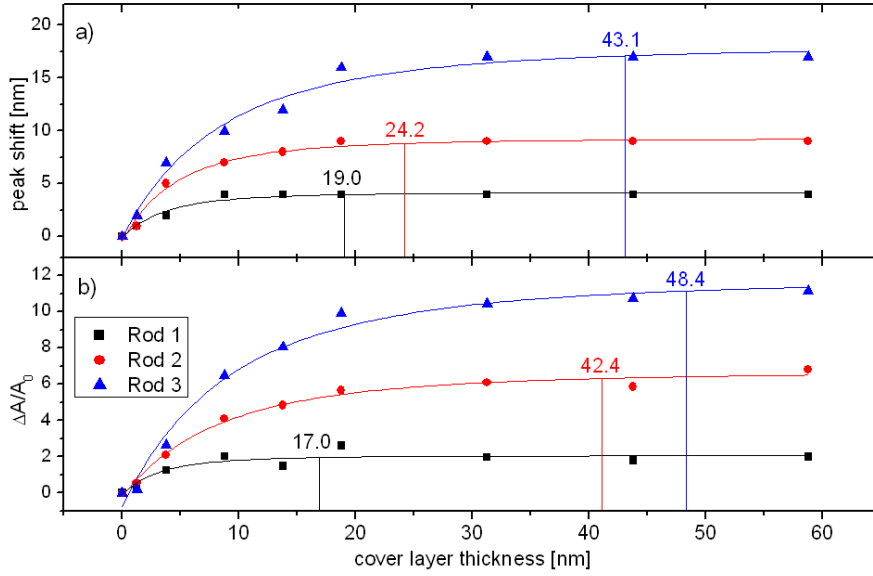
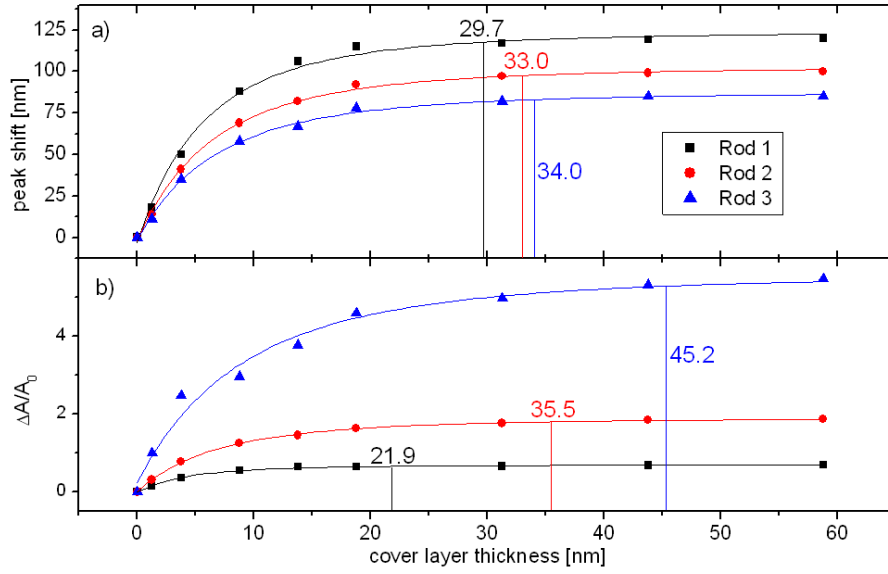Figure 5.9: Shift of the transverse plasmon peak (a) and relative absorption change (b) for the three types of GNRs depending on cover layer thickness. The lines are fits of the data points, using an exponential saturation function. The marked values of layer thickness correspond to 95% of saturation.

Besides the peak positions, the integrated absorption is analyzed. Figure 5.7b shows the relative change of integrated absorption $(A_n - A_0)/A_0$ for the longitudinal plasmon peak. As seen before, the slope decreases with increasing cover layer thickness. The dependence of the integrated absorption on the particle type is much stronger than the dependence of the peak shift. The absorption of GNRs type 1 increases by a factor of 0.7 whereas the peak of type 3 grows about a factor of 5.5. This indicates a connection to the particle volumes. The values of saturation d_{sat} also differ. This is caused by the different particle diameters. Since the particles lie in plane, the cover layer thickness has to be in the range of the diameter to ensure a complete embedding.

Transverse LSPR   The shifts of the transverse plasmon resonance and their relative changes of absorption are plotted in figure 5.9. Both show the expected saturation behavior that depends on the particle size. Small particles with a large aspect ratio (Rod 1) show less peak shift and saturate earlier than particles with low aspect ratio (Rod 2 and Rod 3). In comparison to the longitudinal LSPR peaks, the transverse peaks shift about one magnitude less (3 nm to 17 nm).

As shown in 5.9b, the absorption of the transverse LSPR peaks rises stronger than the absorption of the longitudinal ones. Within the errors, both, longitudinal and transverse plasmon absorption saturate at the same cover layer thickness that is close to the particle diameter.

The peak positions between 511 nm and 517 nm as well as the shifts between 4 nm and 17 nm are similar to the plasmon absorption of spherical gold nanoparticles. Previous experiments of our group showed that saturation of spherical particles occurs, when the cover layer thickness is in the range of the particles diameter. But

Type	length/diameter	$d_{sat}(\Delta\lambda)$		$d_{sat}(\Delta A/A_0)$	
		long	trans	long	trans
Rod 1	62.5 / 16.1	29.7 ± 3.5	19.0 ± 2.4	21.9 ± 1.0	17.0 ± 4.2
Rod 2	70.1 / 23.4	33.0 ± 2.3	24.2 ± 2.0	35.5 ± 0.9	42.4 ± 3.2
Rod 3	79.0 / 32.7	34.0 ± 3.1	43.1 ± 4.1	45.2 ± 7.3	48.4 ± 4.9

Table 5.3: Particle interaction range: Cover layer thickness d_{sat} for peak shift $\Delta\lambda$ and relative absorption change $\Delta A/A_0$ determined by the fitting curves in figures 5.7 and 5.9.
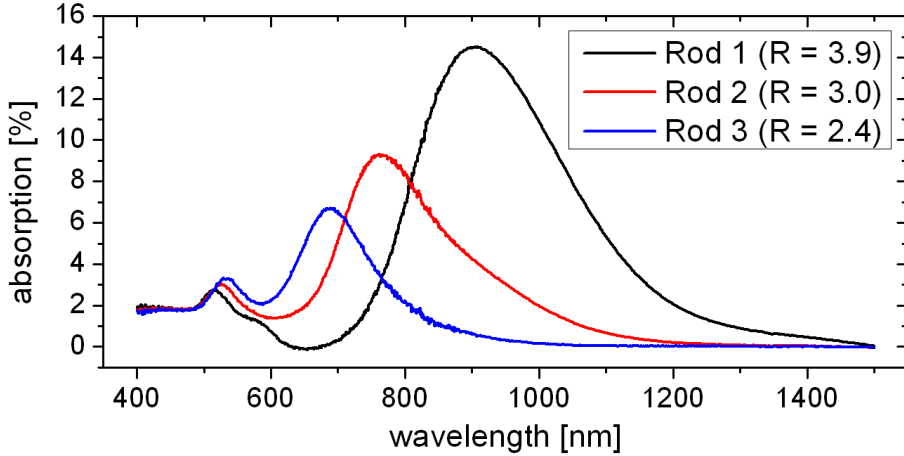
Figure 5.10: Absorption spectra of full embedded gold nanorods with different aspect ratios R. With decreasing R, the transverse LSPR peak shrinks and shifts to the blue. In the limiting case $R = 1$ (spherical particle), only one LSPR peak remains at about 520 nm (not shown).

the integrated absorption of embedded spheres is only about twice as large as the absorption of spheres at air interface [22].

5.3.3 Size and Range of Interaction

In order to compare the particle size with the range of plasmonic interaction, all values are listed in table 5.3. As first guess, one would expect one value of saturation for each particle type. Within a wider tolerance, this is the case for three of the four absorption characteristics: change of longitudinal and transverse absorption peak and the shift of the transverse one. Particles of type 1 show saturation, if the cover thickness reaches roughly 20 nm. For GNRs type 3 saturation occurs at roughly 45 nm and GNRs type 2 spread in between these two values. Only the peak shift of the longitudinal absorption makes an exception. Here, all cover thicknesses of saturation locate very close to each other in the range of 32 nm. This might be caused by different shifting behavior that is strongest for the smallest particles. Although the peak position depends on the aspect ratio, a connection to the particle length can be found. The ratio of $d_{sat}(\Delta\lambda)$ and length L is almost constant for all types of particles (see table 5.4). This is surprising, since this ratio has to converge to a value of 1, the more sphere-like the shape of the particles is [22]. One possible explanation

Type	$d_{sat}(\Delta\lambda)/L$	$d_{sat}(\Delta\lambda)/H$		$d_{sat}(\Delta A/A_0)/H$	
	long	long	trans	long	trans
Rod 1	0.48 ± 0.12	2.22 ± 0.51	1.42 ± 0.34	1.63 ± 0.26	1.27 ± 0.46
Rod 2	0.47 ± 0.08	1.70 ± 0.32	1.25 ± 0.25	1.83 ± 0.26	2.19 ± 0.42
Rod 3	0.43 ± 0.09	1.12 ± 0.15	1.42 ± 0.19	1.49 ± 0.30	1.59 ± 0.22

Table 5.4: Relations of d_{sat} to particle length L and the height H of the uncovered particles, measured by AFM.
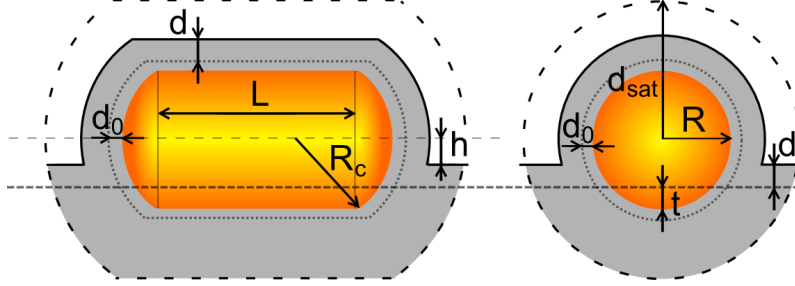
Figure 5.11: Sketch of a GNR with a polymer cover of thickness d. The size parameters of the cylindrical part are radius R and length L. The radius of the spherical calotte is R_c. Subsidence depth t was measured by AFM, the initial cover thickness d_0 is one layer of PSS and range of saturation d_{sat} was determined by fitting. The ratio of polymer (grey) to full volume (dashed area without particle) defines the dielectric function of the medium.

is that the longitudinal peak passes into the transverse peak with decreasing aspect ratio. The ratio $d_{sat}(\Delta\lambda)/L$ could be kept constant, but the related longitudinal absorption peak simply disappears. This effect can be seen in figure 5.10.

5.4 Effective Medium Theory in Two Phase Media

Maxwell-Garnett effective medium theory was developed for spherical particles in a homogeneous medium. By introducing the shape factor u, it is also applicable for rod-shaped particles. One step further is to simulate the position of LSPR, if the particles are only partially surrounded by medium. The environment of such particles is inhomogeneous and consists of two phases: One part of polymer with $\epsilon_{poly} \approx 2.45$ and one part of air with $\epsilon_{air} = 1$. Both values can be combined to an average dielectric function of the surrounding medium $1 \leq \epsilon_m \leq 2.45$. But an explanation how to combine both media cannot be found in the literature.

As shown in the previous measurements, the first cover layer of polymer causes the strongest shift. So not only the amount of polymer plays a role, but also it's distance to the particle. Therefore, the volume of interaction V' is introduced. It is weighted by the intensity E^2 of the light-induced dipole's electric field. The weighted volume is defined as

$$V' = \frac{1}{E_0^2} \int_V E^2 \, \mathrm{d}V \quad . \tag{5.1}$$
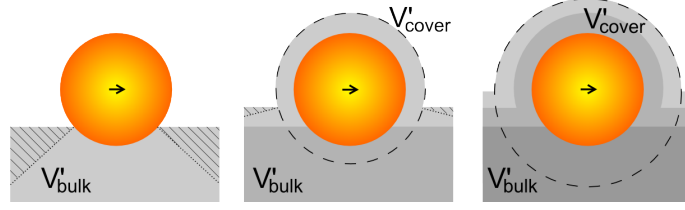
Figure 5.12: Stepwise embedding of a spherical gold nanoparticle. Each polymer layer adds a cover to the particle and its surrounding area. For symmetry reasons, the shaded areas were neglected. The black arrow illustrates the position of the point dipole.

This integral is evaluated for the polymer and the total volume. The ratio of both

$$x = \frac{V'_{polymer}}{V'_{total}} \tag{5.2}$$

yields an average dielectric function for the two phase medium

$$\epsilon_m = x\epsilon_{poly} + (1 - x)\epsilon_{air} \quad . \tag{5.3}$$

The electric field of a dipole with dipole moment $\vec{p}$ is defined as

$$E = \frac{3\hat{r}(\vec{p} \cdot \hat{r}) - \vec{p}}{4\pi\epsilon_0(\vec{r} - \vec{r_0})^3} \quad . \tag{5.4}$$

Assuming a dipole that is centered in the origin of a spherical coordinate system and oriented in z-direction, shortens equation 5.4 to

$$E = \frac{p(2\cos\theta\hat{r} + \sin\theta\hat{\theta})}{4\pi\epsilon_0\vec{r}^3} \quad . \tag{5.5}$$

The square of E defines the intensity of the dipole field

$$E^2 = \left(\frac{p}{4\pi\epsilon_0}\right)^2 \cdot \frac{3\cos^2\theta + 1}{r^6} \quad . \tag{5.6}$$

To calculate the integral (equ. 5.1), several parameters of the particles are necessary. A covered gold particle with all relevant parameters is sketched in figure 5.11. Particle radius R, length of the cylinder L, and depth of subsidence t are known from the characterization measurements (see tab. 5.1). The cylinder part is capped by spherical calottes with radius R_c at each end. The initial cover thickness d_0 describes the molecular shell the particles require for the synthesis of the structures. In case of GNRs, it is a layer of PSS that is added at the last step of the particle preparation (see sec. 3.1.2). The range of interaction d_{sat} was determined by fitting the saturation curves in figures 5.7 and 5.9. Since the weighted volume V' converges, the calculations are done for infinite volumes. Finally, the combined dielectric function of the two-phase medium ϵ_m is a function of the cover layer thickness d. This thickness is defined by the number of added polymer layers.
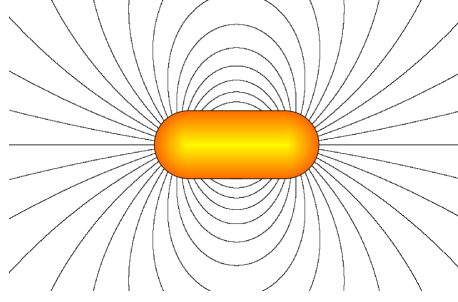
Figure 5.13: Distribution of the electric dipole field around a GNR. The maxima of the field intensity are localized at both ends. The environment of both ends dominates the interaction and the cylindrical part can be neglected.

5.4.1 Gold Nanospheres in Two Phase Media

Before applying the model to GNRs, it is verified on the more symmetric case of spherical particles. To enable analytic solutions of equation 5.1, the polymer volume is assumed as radial. As sketched in figure 5.12, a spherical shell of polymer rests on a cone-shaped base. Here, an infinite half space would be more accurate, but the strong dependence on radius r minimizes the error. Furthermore, the error decreases with increasing cover layer thickness.

The radius of the polymer shell is $H = (R + d_0 + d)$ and $h = (R - t - d_0 - d)$ is the height of the sphere's center above the polymer level (see fig. 5.11). With these values, the weighted polymer volume is

$$V'_{poly} = \left(\frac{p}{4\pi\epsilon_0}\right)^2 \left[\frac{\cos^{-1}(\frac{h}{H})}{3H^3}\left(7\sqrt{1 - \frac{h^2}{H^2}} + \cos\left(3\sin^{-1}\frac{h}{H}\right)\right) + \frac{8\pi}{3}\left(\frac{1}{R^3} - \frac{1}{H^3}\right)\right].$$
(5.7)

The total weighted volume of the particle's environment is

$$V'_{tot} = \left(\frac{p}{4\pi\epsilon_0}\right)^2 \left[\frac{8\pi}{3R^3}\right].$$
(5.8)

Both terms are the solution of equation 5.1. The detailed calculations can be found in the appendix. With known weighted volumes, equations 5.2 and 5.3 define the average dielectric function of the medium ϵ_m. With the resonance condition $0 = \epsilon_{Au} + 2\epsilon_m$, the resonance value of ϵ_{Au} can be determined.

5.4.2 Gold Nanorods in Two Phase Media

Gold nanorods can not be easily described in a highly symmetric coordinate system that provides the given formulas for the electric dipole field and the polymer volumes. Therefore, some approximations have to be done. The particles could be treated as spheroids, but the translation of equation 5.4 into ellipsoidal coordinates is difficult. Furthermore, the thickness of the cover layer would depend on the angle, so that spherical coordinates are most reasonable for the calculations.
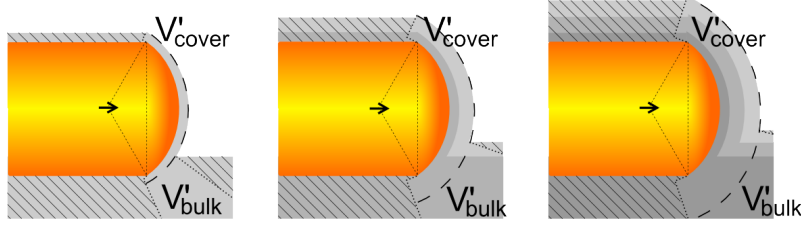
Figure 5.14: Sketch of polymer-embedded GNR. Each polymer layer adds a cover
to the particle and its surrounding area. The shaded areas were unac-
counted for the calculations. The black arrow illustrates the position
of the point dipole.

Actually, the charges are localized at the particle surface. To reduce the computing
work, just one dipole is assumed. Its charges are placed in the center of the spherical
calottes at each end of the particle. The curvature radius R_c is estimated from the
SEM data (see fig. 5.1). The electric field of the dipole is schematically shown in
figure 5.13. The field lines concentrate at both ends of the particle, whereas the
field intensity around the middle part is weak. Thus, the interaction of dipole and
surrounding medium is dominated by the environment of the end parts.

Cylindric Middle Part of a GNR   According to figure 5.13, the electric field is
assumed parallel to the surface. This assumption $\theta = \pi/2$, shortens equation 5.6 to
a simple r^{-6} dependency. With $H = (R + d_0 + d)$ and $h = (R - t - d)$, the weighted
volume of the cylindrical part is[1]

$$V'_{cylinder} = V'_{cover} + V'_{bulk} = \left(\frac{p}{4\pi\epsilon_0}\right)^2 \left[\frac{\pi L}{2}\left(\frac{1}{R^4} - \frac{1}{H^4}\right) + \frac{L}{2H^4}\cos^{-1}\left(\frac{h}{H}\right)\right] \quad (5.9)$$

and the total weighted volume is

$$V'_{cylinder,total} = \left(\frac{p}{4\pi\epsilon_0}\right)^2 \frac{\pi L}{2R^4} \quad . \quad (5.10)$$

Due to the strong $1/R^4$ dependence of the cylindrical weighted volume, the total
ratio defined in equation 5.2 is dominated by the $1/R^3$-depending spherical caps,
calculated in the following paragraph. Evaluating the model without the contribu-
tion of the cylindrical part produces an error below 1 %. To reduce the computing
time, the cylindrical part can be neglected.

Spherical Calotte as Cap of a GNR   The caps of a GNR are considered as spherical
calottes with radius R_c. By symmetry, the evaluation of one cap is sufficient. As
depicted in figure 5.14, the dipole is located at the radial center of the cap. For the
evaluation of equation 5.1, the polymer volume is split into a spherical cover with
radius $H_c = (R_c + d_0 + d)$ and bulk polymer with distance $h_c = (R_c - t - d)$ from

---

[1]See appendix for detailed calculation.

particle axis (see fig. 5.11). Both weighted volumes are[2]

$$V'_{cover} = \left(\frac{p}{4\pi\epsilon_0}\right)^2 \left(\frac{\pi}{6R_c^3} - \frac{\pi}{6H_c^3}\right)\left[-7\frac{\sqrt{R_c^2 - R^2}}{H_c} + \sin\left(3\sin^{-1}\frac{\sqrt{R_c^2 - R^2}}{H_c}\right) + 8\right]$$

(5.11a)

$$V'_{bulk} = \left(\frac{p}{4\pi\epsilon_0}\right)^2 \left(\frac{\cos^{-1}\left(\frac{h}{H_c}\right)}{6H_c^3}\right)\left[-7\frac{\sqrt{R_c^2 - R^2}}{H_c} + \sin\left(3\sin^{-1}\frac{\sqrt{R_c^2 - R^2}}{H_c}\right)\right.$$
$$\left. + 7\sqrt{1 - \frac{h_c^2}{H_c^2}} + \cos\left(3\sin^{-1}\frac{h_c}{H_c}\right)\right].$$

(5.11b)

The total weighted volume is calculated as spherical cover with infinite thickness[3]

$$V'_{total} = \left(\frac{p}{4\pi\epsilon_0}\right)^2 \left(\frac{\pi}{6R_c^3}\right)\left[-7\frac{\sqrt{R_c^2 - R^2}}{H_c} + \sin\left(3\sin^{-1}\frac{\sqrt{R_c^2 - R^2}}{H_c}\right) + 8\right]. \quad (5.12)$$

In the limit $R_c = R$, the spherical calotte is a half sphere. In this case, several terms vanish and equations 5.11 and 5.12 yield the equations for spherical particles 5.7 and 5.8. The prefactor differs by 2, because only one half of the rod is considered in the calculations.

5.4.3 Determining the Dielectric Function of Gold Nanoparticles

Electron density in Gold Nanoparticles   In bulk gold, the valence electron density is defined by

$$n_{bulk} = R\frac{Z \cdot \rho}{A} = 6.02 \cdot 10^{23}\,\text{mol}^{-1}\frac{1 \cdot 1932\,\text{kg}\,\text{m}^{-3}}{0.19697\,\text{kg}\,\text{mol}^{-1}} \approx 59\,\text{nm}^{-3} \quad , \quad (5.13)$$

with Avogadro constant R, valence number Z, density ρ, and atomic mass A.
The electron density decreases at surfaces, because only one side contributes to the electron gas. This effect becomes relevant for nanoparticles. The inset of figure 5.15 shows the relative change of n as a function of surface to volume ratio.
The variation of n changes the plasma frequency $\omega_P \propto \sqrt{n}$. According to equation 2.4a, the change of the dielectric function is

$$\Delta\epsilon = \epsilon_{particle} - \epsilon_{bulk} = \frac{\omega_{P,particle}^2 - \omega_{P,bulk}^2}{\omega^2} \quad . \quad (5.14)$$

Table 5.5 lists the determined values for $\Delta\epsilon$, the ratio A/V, and n. Hereby, $\Delta\epsilon$ is the average value for the observed spectral range. Especially for GNS, the dielectric functions of bulk gold and particles diverge strongly, causing errors in $\Delta\epsilon$ and the calculated electron density n.

---

[2]See appendix for detailed calculation.
[3]See appendix for detailed calculation.

Particle Type	A/V [1/m]	n [1/nm^{-3}]	$\Delta\epsilon$
GNS 20	0.3	57 ± 1	0.5 ± 0.5
Rod 1	0.277	50 ± 2	4.9 ± 0.7
Rod 2	0.205	54 ± 0	1.8 ± 0.7
Rod 3	0.16	57 ± 2	0.7 ± 0.1

Table 5.5: Dependence of electron density n and change of dielectric function $\Delta\epsilon$ on surface-volume-ratio A/V. For bulk gold, the electron density is $n = 59\,\mathrm{nm}^{-3}$. The error in $\Delta\epsilon$ for GNS 20 is caused by the strong divergence of the determined dielectric function of particles and the function of bulk gold (see inset of fig 5.16).

Dielectric Function of GNSs To determine the dielectric function for spherical particles, two data points are measured: One for GNSs in aqueous suspension with $\epsilon_m = \epsilon_{H_2O} = 1.77$, and one for fully embedded GNSs with $\epsilon_m = \epsilon_{poly} = 2.42$. The wavelength of the LSPR is measured by spectroscopy and the real part of ϵ_{Au} is calculated by the resonance condition $0 = \epsilon_{Au} + u\epsilon_m$. The interpolation between both values is taken as dielectric function. The inset of figure 5.16 shows the real part of ϵ_{Au} for spherical particles.

Dielectric Function of GNRs The dielectric function of each type of GNRs is determined by interpolating the measured data points of water-embedded and polymer-embedded particles, shown in figure 5.15. Both values are afflicted by errors, caused by the error of the shape factor u. Therefore, the interpolation is chosen to fit a third data point. This point allocates the measured wavelength of the uncovered particles to the value of $\epsilon_{Au} = -u\epsilon_m$, whereof ϵ_m is calculated by the model.
For all three types of GNRs, the interpolations are localized above ϵ_{Au} of bulk gold. With increasing particle size, the difference between particle and bulk functions decreases. This illustrates the transition from nanoparticle to bulk material.

5.4.4 Simulating the LSPR Peak Position

LSPR Peak Position of GNSs Figure 5.16 shows the measured peak positions of 20 nm GNSs as function of the cover thickness d. With known weighted volumes, the dielectric function of the environment was determined according to equations 5.2 and 5.3. For uncovered particles ($d_0 = 0\,\mathrm{nm}$) with a subsidence depth of $t = 5.5\,\mathrm{nm}$, the dielectric function starts with $\epsilon_m = 1.41$. After adding 35 nm of polymer, the value saturates at $\epsilon_m = \epsilon_{poly} = 2.46$. With known ϵ_m, the value of $\epsilon_{Au} = 2\epsilon_m$ is defined. The corresponding wavelength can be read off the dielectric function, given in the inset of figure 5.16.
The simulation fits all measured data points within the error bars.

Longitudinal LSPR Peak Position of GNRs The measured longitudinal LSPR wavelengths are shown in figure 5.17. For the simulation of these data, it is not significant, whether the cylindric part of the particles is taken into account or not.
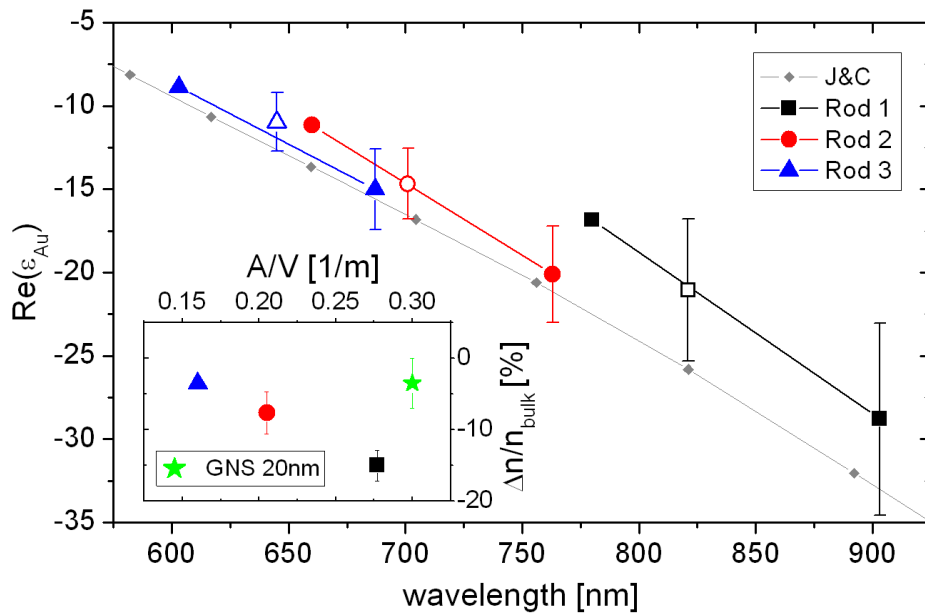
Figure 5.15: Dielectric functions of the GNRs. Data points with error bars represent fully embedded GNRs in aqueous solution ($\epsilon_{H_2O} = 1.77$, open symbols) and polymer ($\epsilon_{poly} = 2.47$, solid symbols). The interpolation between both values is adjusted within the errors to fit the measured LSPR peak positions (solid symbols without error bars) of uncovered particles. The dielectric function of particles is higher than ϵ_{Au} of bulk gold (Johnson and Christy [37]). This is caused by the reduced electron density n, plotted as function of the surface-volume-ratio in the inset. All error bars yield from the errors of the shape factors u.
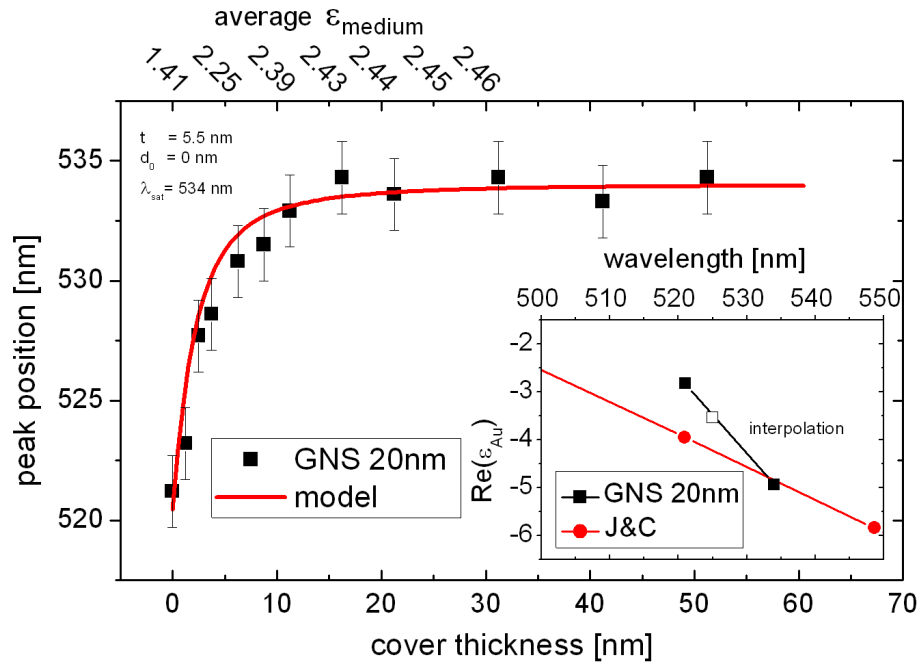
Figure 5.16: The peak position of the surface plasmon absorption shifts with increasing thickness of the polymer cover. The data points are fitted by the two-phase-media model. It uses the dielectric function of the environment (upper axis) and the dielectric function of the particles, shown in the inset. ϵ_{Au} is interpolated between the values of GNSs in water (open square) and GNSs embedded in polymer (right solid square).
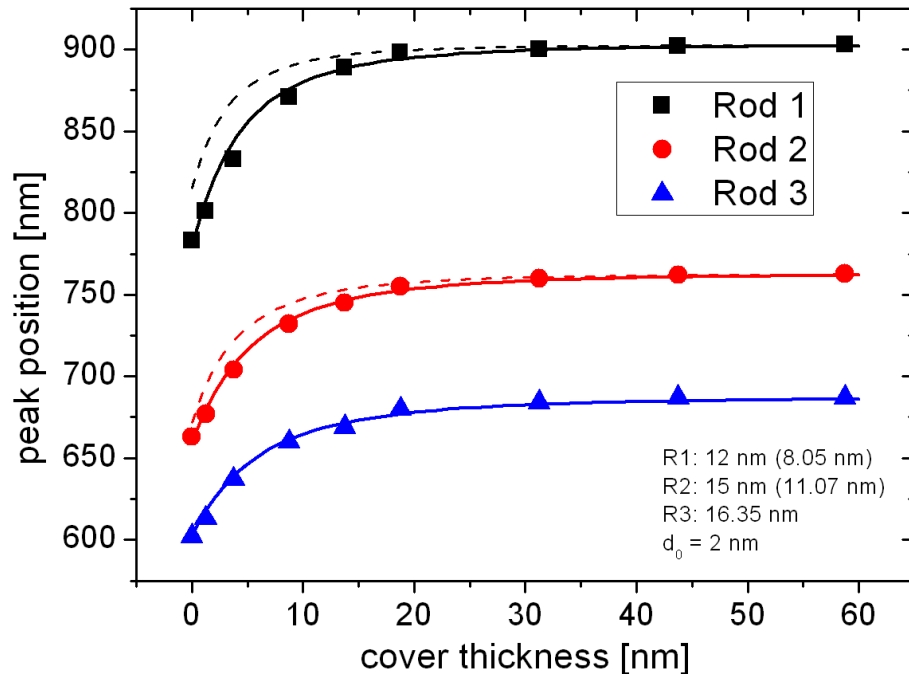
Figure 5.17: The longitudinal plasmon absorption peaks shift when the GNRs are covered with polymer. Simulating with $R_c = R$ overestimates the data (dashed lines). By increasing the curvature radii, the simulation fits (solid lines). All parameters are given in table 5.3.

Type	R_c [nm]	R [nm]	L [nm]	t [nm]	d_0 [nm]	u
GNS 20	10	10	0	5.5	0	2
Rod 1	12	8.05	0 (44.4)	2.7	2	11.9
Rod 2	15	11.07	0 (44.7)	4.0	2	8.3
Rod 3	16.35	16.35	0 (44.3)	2.3	2	6.2

Table 5.6: Applied parameters to simulate the LSPR wavelengths of gold nanoparticles. Data and simulations are plotted in figures 5.16 and 5.17. The values in brackets were determined by SEM measurements, but not used for the fit.

Type	f_{air}	$f_{embedded}$
Rod 1	0.312	0.105
Rod 2	0.158	0.046
Rod 3	0.168	0.050

Table 5.7: Filling factors for uncovered and fully embedded GNRs.

The error is below one percent and could be reduced further by adjusting the dielectric function of the particles. Therefore, the shown simulations focus only on the spherical end parts.

The SEM characterization measurements in figure 5.1 do not determine the curvature radii R_c exactly. The assumption of spherical caps ($R_c = R$) may be obvious, but the simulation overestimates the polymer volume for Rod 1 and Rod 2 (dashed lines in fig. 5.17). Therefore, the radii R_c were set to 12 nm and 15 nm, respectively. This results in a decreased surface of the particles and the (weighted) polymer volume is reduced. Via equation 5.3, the value of the dielectric function of the medium ϵ_m decreases.

By adjusting the dielectric function as described in subsection 5.4.3, the simulation fits the data. The fits are shown as solid lines in figure 5.17. Table 5.6 summarizes all applied values.

6 Picosecond Acoustics

The absorption of an ultrashort light pulse in a thin metal transducer layer leads to expansion on a picosecond timescale. The expanding transducer compresses the adjacent substrate and releases a strain wave that propagates into the medium at speed of sound. As explained in section 2.2, light can scatter from such a strain pulse. Optical pump-probe experiments visualize this time-domain Brillouin scattering (TDBS).

In UDKM group, the samples investigated by picosecond acoustic experiments can be classified into two groups: crystalline samples such as SRO and LSMO, grown by pulsed laser deposition, and amorphous samples such as thin metal films or polyelectrolyte multilayers on fused silica substrates. This chapter focuses on the second group, especially on the non-metallic polyelectrolytes. Dye-containing polymer layers are introduced as transducer and compared to aluminum by optical Brillouin scattering experiments. Measurements and data analysis aim a quantification of the excited phonon spectrum, to determine the efficiency of each transducer. The efficiency of each transducer material is highlighted from different perspectives: the ratio of TDBS signal amplitude to absorbed energy, the damage threshold of the transducer material, and the effort of sample preparation.

The last section treats the dynamics within a sample and explains the temporal development of strain waves. Based on this model, a simulation is shown and compared to the experimental data.

6.1 Experimetal Setup

The Brillouin scattering experiments were carried out with an ultrafast pump-probe laser setup schematically shown in figure 4.3. The laser provides pump light with either 800 nm wavelength or its second harmonic of 400 nm. All samples were probed from the back side to avoid signal losses due to absorption in the transducer layer. Incident angle of the s-polarized probe was 7°. The samples were pumped from the front with p-polarized light under an angle of 21°. The polarizations were chosen to increase the reflectance for the probe beam and decrease it for the pump.

6.2 Sample Materials and Structures

Every thin layer of absorbing material can be used as transducer to generate strain waves. This work focuses on organic polyelectrolytes and the metal aluminum, both based on fused silica substrates. The following paragraphs introduce the samples that were used in the experiments. Table 6.1 summarizes all relevant parameters.

(a) PAzo structure

(b) trans state
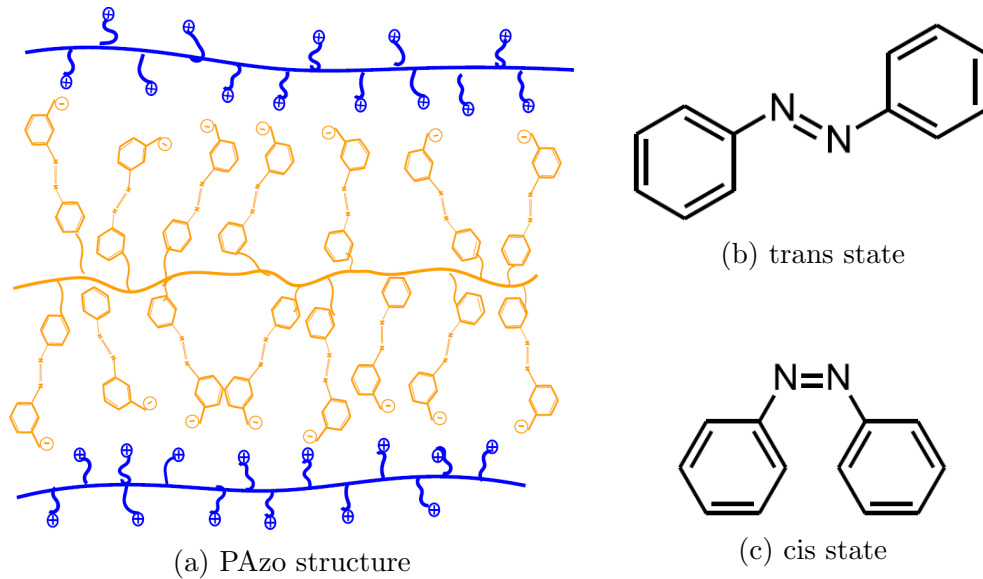
(c) cis state

Figure 6.1: The thickness of PAzo (yellow) and PAH (blue) multilayers shown in (a) depends on the isomerization state of the azo side chains. The length of the molecule is reduced by switching from trans state (b) to cis state (c). The sketch in (a) is taken with permission from literature [73].

Metal Transducer: Aluminum The first experiments deal with the metal aluminum. By vapor deposition, an aluminum film of $52\,\mathrm{nm}$ thickness was grown on a fused silica substrate. For an incident angle of $21°$ and p-polarization, the absorption of such a transducer layer is $7.7\,\%$ for $\lambda = 400\,\mathrm{nm}$ and $16.2\,\%$ for $\lambda = 800\,\mathrm{nm}$. Both values were measured by determining the reflection and the transmission in the experimental laser setup. Since the metal film does not transmit any light, the major part is reflected.

Polyelectrolyte Multilayers as Transducer Material In a second set of samples, polyelectrolyte multilayers were used as transducer materials. Alternating layers of the polyelectrolytes PAzo and PAH were deposited on fused silica substrates as described in chapter 3. The sample was capped with transparent doublelayers of PSS/PAH to reduce possible evaporation due to laser excitation. Figure 6.1 sketches the structure of a PAH/PAzo/PAH multilayer. The PAzo side chains are perpendicular to the polymer backbone in up- or downward direction. If free azo molecules are excited, they undergo a trans-cis isomerization that reduces the length from $90\,\mathrm{\AA}$ to $60\,\mathrm{\AA}$. If all azo chains flip from *trans* to *cis* state, the whole layer would be expected to shrink in thickness. On the other hand, the on ultrashort timescales the film cannot expand in plane as demanded by Poisson's ratio. To verify whether the layer shrinks or expands, another reference sample was made. It consists of transparent PSS/PAH multilayers that were interspersed with porphyrin (POR) dye molecules. Similar to PAzo, POR absorbs in the near UV, but does not change its structure after excitation. The absorption spectra of both samples are plotted in figure 6.2. These data do not take saturation at high pulse intensities into account. For the high intensity pump pulses, the absorption coefficients for $400\,\mathrm{nm}$ p-polarized
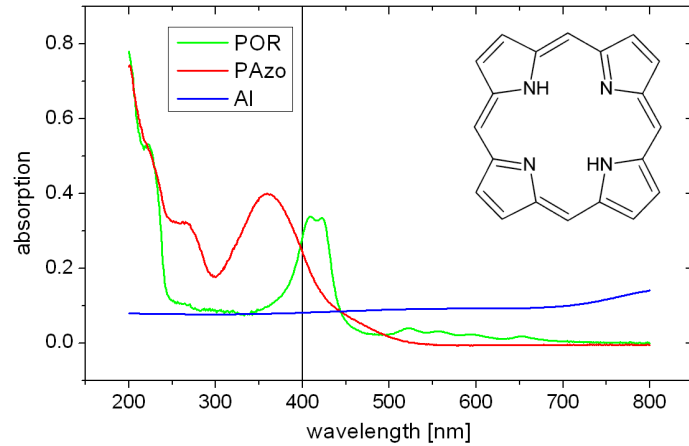
Figure 6.2: The absorption A spectra of POR, PAzo, and Al samples calculated from transmission T and reflection R measurements by $A = 1 - R - T$. Both samples were tuned to have similar absorption at $400\,\text{nm}$ wavelength. These data do not consider the saturation effects that occur at high pump intensities. The absorption data measured under experimental conditions are given in table 6.1. The inset shows the structure of a porphyrin dye molecule.

light are $14.5\,\%$ (POR) and $12.8\,\%$ (PAzo), respectively.

Metal-Organic Transducer Materials The last set of samples are combinations of polyelectrolytes and aluminum. As basic idea, an aluminum layer was used as reflector for the probe light. These samples had identical optical properties seen from substrate side. In this case, the reflection coefficient r in equation 6.4 is fixed and independent of any transducer material. Thus, the measured Brillouin signals of these samples allow direct conclusions on the amplitude of the induced strain. The samples are aluminum covered fused silica substrates, identical to the sample described first. On this basic structure, layers of polyelectrolytes are added. One sample is prepared with PAzo/PAH as transducer, covered with transparent layers of PSS/PAH. The multilayers have a thickness of $68\,\text{nm}$ and $15\,\text{nm}$, respectively. Another sample is made for reference experiments. It consists of PSS/PAH multilayers with $75\,\text{nm}$ thickness. Possible difficulties with binding hydrophilic polyelectrolytes to a metal surface are discussed in chapter 3. The absorption coefficients are given in table 6.1.

6.3 Data Analysis

This section describes the data processing from raw data to a value that quantifies the induced strain. A pump-probe experiment records the time-dependent transmission and reflection of a sample. Both contain the signal of Brillouin scattering, so it is sufficient to focus on the relative change of reflection. The typical beam paths of a Brillouin scattering experiment are depicted in figure 2.3a. The measured change
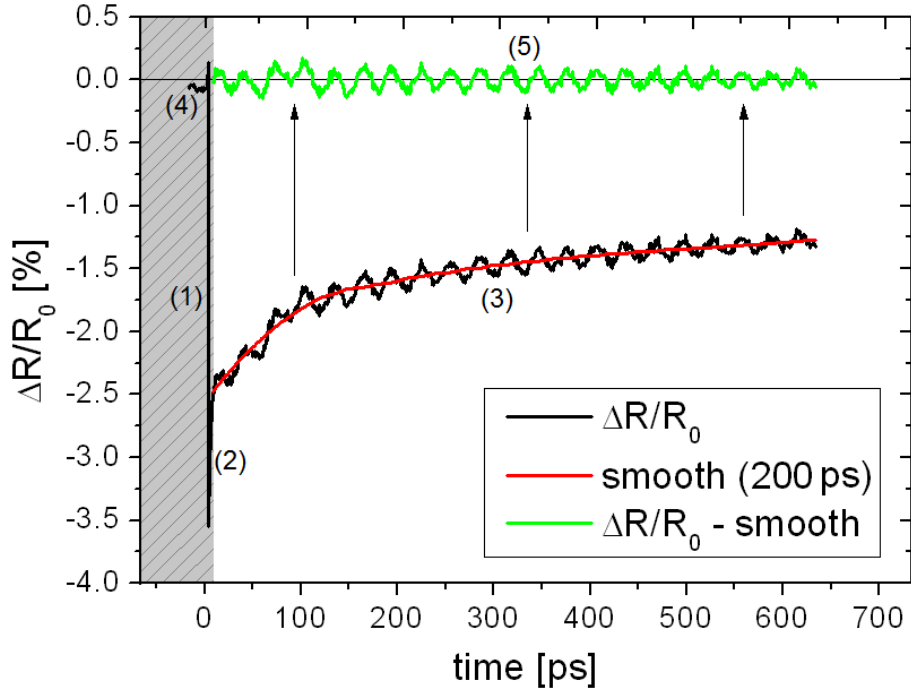
Figure 6.3: Extraction of the oscillation signal, exemplary shown for the POR sample at a probe wavelength of $730\,\mathrm{nm}$. The raw $\Delta R/R_0$ data are plotted as black line.

(1) Due to the excitation of the electrons at $t = 0\,\mathrm{ps}$, the dielectric function changes, causing a strong change of the reflection.

(2) Within few picoseconds ($0\,\mathrm{ps} < t < 10\,\mathrm{ps}$), the energy dissipates via electron-phonon coupling into coherent and incoherent vibrations of the polyelectrolyte molecules.

(3) The signal change due to incoherent vibrations (heat) is represented by the red line, calculated by smoothing the raw data for $t > 10\,\mathrm{ps}$. While the heat dissipates, the change of reflection decays.

(4) After $200\,\mathrm{\mu s}$ (repetition rate of the laser), a small amount of heat is still in the sample, causing the negative offset in the raw data for $t < 0\,\mathrm{ps}$.

(5) The excited coherent vibrations describe the hypersound strain waves that are detectable by time-domain Brillouin scattering (TDBS). They cause a cosinusoidal oscillation (green line) that is calculated as the difference between raw data (black) and smooth (red).

Transducer	$A_{400/800}$ [%]	Structure	Thickness [nm]
Al	7.7 / 16.2	Al	52
(PAzo/PAH)/Al	34.5 / 36.5	Al (PAzo/PAH)$_{15}$ (PSS/PAH)$_6$	52 + 68 + 15
(PSS/PAH)/Al	10.0 / 27.6	Al (PSS/PAH)$_{30}$	52 + 75
(PAzo/PAH)/(PSS/PAH)	12.8 / -	(PAzo/PAH)$_{15}$ (PSS/PAH)$_6$	68 + 15
(PSS/PAH)+POR	14.5 / -	(PSS/PAH)$_8$ [POR/PAH (PSS/PAH)$_4$]$_3$ POR/PAH	90

Table 6.1: Overview of the samples, used for Brillouin scattering experiments. The absorption coefficients A for 400 nm and 800 nm were determined in the laser setup with intensities above the saturation limit. Due to saturation, the PAzo and POR samples actually absorbed less energy of the pulsed laser light than predicted by the absorption measurements, shown in figure 6.2. Thus, the values given in this table are used for normalization.

of reflection is defined as

$$\frac{\Delta R}{R} = \frac{R' - R}{R}. \tag{6.1}$$

The value $R = r^2$ is the reflected intensity of the static (unpumped) sample. The value for the pumped sample contains the contribution of the sound wave r_s. It interferes with the reflection of the static interfaces r', resulting in a total intensity

$$R' = r'^2 + r'r_s \cos\phi + r_s^2. \tag{6.2}$$

The scattering at the strain pulse is so weak that the term r_s^2 can be neglected. Using this approximation, formula 6.1 results in

$$\frac{R' - R}{R} = \frac{r'^2 + r'r_s \cos\phi + r_s^2 - r^2}{r^2} \tag{6.3a}$$

$$\approx \frac{r'^2 - r^2}{r^2} + \frac{r'r_s \cos\phi}{r^2} \tag{6.3b}$$

The sum in formula 6.3b describes the measured signal. The first summand corresponds to the thermal background that decreases slowly for increasing time delay between pump and probe beam. The second summand contains the information about the induced strain. A typical measurement and the further signal processing are illustrated in figure 6.3. To extract the oscillation, values before time zero are neglected. The strong electronic response is also not taken into account. The thermal background is estimated by smoothing the data over a time window of 200 picoseconds. The difference of raw data and thermal background is the cosinusoidal oscillation with a period of several picoseconds. Within the observed time delays, the deviation of r and r' is below one percent. Assuming both as identical approximates the second summand in equation 6.3b to

$$\frac{r'r_s \cos\phi}{r^2} \approx \frac{r_s \cos\phi}{r}. \tag{6.4}$$

For investigations of amplitude r_s/r and phase ϕ of the TDBS oscillation, a fast Fourier transform (FFT) is done. Figure 6.4 depicts the application of a low-pass
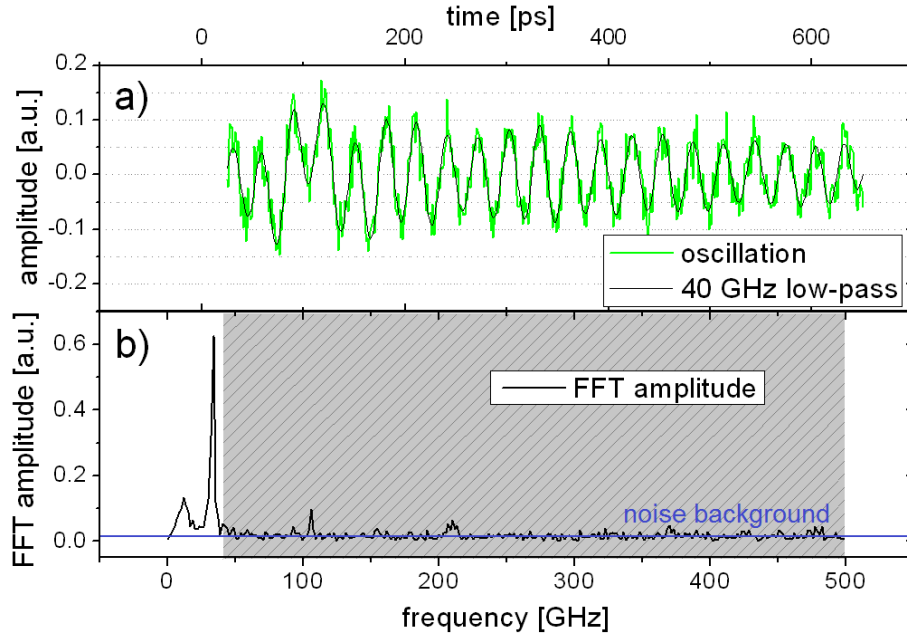
Figure 6.4: Determination of the excited phonon spectra, exemplary shown for the POR sample at 550 nm. A fast Fourier transform (FFT) of the noisy TDBS oscillation data plotted as green line in (a) results in the frequency spectrum plotted in panel (b). The main peak marks the basic frequency at about 35 GHz. The integral of this peak, subtracted by the noise background (blue line), is taken as amplitude of the TDBS oscillation signal. A low-pass filter (shaded area) is applied to remove the contribution of high frequencies from the oscillation signal. The inverse FFT of these filtered data is plotted as black line in (a).

filter to analyze the phase. It also shows the strong peak of the fundamental oscillation frequency. Within a width of 6 GHz, the peak is integrated to gain a value of the amplitude r_s/r. This FFT amplitude is proportional to the strain [74]. The noise background is determinded by outlying data that were not considered in the integral. This process is done for every measured wavelength, typically ranging from 450 nm to 750 nm. The FFT amplitude is proportional to r_s/r. Hence, the data are multiplied with the reflection coefficient r of the particular sample (see figure 6.5). Since the measurement is more sensitive for high wavenumbers, the data are divided by $k = 2\pi/\lambda$ [45]. This is because the wave trains act as reflection interfaces. On a given spatial distance (length of the strain wave), the number of wave trains is higher for high values of k.

For comparison, each spectrum is normalized to the pump intensity. At sufficiently low pump fluence, a linear correlation of pump power and induced strain can be assumed [75, 76]. The data proceeding results in an FFT-spectrum that represents the spectral occupation numbers of phonons in the spectral range that is accessible with the visible probe light (see fig. 2.4). Although the FFT-values are given in arbitrary units, the identical proceeding of each data set ensures comparability between all analyzed samples.
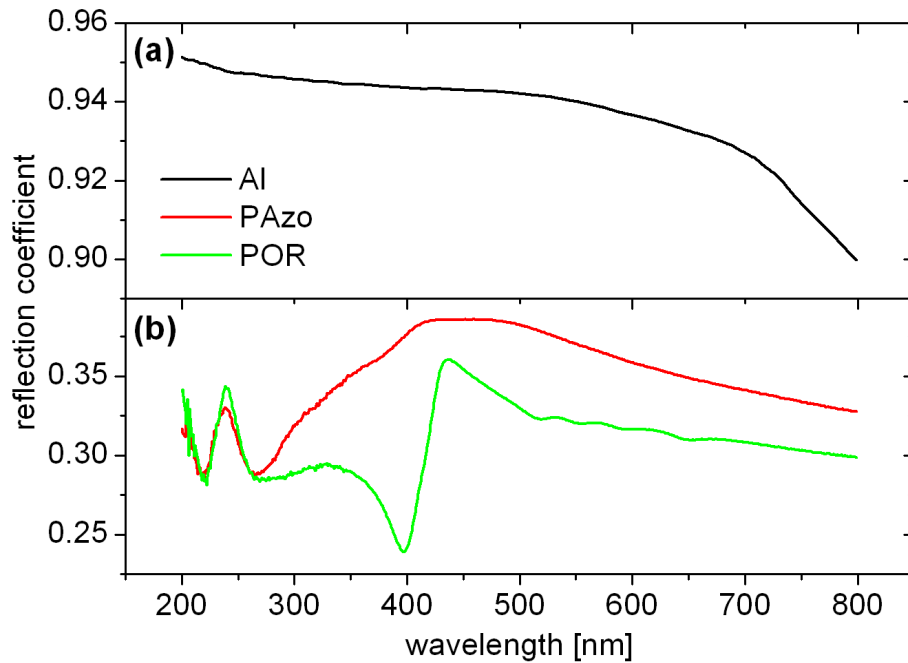
Figure 6.5: Reflection coefficients of interfaces, where the probe beam is reflected: Al/quartz, PAzo/air + PAzo/quartz, and POR/air + POR/quartz. The reflection from Al/air interface is neglected due to the very low transmittance of the 52 nm Al film.
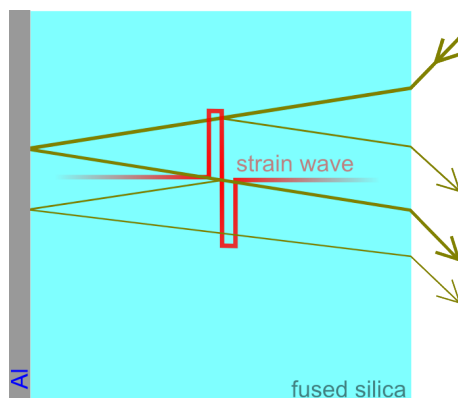
Figure 6.6: Optical pathways within a sample with high reflecting transducer layer. Multiple reflections enable Brillouin scattering from front and back side. Both interfere destructively, resulting in an attenuation of the TDBS signal.

(a) Oscillation data

(b) Spectral FFT data
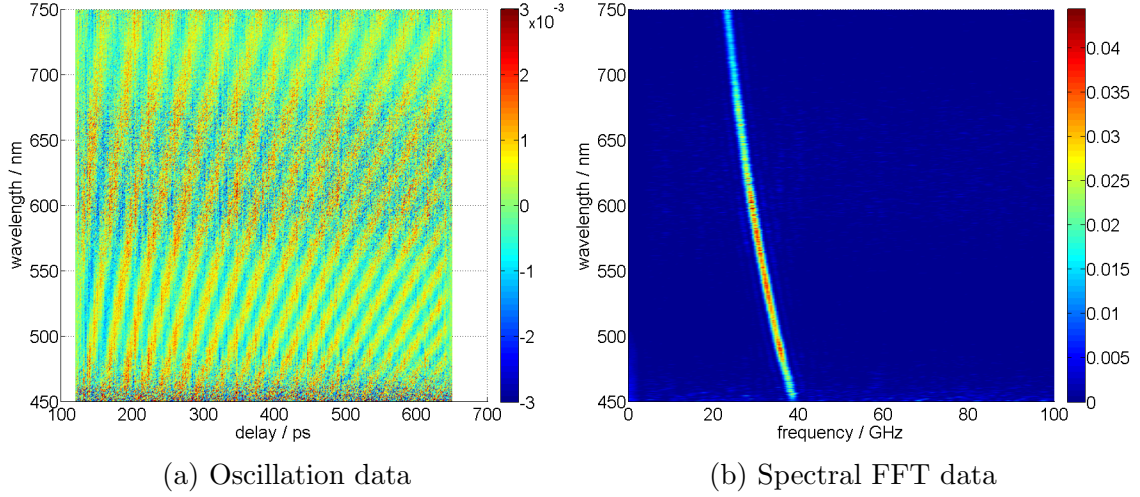
Figure 6.7: The fan-like struture in the oscillation data (a) results in a curved development of the basic frequency in the FFT plot (b).

6.3.1 Signal Attenuation at High Reflecting Transducers

Highly reflecting transducers enable detectable Brillouin scattering from both sides of the strain pulse. As sketched in figure 6.6, the reflection from the transducer interface probes the strain wave from the back side. Thus, the reflection term in equation 6.2 expands to

$$R' = r'^2 + r_{s,f}^2 + r'^2 r_{s,b}^2 + r' r_{s,f} \cos \phi_1 + r'^3 r_{s,b} \cos \phi_2 + r_{s,f} r_{s,b} \cos \phi_3 \qquad (6.5)$$

where r' is the reflection coefficient of the interface of transducer and substrate. The reflection coefficients of the sound wave are $r_{s,f}$ and $r_{s,b}$, probed from front (f) and back (b) side, respectively. Due to very low intensity, second order terms of r_s can be neglected. In analogy to equation 6.4, the measured signal is proportional to $(r_{s,f} \cos \phi_1 + r'^2 r_{s,b} \cos \phi_2)/r$. The light scattered from the front side undergoes a phase shift of π. Thereby, both terms interfere destructively. In case of aluminum ($r' \approx 0.9$), the total oscillation amplitude is reduced up to $(1 - r'^2) \approx 0.2$. This value marks the minimum, since the additional phase shifts at the transducer interface only sum up to zero for normal incidence. All measurements were performed under an incident angle of $7°$, resulting in a signal that is slightly higher than the theoretical minimum. For a quantitative comparison of the determined phonon spectra, this effect must be taken into account.

6.4 Results and Discussion

6.4.1 Determining the Sound Velocity of Fused Silica

According to equation 2.20, the oscillation period rises linearly with increasing probe wavelength. This results in a fan-like pattern as shown in figure 6.7a. The same effect is visualized by the FFT plot in figure 6.7b. Here, the frequency dependence on the wavelength is inverse, which results in a curved development. Both plots
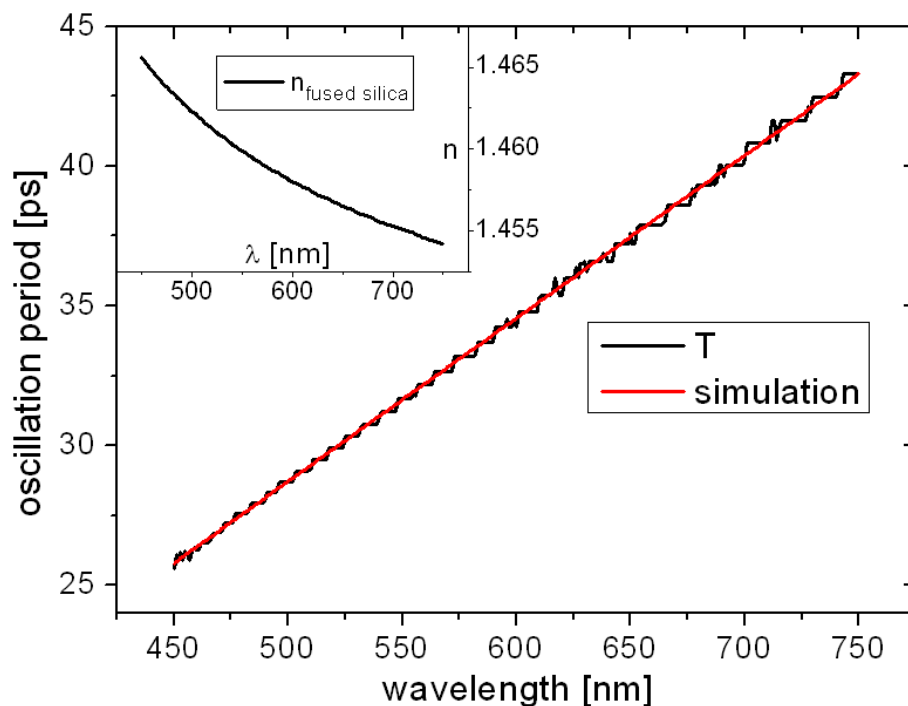
Figure 6.8: Oscillation period calculated from the FFT data (black). The steps are caused by the finite resolution of the measurement. The linear fit of the data (red) yields a sound velocity in fused silica of $v_s = 6.0\,\mathrm{nm/ps}$. The inset shows the refractive index of fused silica, measured by ellipsometry.

show the data of the POR sample. Since the oscillation period does not depend on the transducer material but on the substrate, it is sufficient to do the analysis on this sample. Figure 6.8 shows the spectral dependence of the oscillation amplitude $T = f^{-1}$. It is calculated from the maxima of the FFT data in figure 6.7b. By transposing equation 2.20, the sound velocity of the fused silica substrate can be calculated

$$v_S = \frac{\lambda}{2 T_S n(\lambda) \cos \alpha}. \tag{6.6}$$

The incident angle of the probe light was $\alpha = 7°$, yielding a sound velocity of $v_s = 6.0\,\mathrm{nm/ps}$. This value was found for all analyzed samples. It is in excellent agreement with the value $v_s = 5.968\,\mathrm{nm/ps}$ found in literature [77].

6.4.2 Investigations of the Transducer Efficiencies

The following paragraphs treat the investigations of the TDBS oscillation amplitudes. In contrast to the oscillation period, the amplitudes depend on the transducer material and have to be analyzed separately. The materials aluminum (Al), polyelectrolytes (PAzo/PAH multilayers and POR-doped PSS/PAH multilayers), and combinations of both are compared to each other.

Metal Transducer: Aluminum Figures 6.9a and 6.9b show TDBS oscillation signals of an aluminum transducer on a fused silica substrate after smoothing with a

(a) Al: $\lambda = 800\,\text{nm}$, $I = 30.0\,\text{mJ/cm}^2$ (b) Al: $\lambda = 400\,\text{nm}$, $I = 7.7\,\text{mJ/cm}^2$
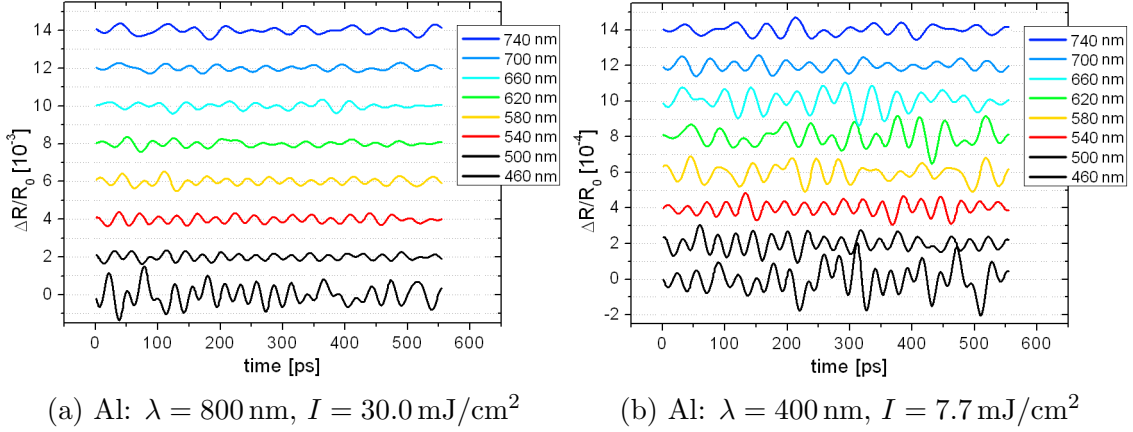
Figure 6.9: Both plots show TDBS oscillation signals of an fused silica substrate, excited via an 52 nm aluminum transducer. The data were smoothed by an FFT low-pass filter and shifted for visibility. It is noted that the scale in (a) is one order of magnitude higher than in (b). Strong temporal variations of the amplitude indicate noisy data.

low-pass filter. The first measurement applied 800 nm pump pulses with an intensity of $30.0\,\text{mJ/cm}^2$. Within a spectral range from 500 nm to 580 nm, clear oscillations with amplitudes in the order of $5 \cdot 10^{-4}$ occur. The data at 460 nm and above 580 nm wavelength are very noisy. They are not considered in the further discussion. In the second measurement, the same Al sample was pumped with an intensity of $7.7\,\text{mJ/cm}^2$ at a wavelength of 400 nm. Compared to the first measurement, the oscillation amplitude drops to a value of $5 \cdot 10^{-5}$, because the absorption and the pump intensity are lower. Clear oscillations are only visible in the range of 540 nm. The exact values of amplitudes are calculated from the FFT data. Figure 6.10 shows the FFT amplitude spectra for both measurements. As explained in section 6.3, the data are normalized to the pump intensity, the reflection coefficient of the probe light, and the k-vector. The derived normalized amplitudes are higher for the Al sample pumped at 400 nm wavelength. This disagrees with the observation that the absorption of the Al transducer is roughly two times higher at 800 nm wavelength than at 400 nm (see tab. 6.1). One possible reason might be that the intensity of the 800 nm pump beam was above the limit of the assumed linear correlation between pump intensity and induced strain. The additional normalization to the absorption as shown in figure 6.10b increases the distance between both curves. Assuming a linear response to the excitation energy, both curves should be identical. Due to the signal attenuation for high reflecting samples, discussed in section 6.3.1, especially the data of the second measurement are very noisy.

Polyelectrolyte Transducers: (PAzo/PAH) and POR-Doped (PAH/PSS) multilayers The TDBS oscillation signals of the polyelectrolyte transducers are shown in figures 6.11a and 6.11b. Both samples were pumped at 400 nm wavelength with an intensity of $7.7\,\text{mJ/cm}^2$. For the PAzo sample, the TDBS oscillation signal is very strong between 580 nm and 740 nm wavelength, but it vanishes below 540 nm. In the maximum at about 700 nm, the amplitude of the $\Delta R/R_0$ oscillation is slightly

Figure 6.10: FFT amplitudes of TDBS oscillations induced by an aluminum transducer. The plot in (a) shows the FFT amplitude, normalized to pump intensity, reflection coefficient, and k-vector. In panel (b) the FFT data additionally are normalized to the absorption.

(a) PAzo: $\lambda = 400\,\text{nm}$, $I = 7.7\,\text{mJ/cm}^2$ (b) POR: $\lambda = 400\,\text{nm}$, $I = 7.7\,\text{mJ/cm}^2$
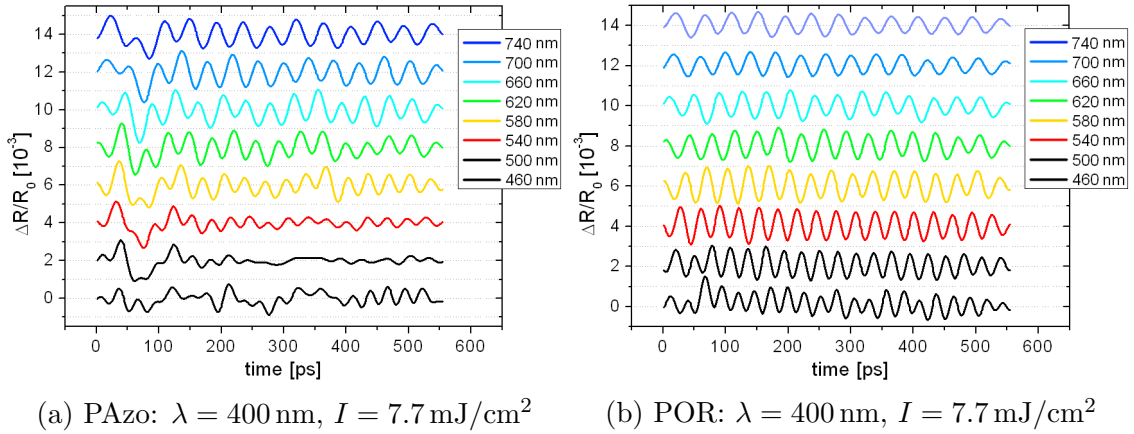
Figure 6.11: The TDBS oscillation signals in fused silica, induced by PAzo/PAH multilayers are shown in (a). Figure (b) shows the data of the POR sample. All data were smoothed by FFT low-pass filter and shifted for visibility. For the PAzo sample, no clear oscillations can be extracted from the $\Delta R/R_0$ data for probe wavelength below 540 nm.
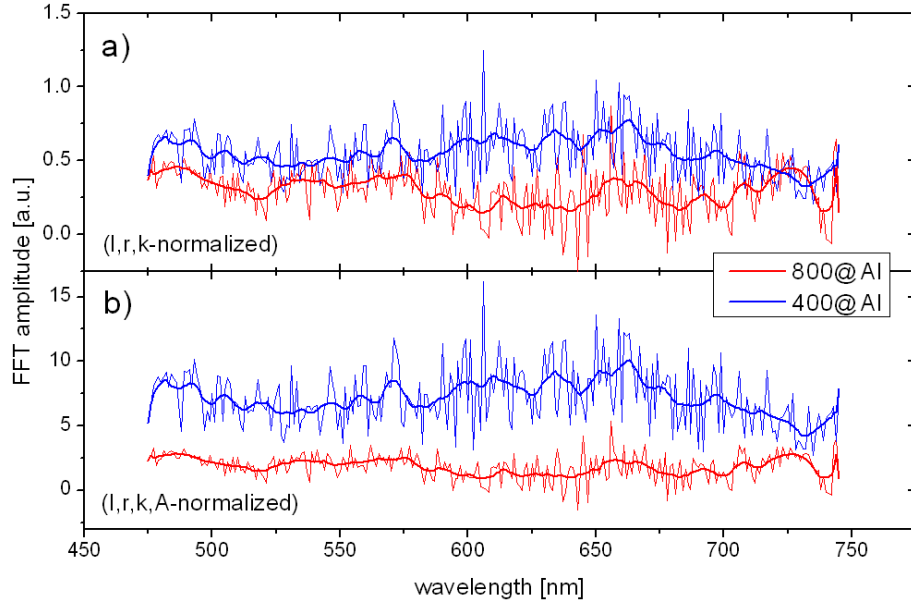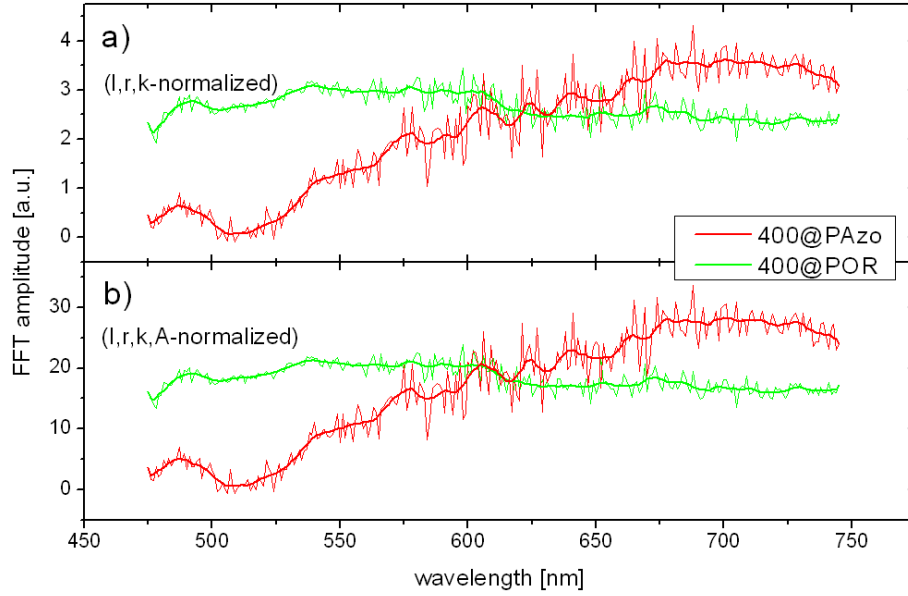
Figure 6.12: FFT amplitudes of TDBS oscillations induced by polyelectrolyte transducers. The plot in (a) shows the FFT amplitudes, normalized to pump intensity, reflection coefficient, and k-vector. In panel (b) the FFT data additionally are normalized to the particular absorptions, given in table 6.1.

higher than $0.5 \cdot 10^{-3}$. The measurement of the POR sample shows clear oscillations across the whole observed spectral range. At 540 nm wavelength, the oscillation amplitude has a maximum value close to $1 \cdot 10^{-3}$ for the first 150 picoseconds. At later delay times, the amplitude is almost halved. This indicates a damping of phonons within the propagation medium. Section 6.5) treats the topic of phonon damping. The FFT amplitude plots shown in figure 6.12a represent the same distributions: The excited phonon spectra of the PAzo transducer increases from almost zero at 500 nm to a value of 3.5, while the POR transducer varies mainly between values of 2.5 and 3.0. Since both samples have similar absorption, the normalization to the total absorbed energy does not change the relative differences (see fig. 6.12b). The observed trends depend on optically accessible part of the excited phonon spectrum. As pointed out in figure 2.4 it is given by the sample structure, particularly with regard to the thickness. In section 6.5 the measured phonon spectra of the PAzo sample is exemplarily verified by a simulation.

One can conclude that polyelectrolyte transducers work very well on fused silica substrates in the sense that a TDBS signal can be easily found. Comparing the calculated phonon spectra of the PAzo and POR samples indicates that there is no enhancement of strain due to the *cis-trans* isomerization of the PAzo groups. With respect to the signal attenuation for the highly reflecting Al samples, the calculated phonon spectra suggest a similar efficiency of polyelectrolyte and Al transducers in terms the generation of strain.

Hybrid Materials: Polyelectrolyte Multilayers on Al Figure 6.13b shows the TDBS oscillations of a fused silica substrate excited by an transducer consisting

(a)

(b)

(c)

(a)   (PAzo/PAH)/Al:
$\lambda = 800\,\text{nm},\ I = 35.0\,\text{mJ/cm}^2$

(b)   (PAzo/PAH)/Al:
$\lambda = 400\,\text{nm},\ I = 13.8\,\text{mJ/cm}^2$

(c)   (PSS/PAH)/Al:
$\lambda = 800\,\text{nm},\ I = 35.0\,\text{mJ/cm}^2$
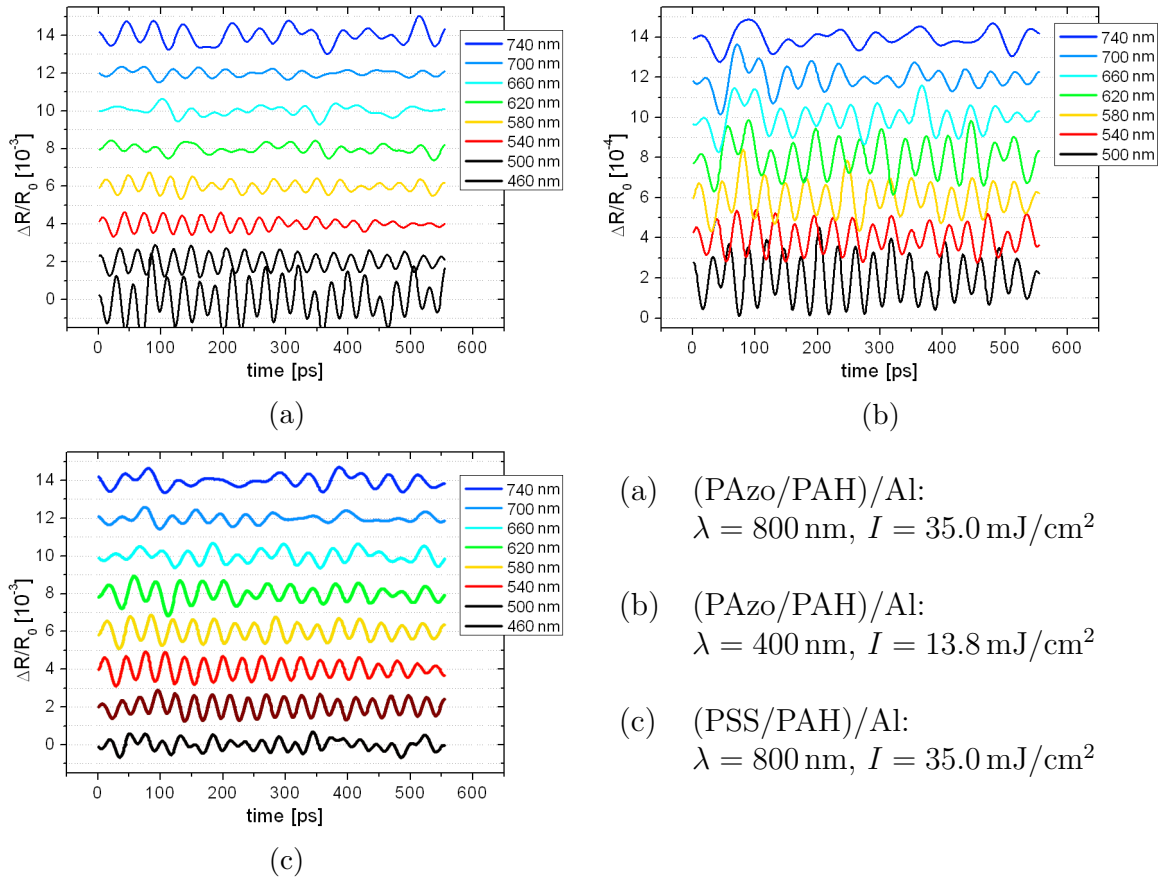
Figure 6.13: The plots show TDBS signals induced by polelectrolyte covered aluminum transducers. Excitation of PAzo/PAH multilayers on aluminum with 400 nm wavelength results in weak oscillation amplitudes. For 800 nm pump wavelength, the polyelectrolytes do not absorb any light, but act as optical anti-reflection coating. This increases the absorption (see tab. 6.1) and enhances the measured signals. Temporal variations of the amplitude indicate a bad signal-to-noise ratio. All signals are shifted for visibility.
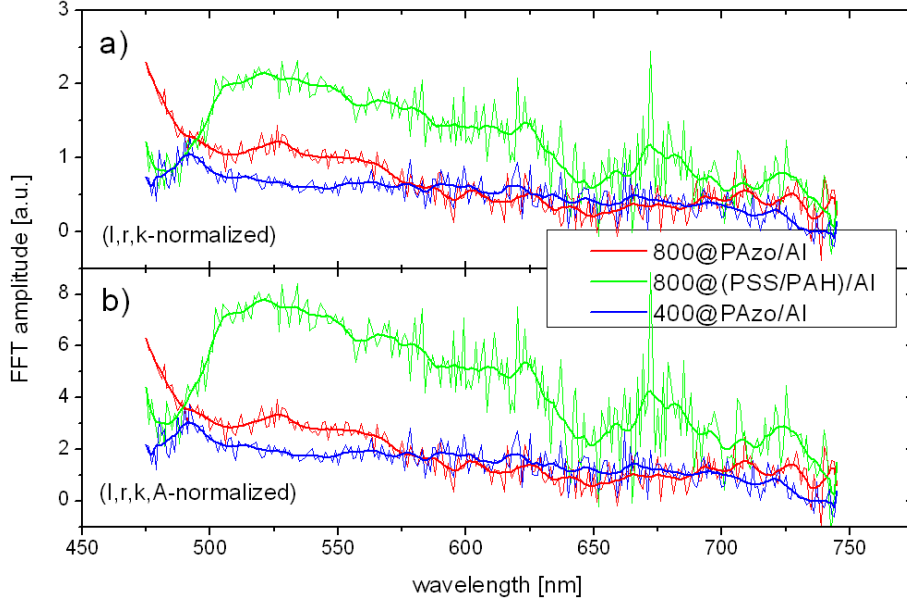
Figure 6.14: FFT amplitudes of TDBS oscillations induced by polyelectrolyte-covered aluminum transducers. The plot in (a) shows the phonon spectra, normalized to pump intensity, reflection coefficient, and k-vector. In panel (b) the FFT data additionally are normalized to the absorption, given in table 6.1. The excitation of the PAzo/PAH multilayers with 400 nm pump light (blue lines) generates less strain than using these layers as transparent anti-reflection coating (red lines).

of an aluminum layer covered with multilayers of PAzo/PAH. When pumped with $13.8\,\mathrm{mJ/cm^2}$ at 400 nm wavelength, only weak oscillations with an amplitude of $1 \cdot 10^{-4}$ occur in the spectral range of 500 nm to 620 nm wavelength. If the same sample is pumped with 800 nm wavelength, the PAzo/PAH multilayers do not absorb any light (see fig. 6.2). But they act as optical anti-reflection coating. The absorption increases from a value of $A_{Air/Al} = 0.16$ for an uncovered aluminum film to a value of $A_{(PAzo/PAH)/Al} = 0.37$, if PAzo/PAH multilayers are added (see tab. 6.1). The plot in figure 6.13a shows oscillations with an amplitude close to $0.5 \cdot 10^{-3}$, but the signals vanish for probe wavelengths above 580 nm.

The effect of signal enhancement due to anti-reflection coating is verified by another sample: Transparent multilayers of PSS/PAH cover an aluminum transducer layer that is excited with at 800 nm pump wavelength. Here, the absorption is $A_{(PAH/PSS)/Al} = 0.28$. The measured TDBS signal is shown in figure 6.13c. The amplitude of roughly $0.7 \cdot 10^{-3}$ is slightly higher than the amplitude caused by the PAzo/PAH covered Al transducer. It is best pronounced in the spectral range from 500 nm to 620 nm wavelength. The FFT amplitudes in figure 6.14 show that covering the aluminum transducer with transparent layers of PSS/PAH achieves the strongest TDBS signal. This is caused by a reduced reflection due to the refractive index matching of both materials that increases the absorption. In principle, both polyelectrolyte/Al samples should give the same response when excited with 800 nm pump wavelength, because the optical properties are similar and the sample structure is almost identical. But the FFT amplitudes of both samples differ by a factor

of 2 (see fig. 6.14a). The reason can be found by contemplating figures 6.13a and 6.13c once more. The oscillations of the (PAzo/PAH)/Al sample are more strongly damped than those of the (PSS/PAH)/Al sample. Whereas the oscillation amplitude of the (PAzo/PAH)/Al sample declines by a factor of 2, the amplitude of the (PSS/PAH)/Al sample shows almost no change over the observed time window. The calculation of the FFT amplitudes considers the temporal development. Therefore, strong damping results in a much weaker FFT signal. But this brings up the question to the origin of the two different damping constants. Since both samples base on identical fused silica substrates, a change of the optical properties must be the reason. On the other hand, the rotating sample holder ensured identical conditions with regards on degeneration for every point of the measurement.

The FFT spectra of the (PAzo/PAH)/Al sample pumped at 400 nm wavelength are shown in figure 6.14b. These FFT amplitudes are smaller than the FFT amplitudes for the same sample, excited with 800 nm pump wavelength, although the absorption coefficients at 400 nm and 800 nm pump wavelengths are almost identical for this sample (see table 6.1). The energy input is the same, but an excitation of the aluminum with 800 nm wavelength results in a roughly 1.5 times higher FFT amplitude in the spectral range of 500 nm to 550 nm than an excitation of the polyelectrolyte layer with 400 nm wavelength. At 475 nm probe wavelength, the values even differ by a factor of 3. These differences can be caused by several reasons. One is the excited spectrum of phonons. It depends on the structure and the material properties of the transducer. This will be discussed in detail in section 6.5. Another reason for the different TDBS signal is the impedance matching of the materials. The impedance values of fused silica and aluminum are $Z_{f.s.} = 13.1$ and $Z_{Al} = 17.3$. The applied PAzo/PAH and PSS/PAH polyelectrolyte multilayers both have a much lower value of $Z_{PE} = 3.4$ The transmitted and reflected intensities I_t and I_r of acoustic waves are defined as

$$I_t = \frac{1}{2} Z_2 v_t^2 = 4 I_{in} \frac{Z_1 Z_2}{(Z_1 + Z_2)^2} \tag{6.7a}$$

$$I_r = \frac{1}{2} Z_1 v_r^2 = I_{in} \frac{(Z_2 - Z_1)^2}{(Z_1 + Z_2)^2} \quad . \tag{6.7b}$$

The measured signal is proportional to the strain-induced change of the refractive index within the propagation material, which is equivalent to the acoustic amplitude [74]. The reflection coefficient is defined as $R = \sqrt{I_r/I_{in}}$. For a transition from aluminum to fused silica, the reflection coefficient is $R_{f.s./Al} = 0.14$. Both materials match quite well. At the (PAzo/PAH)/Al interface two-thirds ($R_{PE/Al} = 0.67$) of the hypersound intensity are reflected. The strain, initialized in the polyelectrolytes, has to pass both interfaces. Thus, only 28% of the initial acoustic amplitude can be detected in the propagation material. This factor would explain the much lower FFT signal of the (PAzo/PAH)/Al sample pumped with 400 nm wavelength compared to the same sample pumped with 800 nm wavelength, both shown in fig. 6.14. But this is only partly consistent with the measurement of PAzo/PAH on fused silica that gave a much stronger FFT amplitude (see fig. 6.12b). The interface of PAzo/PAH multilayers and fused silica has a acoustic reflection coefficient of $R_{PE/f.s.} = 0.59$. So 41% of the energy absorbed in the PAzo/PAH layer were transformed into TDBS
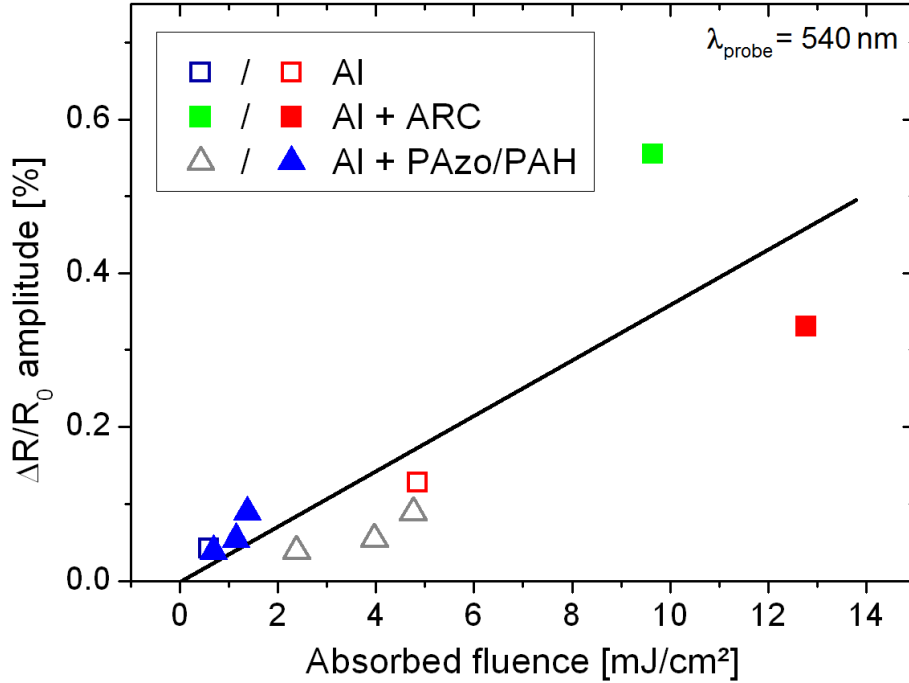
Figure 6.15: Measured amplitude of $\Delta R/R_0$ at $\lambda_{probe} = 540\,\text{nm}$ as function of absorbed fluence. Open squares mark uncovered Al transducer samples pumped at $400\,\text{nm}$ (blue) and $800\,\text{nm}$ (red) wavelength, respectively. Solid squares define Al samples covered with polyelectrolyte multilayers (green: PSS/PAH, red: PAzo/PAH). At $800\,\text{nm}$ pump wavelength, both polyelectrolytes are transparent, acting as anti-reflection coating (ARC). Triangles describe PAzo/PAH multilayers on Al pumped at $400\,\text{nm}$ wavelength. Assuming that absorption only occurs within the Al layer (solid blue triangles), the data points lie closer to the average (black line).

signal. Comparing figures 6.14b and 6.12b shows that both spectra differ in amplitude by roughly one order of magnitude[1]. The signal attenuation explained in section 6.3.1 contributes at most a factor of 5. Additionally, the slopes of both phonon spectra are different. Whereas the spectrum of PAzo/PAH multilayers on fused silica increases with increasing wavelength, the spectrum of (PAzo/PAH)/Al sample is more or less constant over the whole spectral range.

In contrast, the measurements of (PAzo/PAH)/Al and Al samples show similar spectral trends (see fig. 6.14b and 6.10b, but the amplitude is roughly 3 times higher for the Al sample without cover. This indicates similar structures of the transducer layers, but different efficiencies for the generation of strain. Both data match, if one assumes that the PAzo/PAH multilayers do not induce any strain into the aluminum inter layer. The total absorption is 34.5%, but most of the $400\,\text{nm}$ pump light is absorbed within the PAzo/PAH multilayers. The reflection coefficient of the (PAzo/PAH)/Al interface is 0.9, meaning the Al layer absorbs roughly 10% of the pump light. If the data shown in figures 6.14b are normalized to

---

[1] The plots use arbitrary units, but comparability is ensured by identical data proceeding.

(a)   (b)
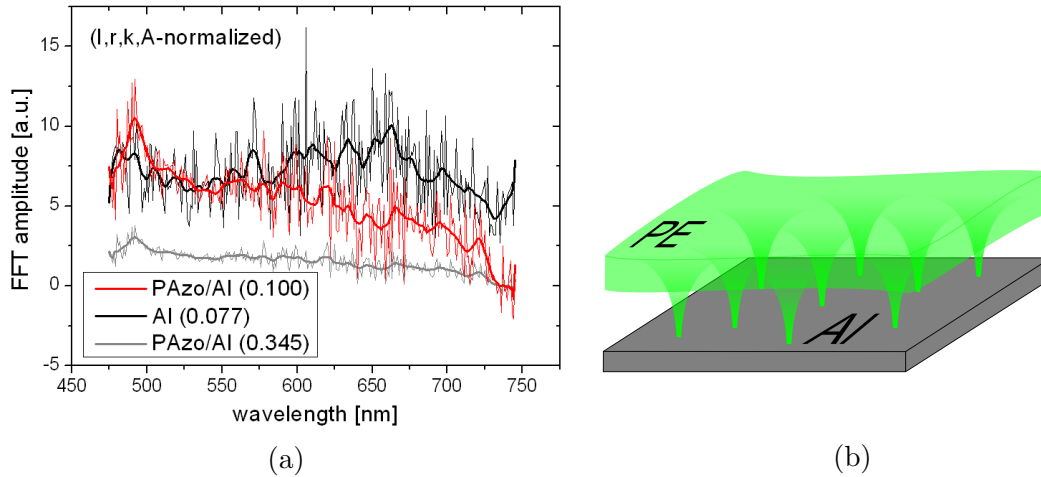
Figure 6.16: FFT amplitude plots of Al and (PAzo/PAH)/Al samples are shown in panel (a). Both samples were pumped with 400 nm wavelength. The data are normalized to the absorption values given in brackets. If the measured spectrum of the (PAzo/PAH)/Al sample is normalized to the absorption within the Al (red line) instead of the total absorption (grey line), it shows similar FFT amplitudes as the Al sample (black line) does. This indicates that the PAzo/PAH multilayers do not induce any strain into the substrate. The sketch in (b) shows a possible microscopic structure that prevents an efficient transfer of strain from PAzo/PAH to the aluminum layer.

the specific absorption of the Al instead of the total absorption value, it reproduces the FFT spectrum of the Al sample much better (see fig. 6.16a). This observation is verified by additional measurements applying different pump fluences. Figure 6.15 gives an overview of the aluminum transducer efficiencies at a probe wavelength of $\lambda_{probe} = 540$ nm. The (PAzo/PAH)/Al sample has lowest amplitudes of the $\Delta R/R_0$ oscillation signal, if the total absorption is taken into account. Assuming that only the light absorbed in the aluminum layer generates strain, the data fit better to the average value. The conclusion is that the detected acoustic wave is generated by the aluminum layer and the PAzo/PAH layers do not contribute any strain.

Repulsive forces between the hydrophilic polyelectrolytes and the hydrophobic aluminum were observed during the sample preparation. It is conceivable that the contact area of both layers is limited to few surface defects. This would provide the effect of an optical anti-reflection coating, but not the propagation of sound waves. The microscopic structure of such an interface is sketched in figure 6.16b.

In terms of strain generation, one can resume that the excitation of the PAzo/PAH multilayers on aluminum is less efficient than exciting the aluminum while the PAzo/PAH multilayers only act as optical anti-reflection coating.

6.4.3 Evidence of an Expansion of PAzo/PAH Multilayers

As shown in figure 6.1a, the inner structure of the PAzo sample consists of azo groups that are orientated perpendicular to the surface plane. If the excitation
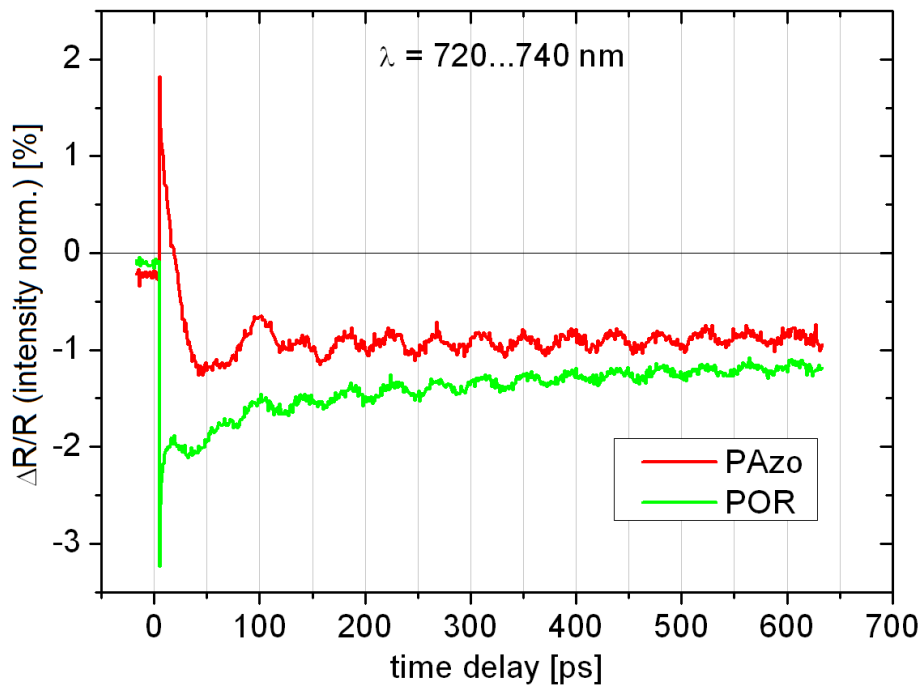
Figure 6.17: Relative change of reflection for PAzo and POR samples. The data are averaged over the spectral range from 720 nm to 740 nm and normalized to the pump fluence of $7.7\,\mathrm{mJ/cm^2}$. According to the change of the dielectric function, the response of $\Delta R/R_0$ is positive or negative. In case of PAzo, the decay of the initial change of reflection lasts 40 ps. This may be caused by the excitation of long-living *cis*-states. After dissipation of this feature, the TDBS signals of both samples oscillate in the same phase.

(a) partially damaged area 100x100 μm^2

(b) undamaged area 10x10 μm^2

(c) damaged area 10x10 μm^2
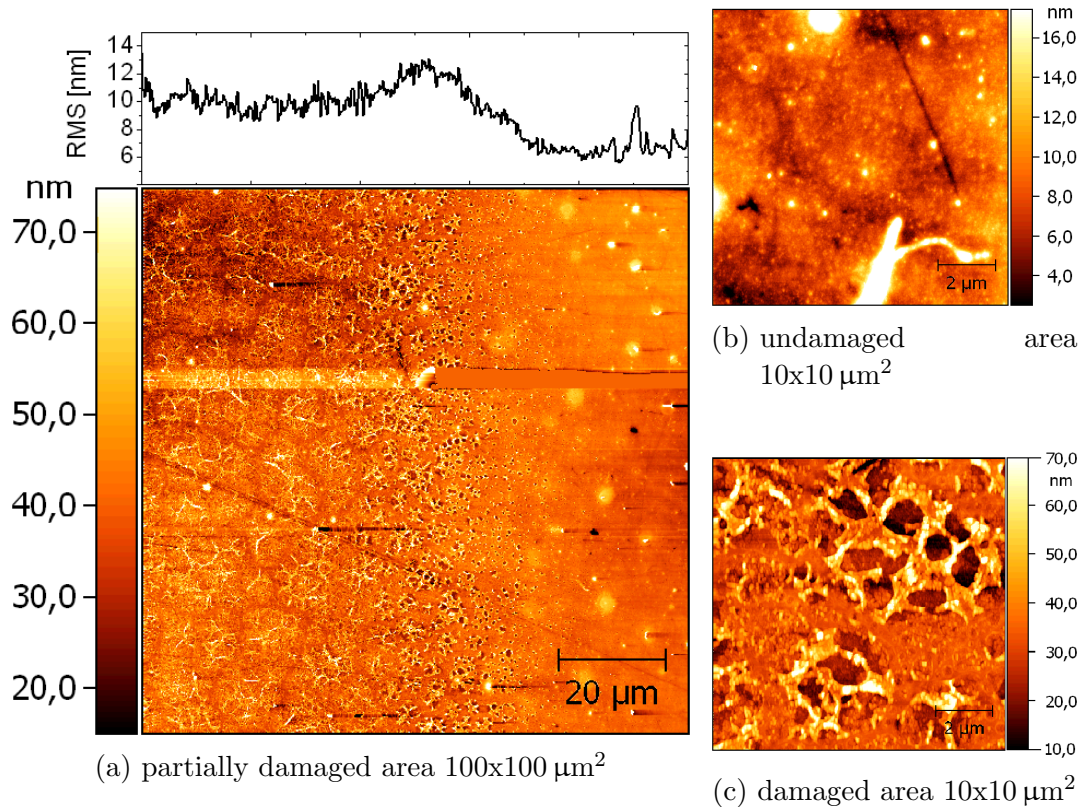
Figure 6.18: AFM topography measurements of a PAzo/PAH sample after TDBS experiments. Figure (a) shows the transition from laser excited area (left) to normal sample surface (right). The development of surface roughness is plotted above. Pictures (b) and (c) show damaged and undamaged areas with high resolution. Especially in the transition zone between excited and unexcited sample spots, the polyelectrolyte multilayers detach from the substrate yielding an increase of roughness.

causes the transition from the *trans* to the *cis* state, this isomerization would result in a reduction of the layer thickness. The induced strain and therefore the change of refractive index, both would be inverted yielding a phase shift of π in the oscillations of the DTBS signal. Since the excitation of porphyrin dye molecules results in heating that is attended by thermal expansion, the PAzo sample is compared to the POR sample.

The data shown in figures 6.11a and 6.11b suggest that there is no relative phase shift. For better visibility, the raw $\Delta R/R_0$ data of both samples are plotted in figure 6.17. Both TDBS signals clearly oscillate in the same phase. Since the refractive indices of the polyelectrolyte multilayers $n_{PAzo/PAH} \approx 1.65$ and $n_{PSS/PAH} \approx 1.55$ are both higher than the refractive index of fused silica $n_{fusedsilica} \approx 1.45$, a relative phase shift caused by static reflections can be excluded. So the measurements indicate that both materials expand. One has to assume, that the majority of the azo groups does not switch into *cis*-state. This may be caused by a lack of free volume within the multilayers, or by the covalent bonding to the polymer backbone.

(a) partially excited area 100x100 μm^2

(b) unexited area 10x10 μm^2

(c) exited area 10x10 μm^2
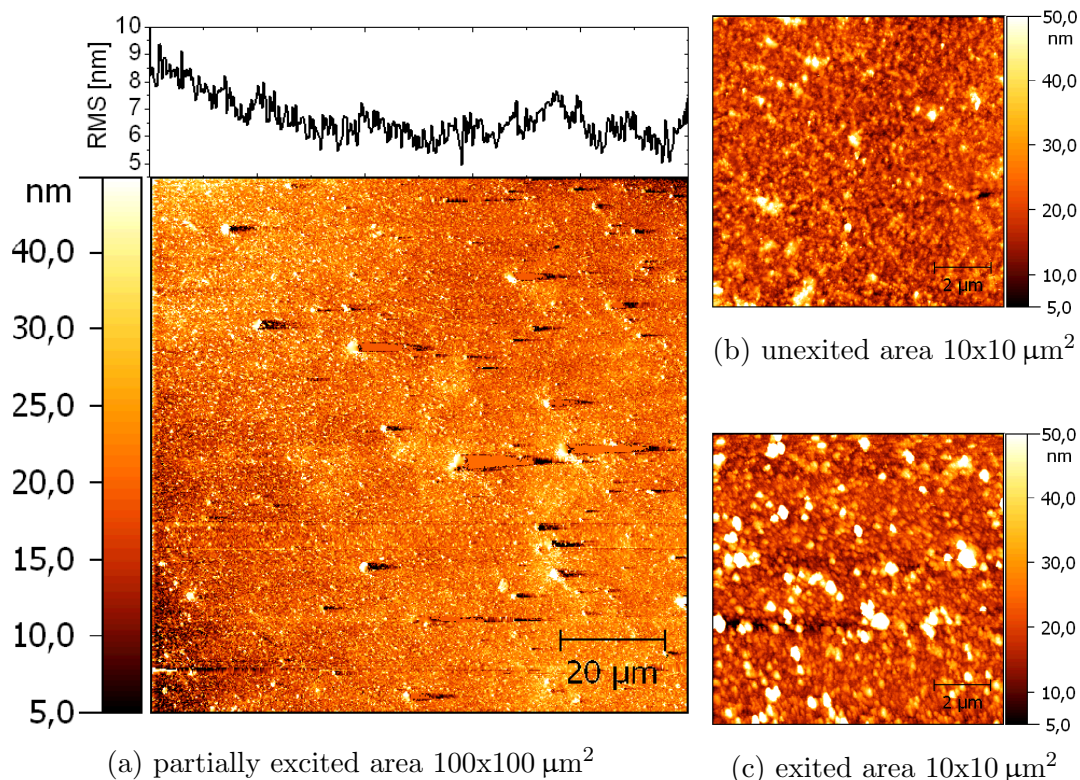
Figure 6.19: AFM topography measurements of a (PSS/PAH)+POR sample after TDBS experiments. Figure (a) shows the transition from laser excited area (left) to normal sample surface (right). The development of surface roughness is plotted above. Pictures (b) and (c) show both areas with high resolution. The laser excitation prohibits the attachment of dusk particles ('dots' in (a)). But it increases the surface roughness of the sample by the generation of aggregates (white spots in (c)).

6.4.4 Degeneration of Polyelectrolyte Transducers

Due to their strong absorption, multilayers of polyelectrolytes are applicable as transducers at low excitation energies. Pretests showed that intensities above $10\,\mathrm{mJ/cm^2}$ destroy PAzo/PAH multilayers within several minutes. At lower pump power, the sample endures measurement of few hours duration. However, even this results in visible surface modifications. These modifications are analyzed by AFM topography measurements. Since the sample is rotated during the measurements, the pump beam writes lines. Figure 6.18a shows center and border area of such a line. The laser excitation results in a reorganziation of the PAzo/PAH multilayers. In the high resolution picture (fig. 6.18c) holes and cracks are visible. The surface is very rough, giving an RMS value of 11 nm. Figure 6.18b shows an unpumped area. Here, the RMS value is only 2 nm. The RMS value does not trace the Gaussian beam profile of the pump pulse. So the damage is not proportional to the energy. Reorganization of the structure occurs, if a critical energy is reached. This energy may refer to the melting point of the polymers.

Measurements on the reference POR sample caused also permanent changes that were visible by eye. But the surface topography in figure 6.19a shows almost no differences between pumped and unpumped areas. Many particles with roughly $1\,\mu\mathrm{m}$ diameter are concentrated in the unpumped area, whereas only few can be found in the pumped one. The particles are probably dust particles that stick better to the untreated surface. Nevertheless, the roughness is slightly higher for laser pumped area. The reason is found in figure 6.19c. Many particles with a height of roughly 30 nm cover the surface and increase the RMS value to 7 nm. The particles may be polymer aggregates that were formed by thermal processes. A scan of the unpumped area does not show these particles (see fig. 6.19c). The surface is smoother with an RMS of 6 nm.

Comparing both samples, the POR sample seems to be more resistant to laser excitation than the PAzo/PAH sample. It is possible that the isomerization of the azo molecules is relevant for the reorganization of the PAzo/PAH multilayer films. If the excitation of PAzo/PAH layers generates the structures visible in figure 6.18c instantaneous, the inhomogeneous layer thickness would not release well-defined strain pulses and the TDBS signal would decreases.

6.5 Simulation of Lattice Dynamics

In the previous section, optical measured TDBS signals were used to calculate the spectra of the excited phonons. The phonon spectra measured by the Fourier-transferred signals are given by the dynamics within the sample that are induced by the pump laser. For most materials, the strain wave is more complex than the ideal bipolar strain wave as introduced in section 2.2. If transducer and propagation medium are not impedance matched, multipulses occur and the related phonon spectrum becomes more structured [45]. The shape of the strain wave also depends on the excitation profile that is given by the absorption characteristics of the transducer layer.

The dynamics within the layered system can be simulated. For this and other lattice-

Material	Density [kg/m³]	Sound velocity [nm/ps]	Impedance [10^6 Ns/m³]
Al	2700*	6.4*	17.3
PAzo/PAH	(1000)	3.1	3.1
PSS/PAH	(1000)	3.4	3.4
Fused silica	2200*	6.0	13.2

Table 6.2: Material properties of hypersound transducer and propagation materials. Density values in brackets are estimations that base on bulk polymers. Values, marked by (*) are taken from literature.

dynamics related applications, the udkm1Dsim toolbox was developed in the UDKM group [78]. It is based on a linear chain model of masses and springs. Each mass represents a unit cell that interacts with its neighbors via a spring. Both parameters, mass and spring constant, describe the materials. With known sample structure, the time-dependent distribution of strain and the related phonon spectrum can be calculated.

Impedance Matching   Excitation induces stress within the transducer layer. It expands and compresses the adjacent layers. How much of the strain amplitude is transferred from the transducer layer to the adjacent medium depends on both materials. The reflection coefficient for acoustic waves at an interface is defined as

$$r = \frac{Z_2 - Z_1}{Z_2 + Z_1}. \tag{6.8}$$

The impedance Z is determined by the product of density and sound velocity $Z = \rho v_S$. If the adjacent material has a lower impedance, the reflection coefficient is negative and a phase shift occurs. Thus, expansion turns into compression and vice versa.

Excitation Profile   The law of Beer–Lambert predicts an exponential decline of the pump laser intensity, yielding a inhomogeneous excitation profile within many transducer materials such as SRO, LSMO and other perovskites [79, 80]. However, in elemental metals, the coupling time of hot electrons to the lattice is the order of 2 ps [81]. Within this time, the electrons diffuse about several hundreds nanometers [82]. Thus, the absorption profile is exponential, but the resulting heat distribution is homogeneous.

In polyelectrolytes, a nearly homogeneous excitation is caused by bleaching. The observed values of absorption at 400 nm were about 2.5 times lower in the pump-probe setup than expected from UV-VIS spectroscopic measurements (compare tab. 6.1 and fig. 6.2). Even very thick samples of one micron PAzo/PAH multilayers transmit parts of the 400 nm pump laser. In saturation case, every molecule is excited. This results in an almost homogeneous excitation profile.

Generation of a Strain Wave   In the ideal case, transducer and propagation material are perfectly impedance matched. Thus, excitation of the transducer would result in a single, bipolar strain pulse that consists of a compressive part, followed

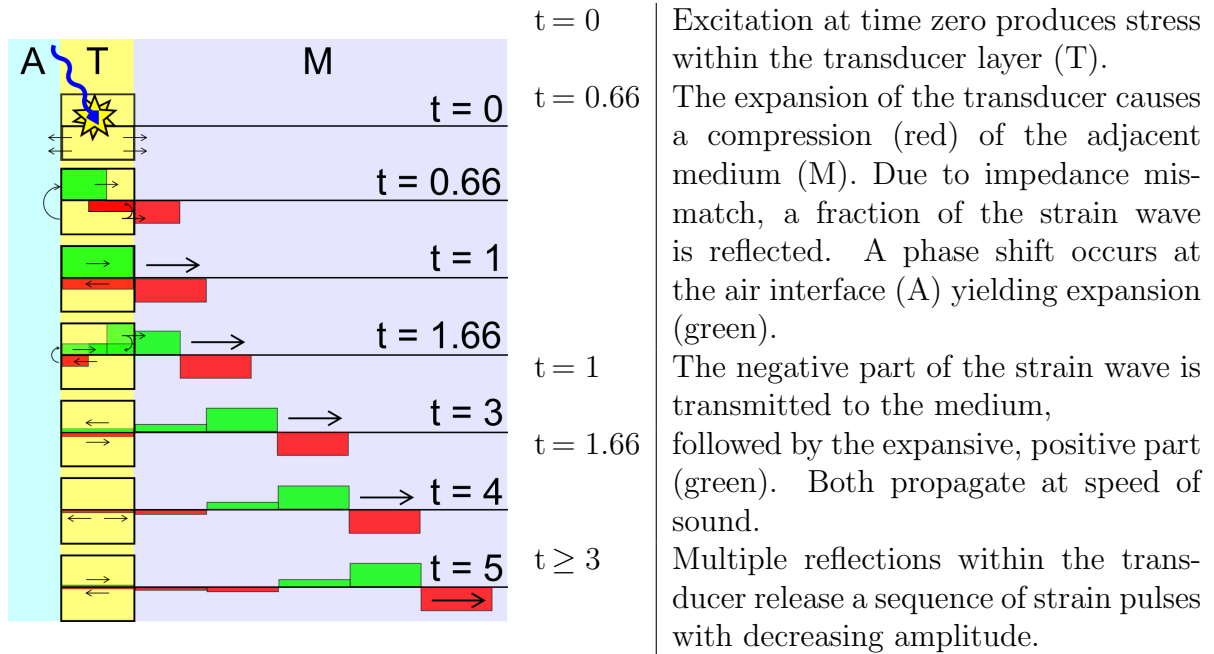|	
t = 0	Excitation at time zero produces stress within the transducer layer (T).
t = 0.66	The expansion of the transducer causes a compression (red) of the adjacent medium (M). Due to impedance mismatch, a fraction of the strain wave is reflected. A phase shift occurs at the air interface (A) yielding expansion (green).
t = 1	The negative part of the strain wave is transmitted to the medium,
t = 1.66	followed by the expansive, positive part (green). Both propagate at speed of sound.
t ≥ 3	Multiple reflections within the transducer release a sequence of strain pulses with decreasing amplitude.

Figure 6.20: Generation of multiple strain pulses. The time is normalized to the duration, a sound pulse needs to cross the transducer layer.

by an expansive part. But most samples have a mismatch between transducer and propagation medium (see tab. 6.2). This causes multiple reflections of the strain wave between both transducer interfaces. At the air interface, virtually all strain is reflected, undergoing a phase shift. At the substrate interface, a fraction of the strain is transmitted into the fused silica at each cycle (see equ. 6.7a). The other part is reflected according to equation 6.8.

The temporal development of the strain wave is sketched in figure 6.20b. In the beginning, the compression part ($\epsilon < 0$) enters the substrate. It is followed by an expansion ($\epsilon > 0$) that consists of two parts. Part one is the former compression, reflected and phase shifted at the air interface. The second, weaker part is the initial compression after one full cycle within the transducer layer.

6.5.1 Example: PAzo/PAH sample

The PAzo sample, discussed in section 6.4 shall be taken as example. Its structure is schematically shown in figure 6.21a. The transducer layer of PAzo/PAH is covered by a thin layer of PSS/PAH. This cover acts as spacer to the air interface. Thus, the excited strain profile is interrupted by sections with $\epsilon = 0$. This can be seen in figure 6.21b for a delay time of 50 ps. At 150 ps delay time, the simulation shows the same temporal development as sketched in figure 6.20. However, the simulation considers damping of the phonons. Since the damping is proportional to the k-vector, high order structures vanish and the strain profile becomes smoother over time. The part with $\epsilon = 0$ disappears within 150 ps.

Figure 6.21c shows the associated phonon spectrum that is represented by the FFT of the simulated strain profile. It consists of a double peak that declines strongly
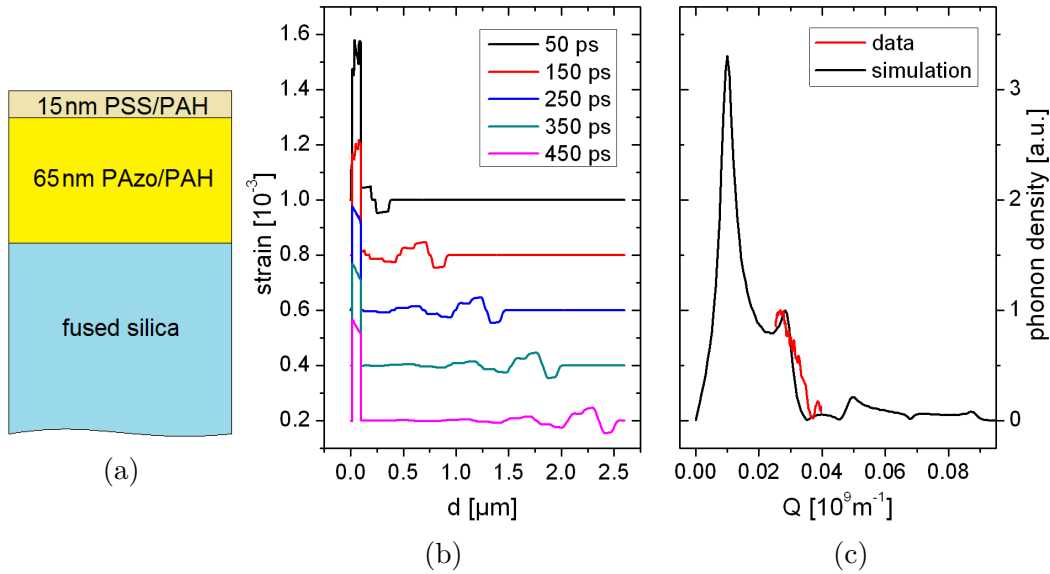
Figure 6.21: The simulation treats a PSS/PAH-capped PAzo/PAH transducer on a fused silica substrate (a). After excitation, strain waves propagate into the substrate (b). The stimulated phonon spectrum as shown in c). The measured data (red) are reproduced by the second maximum. The damping of phonons with high k-vector is higher than for phonons with low k-vector. Thus, discrete features of the strain profile vanish (e.g. the $\epsilon = 0$ step between compressive and expansive part).

at $Q \approx 0.03 \cdot 10^9 \mathrm{m}^{-1}$. This decrease occurs in the part of the spectrum which is accessible by TDBS with visible light. The measured PAzo data, shown in figure 6.12, are normalized to the value of the side peak and translated to Q-scale. The overlap of data and simulation confirms the applied values in table 6.2 as well as the assumed sample structure.

7 Summary

7.1 Gold Nanoparticles

Characterization of Gold Nanorods   Gold nanorods with three different aspect ratios were characterized by SEM and AFM. The particles were deposited on polyelectrolyte multilayers of PAH/PSS. Optical measurements showed two localized surface plasmon resonance (LSPR) peaks, related to the longitudinal and transverse plasmons, respectively. The longitudinal LSPR shifts strongly to the red, if the particles are fully embedded into polyelectrolytes. The transverse LSPR shift is much weaker. Both shifts can be qualitatively explained with the Maxwell-Garnett effective medium theory using the particles' dielectric function taken from the literature, the dielectric function of the surrounding measured by ellipsometry, and the shape factor u of the particle. The shape factor depends on the aspect ratio of the particles measured by SEM and is different for each particle axis. Quantitatively agreement can be achieved only by adjusting the dielectric function of gold nanoparticles. It was determined experimentally in the observed spectral range within the Maxwell-Garnett approximation and compared to the dielectric function of bulk gold. The dielectric function of particles shows a shift to higher values compared to bulk gold as expected from the lower electron density of the nanoparticles near their surface.

Determining the Range of Interaction   The stepwise covering of GNRs with monolayers of polyelectrolytes enabled recording the absorption characteristics as a function of the cover layer thickness. All observed curves showed saturation behavior depending on the particle sizes. The values of saturation mark the range of interaction. Small GNRs saturate at lower cover thickness than bigger ones. However, each particle has at least two values of saturation. The shift of the transverse LSPR peak saturates roughly at the same cover thickness as the increase of absorption does. The peak shift of the longitudinal LSPR saturates at a value that is close to the half of the particles length.

Modeling a Gold Nanoparticle in an Inhomogeneous Environment   The environment of an uncovered or partially embedded particle consists of two phases: polymer and air. To calculate the LSPR analytically, the effect of both media was modeled by one effective average dielectric function. To this end, each volume fraction was weighted by the electric field intensity of the light induced dipole and multiplied with the dielectric function of the respective medium. The best agreement is achieved when the GNRs were reduced to spherical calottes which is also suggested by the SEM images. The environment of the cylindrical middle part could be neglected, since the dipole field concentrates at the particle's ends. With the values of the

SEM and AFM characterization measurements, and the calculated dielectric functions, the model reproduces the measured LSPR with excellent agreement.

7.2 Picosecond Acoustics

Time-Domain Brillouin Scattering Experiments   Pump-probe experiments measure the interaction of light with phonons (Brillouin scattering). Phonon wave packets were generated by ultrafast laser excitation of different transducer materials. The propagation of these phonon waves within the medium (fused silica) generates oscillations of the white light probe pulse in the gigahertz range, caused by interference of light, reflected at the hypersound wave and at the sample's interfaces.

Comparing Aluminum and Polyelectrolytes as Transducer Materials   A vapor deposited aluminum film was compared to layer-by-layer deposited polyelectrolyte multilayers. Both materials were applicable as transducers and showed clear time-domain Brillouin scattering (TDBS) oscillations. The measured signals of the polyelectrolyte transducers (PAzo/PAH) and (PSS/PAH)*POR) were even stronger than the signal of the Al sample. This was caused by signal attenuation due to destructive interference that especially occurred for high reflecting materials such as Al. However, the organic polyelectrolyte films had a lower damage threshold than aluminum layers. Samples, containing the polyelectrolyte PAzo tended to reorganize due to laser excitation which necessitated a continuous change of the probed spot during the measurements. Multilayers of PSS/PAH doped with porphyrin dye (POR) were more stable. The speculation that PAzo/PAH multilayers shrink in thickness due to *trans-cis* isomerization, could be disproved by comparing the TDBS signal of PAzo/PAH and (PSS/PAH)*POR samples. Both signals showed similar TDBS oscillations. The absence of a relative phase shift confirms that both polyelectrolyte transducer materials expand due to laser excitation. Furthermore, the slightly weaker TBBS oscillation amplitudes of the PAzo/PAH sample compared to the POR sample demonstrate that the azo groups do not contribute to the induced strain via mechanical isomerization processes.
One can summarize that polyelectrolyte multilayers as well as aluminum can be used as transducer materials for picosecond acoustics. The advantages of the polyelectrolytes are the fast and easy attachment to hydrophilic surfaces, and their transparency for most of the visible light. But the pump fluence is limited to roughly $10 \, \text{mJ/cm}^2$, to avoid a fast degeneration of these layers.

Quantification of the Induced Strain   It was not possible to determine a reliable value for the strain amplitudes within the fused silica substrates, induced by aluminum or polyelectrolyte transducer layers. The measured TDBS signals depend on the strain amplitude, but also on the optical properties that were not uniform for these samples. To reduce the parameters, new samples were introduced. The samples consist of different transducer materials, but the optical properties are identical when probed from substrate side. This was provided by an highly reflecting interlayer of aluminum. Unfortunately, the quantitative comparison of the strains

induced by PAzo/PAH mulitlayers and Al film gave results, that were not consistent with the results of the investigation of PAzo/PAH multilayers on fused silica substrate. The insufficient attachment of the polyelectrolyte transducer at the Al interface was identified as reason for the inhibited transfer of strain. However, the polyelectrolyte layers acted as optical anti-reflection coating and increased the efficiency of the Al transducer.

7.3 Future Prospects

Field Enhancement Due to GNRs The properties of gold nanorods are well-understood. The choice of the surfactant adjusts the surface charge, so that other charged molecules or particles can attach to the particles' surface. The strong field enhancement in the GNR's environment will be used for SNOM measurements on single particles (e.g. quantum dots).

GNRs for Sensing Application If the dielectric function of the surrounding medium changes, the LSPR of the embedded GNRs shifts. GNRs bonded to a polyelectrolyte surface can be used as detector to determine the dielectric function of an adjacent medium, especially liquids and gases.
Another application is the detection of strain. The compression of a medium increases its density and therefore the dielectric function changes. This effect will be exploited to quantify the strain, induced by picosecond acoustic transducer layers.

Optimized Samples for Picosecond Acoustics Experiments The quantification of transducer-induced strain can be carried out by time-domain Brillouin scattering experiments. On the one hand, the optical barrier layer of aluminum can be modified (e.g. by plasma cleaning) to improve the acoustic coupling between the polyelectrolyte transducer layer and the aluminum. On the other hand, the optical barrier can be made of another probe light absorbing material (e.g. dye-labeled polyelectrolytes).

Bibliography

[1] K. Eric Drexler. *Engines of Creation: The Coming Era of Nanotechnology.* Anchor Books, New York, 1986.

[2] S. Eustis and M. A. El-Sayed. Why Gold Nanoparticles are more Precious Than Pretty Gold: Noble Metal Surface Plasmon Resonance and its Enhancement of the Radiative and Nonradiative Properties of Nanocrystals of Different Shapes. *Chemical Society Reviews*, 35:209, 2006.

[3] M. Spiro and D. de Jesus. Nanoparticle catalysis in microemulsions: Oxidation of N,N-dimethyl-p-phenylenediamine by cobalt(III) pentaammine chloride catalyzed by colloidal palladium in water/AOT/n-heptane microemulsions. *Langmuir*, 16:2464, 2000.

[4] Y. Li, J. Petroski, and M. A. El-Sayed. Activation energy of the reaction between hexacyanoferrate(III) and thiosulfate ions catalyzed by platinum nanoparticles. *Journal of Physical Chemistry B*, 104(47):10956, 2000.

[5] W. E. Doering and S. M. Nie. Single-molecule and single-nanoparticle SERS: Examining the roles of surface active sites and chemical enhancement. *Journal of Physical Chemistry B*, 106(2):311, 2002.

[6] Q. Cui, B. Xia, S. Mitzscherling, A. Masic, L. Li, M. Bargheer, and H. Möhwald. Preparation of gold nanostars and their study in selective catalytic reactions. *Colloids and Surfaces A - Physicochemical and Engeneering Aspects*, 465:20, 2015.

[7] G. Piaciotti, D. Weinreich, D. Goia, N. Pavel, R. McLaughlin, and L. Tamarkin. Colloidal gold: A novel nanoparticle vector for tumor directed drug delivery. *Drug Delivery*, 11:169, 2004.

[8] Y. Shiao, H. Chiu, P. Wu, and Y. Huang. Aptamer-Functionalized Gold Nanoparticles As Photoresponsive Nanoplatform for Co-Drug Delivery. *Applied Materials and Interfaces*, 6:21832, 2014.

[9] Y. Cheng, Q. Dai, R. Morshed, X. Fan, M. L. Wegscheid, D. A. Wainwright, Y. Han, L. Zhang, B. Auffinger, A. L. Tobias, E. Rincon, B. Thaci, A. U. Ahmed, P. C. Warnke, C. He, and M. S. Lesniak. Blood-Brain Barrier Permeable Gold Nanoparticles: An Efficient Delivery Platform for Enhanced Malignant Glioma Therapy and Imaging. *Small*, 10:5137, 2014.

Bibliography

[10] R. Kazmierczak, E. Choe, J. Sinclair, and A. Eisenstark. Direct attachment of nanoparticle cargo to salmonella typhimurium membranes designed for combination bacteriotherapy against tumors. *Methods in Molecular Biology*, 1225:151, 2015.

[11] N. P. Truong, M. R. Whittaker, C. W. Mak, and T. P. Davis. The importance of nanoparticle shape in cancer drug delivery. *Expert Opinion on Drug Delivery*, 12:129, 2015.

[12] XJ Feng, L Feng, MH Jin, J Zhai, L Jiang, and DB Zhu. Reversible super-hydrophobicity to super-hydrophilicity transition of aligned ZnO nanorod films. *Journal of the American Chemical Society*, 126(1):62, 2004.

[13] P. Roach, N. J. Shirtcliffe, and M. I. Newton. Progess in superhydrophobic surface development. *Soft Matter*, 4(2):224, 2008.

[14] K. Koch, B. Bhushan, Y. C. Jung, and W. Barthlott. Fabrication of artificial Lotus leaves and significance of hierarchical structure for superhydrophobicity and low adhesion. *Soft Matter*, 5(7):1386, 2009.

[15] G. Decher, J. D. Hong, and J. Schmitt. Buildup of ultrathin multilayer films by a self-assembly process: III. Consecutively alternating adsorption of anionic and cationic polyelectrolytes on charged surfaces. *Thin Solid Films*, 210(2):831, 1992.

[16] P. Ducheyne and Q. Qiu. Bioactive ceramics: the effect of surface reactivity on bone formation and bone cell function. *Biomaterials*, 20(23-24):2287, 1999.

[17] A. Stein, B. J. Melde, and R. C. Schroden. Hybrid inorganic-organic mesoporous silicates - Nanoscopic reactors coming of age. *Advanced Materials*, 12(19):1403, 2000.

[18] X. Liu, P. Chu, and C. Ding. Surface modification of titanium, titanium alloys, and related materials for biomedical applications. *Material Science & Engeneering R-Reports*, 47(3-4):49, 2004.

[19] A. K. Gupta and M. Gupta. Synthesis and surface engineering of iron oxide nanoparticles for biomedical applications. *Biomaterials*, 26(18):3995, 2005.

[20] Gero Decher. Fuzzy Nanoassemblies: Toward Layered Polymeric Multicomposites. *Science*, 277:1232, 1997.

[21] M. Kiel, S. Mitzscherling, W. Leitenberger, S. Santer, B. Tiersch, T. K. Sievers, H. Möhwald, and M. Bargheer. Structural Characterization of a Spin-Assisted Colloid-Polyelectrolyte Assembly: Stratified Multilayer Thin Films. *Langmuir*, 26(23):18499, 2010.

[22] M. Kiel, M. Klötzer, S. Mitzscherling, and M. Bargheer. Measuring the Range of Plasmonic Interaction. *Langmuir*, 28(10):4800, 2012.

[23] G. S. Hartley. The Cis-form of Azobenzene. *Nature*, 140:281, 1937.

[24] T. Ikeda and O. Tsutsumi. Optical Switching and Image Storage by Means of Azobenzene Liquid-Crystal Films. *Science*, 268(5219):1873, 1995.

[25] T. Ikeda, M. Nakano, Y. Yu, O. Tsutsumi, and A. Kanazawa. Anisotropic bending and unbending behavior of azobenzene liquid-crystalline gels by light exposure. *Advanced Materials*, 15:201, 2003.

[26] K. G. Yager and C. J. Barrett. Novel photo-switching using azobenzene functional materials. *Journal of Photochemistry and Photobiology A*, 182:250, 2006.

[27] A. Archut, F. Vögtle, L. de Cola, G. C. Azzellini, V.i Balzani, P. S. Ramanujam, and R. H. Berg. Azobenzene-functionalized cascade molecules: Photoswitchable supramolecular systems. *Chemistry*, 4:699, 1998.

[28] A. S. Matharu, S. Jeeva, and P. S. Ramanujam. Liquid crystals for holographic optical data storage. *Chemical Society Reviews*, 36:1868, 2007.

[29] N. K. Viswanatha, D. Y. Kim, S. Bian, J. Williams, W. Liu, L. Li, L. Samuelson, J. Kumar, and S. K. Tripathy. Surface relief structures on azo polymer films. *Journal of Materials Chemistry*, 9:1941, 1999.

[30] S. Xie, A. Natansohn, and P. Rochon. Recent developments in aromatic azo polymers research. *Chemistry of Materials*, 5:403, 1993.

[31] Y. Yu, M. Nakano, and T. Ikeda. Photomechanics: Directed bending of a polymer film by light. *Nature Brief Communications*, 425:145, 2003.

[32] T. Nägele, R. Hoche, W. Zinth, and J. Wachtveitl. Femtosecond photoisomerization of cis-azobenzene. *Chemical Physics Letters*, 272(5-6):489, 1997.

[33] Z. V. Vardeny. ULTRAFAST ELECTRONIC AND ACOUSTIC EFFECTS IN CONDUCTING POLYMERS. *Journal of the Electrochemical Society*, 135:109, 1988.

[34] G. S. Kanner, Z. V. Vardeny, and B. C. Hess. Picosecond acoustics in polythiophene thin films. *Physical Review B*, 42:5403, 1990.

[35] Y.-C. Lee, K. C. Bretz, F. W. Wise, and W. Sachse. Picosecond acoustic measurements of longitudinal wave velocity of submicron polymer films . *Aplied Physics Letters*, 69:1692, 1996.

[36] P. Winsemius, M. Guerrisi, and R. Rosei. Splitting of the interband absorption edge in Au: Teperature dependence. *Physical Review B*, 12(10):4570, 1975.

[37] P. B. Johnson and R. W. Christy. Optical Constants of the Noble Metals. *Physical Review B*, 6(12):4370, 1972.

[38] John David Jackson. *Klassische Elekrodynamik 3. Auflage*. De Gruyter, 1999.

[39] U. Kreibig, A. Althoff, and H. Pressmann. Veiling of optical single particle properties in many particle systems by effective medium and clustering effects. *Surface Science*, 106:308, 1981.

Bibliography

[40] G. A. Niklasson, C. G. Granqvist, and O. Hunderi. Effective medium models for the optical properties of inhomogeneous materials. *Applied Optics*, 20:26, 1981.

[41] Yu-Ying, Ser-Sing Chang, Chien-Liang Lee, and C. R. Chris Wang. Gold Nanorods: Electrochemical Synthesis and Optical Properties. *Journal of Physical Chemistry*, 101(34):661, 1997.

[42] M. B. Mohamed, K. Z. Ismail, S. Link, and M. A. El-Sayed. Thermal Reshaping of Gold Nanorods in Micelles. *Journal of Physical Chemistry B*, 102(47):9370, 1998.

[43] S. Link, M.B. Mohamed, and M.A. El-Sayed. Simulation of the Opctical Absorption Spectra of Gold Nanorods as a Function of Theur Aspect Ratio and the Effect of the Medium Dielectric Constant. *J. Phys. Chem.*, 103(16):3073, 1999.

[44] H.J. Eichler, M.Freyberger, H. Fuchs, F. Haug, H. Kaase, J-Kross, H. Langa, H. Lichte, H. Niedrig, T. Pfau, H. Rauch, W. P. Schleich, G. Schmahl, E. Sedlmayr, F. Serick, K. Vogel, H. Weber, and K. Weber. *Lehrbuch der Experimentalphysik Band 3: Optik*. Walter de Gruyter, 2004.

[45] A. Bojahr, M. Herzog, S. Mitzscherling, L. Maerten, D. Schick, J. Goldshteyn, W. Leitenberger, R. Shayduk, P. Gaal, and M. Bargheer. Brillouin scattering of visible and hard X-ray photons from optically synthesized phonon wavepackets. *Optics Express*, 21:21188, 2013.

[46] Maxwell and Garnett. Colours in Metal Glasses and Metal Films. *Transactions of the Royal Society*, CCIII:385, 1904.

[47] Ernst A. Hauser and J. Edward Lynn. *Experiments in colloid chemistry*. McGraw-Hill book Co., 1940.

[48] G. Frens. Controlled Nucleation for the Regulation of the Particle Size in Monodisperse Gold Suspension. *Nature*, 241(1):20, 1973.

[49] K. C. Grabar, , R. G. Freeman, , M. B. Hommer, and M. J. Natan. Preparation and Characterization of Au Colloid Monolayers. *Analytical Chemistry*, 67(4):735, 1995.

[50] J. Turkevich, P.C. Stevenson, and J. Hillier. The formation of colloidal gold. *Journal of physical chemistry*, 57(7):670, 1953.

[51] M. Morga and Z. Adamczyk. Monolayers of cationic polyelectrolytes on mica - Electrokinetic studies. *Joirnal of Colloid ant Interface Science*, 407:196, 2013.

[52] T. K. Sau and C. J. Murphy. Room temperature, high-yield synthesis of multiple shapes of gold nanoparticles in aqueous solution. *Journal of the American Chemical Society*, 126(28):8648, 2004.

[53] R. K. Iler. Multilayers of colloidal particles. *Journal of Colloid and Interface Science*, 21(6):569, 1966.

[54] J. H. Fendler. Self-assembled nanostructured materials. *Chemistry of Materials*, 8:1616, 1996.

[55] J. B. Schlenoff and S. T. Dubas. Mechanism of Polyelectrolyte Multilayer Growth: Charge Overcompensation and Distribution. *Langmuir*, 34(3):592, 2001.

[56] J. B. Schlenoff, A. H. Rmaile, and C. B. Bucur. Hydration Contributions to Association in Polyelectrolyte Multilayers and Complexes: Visualizing Hydrophobicity. *Journal of the Amercian Chemical Society*, 130(41):13589, 2008.

[57] Yuri Lvov, Gero Decher, and Helmuth Mohwald. Assembly, Structural Characterization, and Thermal Behavior of Layer-by-Layer Deposited Ultrathin Films of Poly(vinylsulfate) and Poly(allylamine). *Langmuir*, 9:481, 1993.

[58] C. J. Lefaux, J. A. Zimberlin, A. v. Dobrynin, and P. T. Mather. Polyelectrolyte Spin Assembly: Influence of Ionic Strength on the Growth of Multilayered Thin Films. *Journal of Polymer Science*, 42:3654, 2004.

[59] S. Mitzscherling. Herstellung und Charakterisierung von Nanoschichtsystemen aus Polyelektrolyten und Goldpartikeln. *Diploma Thesis*, 2010.

[60] K. M. Lenahan, Y.-X. Wang, Y. Liu, R. O. Claus, J. R. Heflin, D. Marciu, and C. Figura. Novel Polymer Dyes for Nonlinear Optical Applications Using Ionic Self-Assembled Monolayer Technology. *Advanced Materials*, 10(11):853, 1998.

[61] S. R. Puniredd, D. Janczewski, D. P. Go, X. Zhu, S. Guo, S. L. M. Teo, S. S. C. Lee, and G. J. Vansco. Imprinting of metal receptors into multilayer polyelectrolyte films: fabrication and applications in marine antifouling. *Chemical Science*, 6:372, 2015.

[62] A. Schneider, G. Francius, R. Obeid, P. Schwinte, J. Hemmerle, B. Frisch, P. Schaaf, J.-C. Voegle, B. Senger, and C. Picart. Polyelectrolyte Multilayers with a Tunable Young's Modulus: Influence of Film Stiffness on Cell Adhesion. *Langmuir*, 22:1193, 2006.

[63] N. J. Shak, J. Hong, M. N. Hyder, and P. T. Hammond. Osteophilic Multilayer Coatings for Accelerated Bone Tissue Growth. *Advanced Materials*, 24:1445, 2012.

[64] Z. Tang, Y. Wang, P. Podsiadlo, and N. A. Kotov. Biomedical Applications of Layer-by-Layer Assembly: From Biomimetics to Tissue Engineering. *Advanced Materials*, 18:3203, 2006.

[65] K. Ariga, J. P. Hill, and Q. Ji. Layer-by-layer assembly as a versatile bottom-up nanofabrication technique for exploratory research and realistic application. *Physical Chemistry Chemical Physics*, 9:2319, 2007.

[66] J. Hiller, J. D. Mendelsohn, and M. F. Rubner. Reversibly erasable nanoporous anti-reflection coatings from polyelectrolyte multilayers. *Nature Materials*, 1:59, 2002.

[67] L. Zhai, A. J. Nolte, R. E. Cohen, and M. F. Rubner. pH-Gated Porosity Transitions of Polyelectrolyte Multilayers in Confined Geometries and Their Application as Tunable Bragg Reflectors. *Macromolecules*, 37:6113, 2004.

[68] P. T. Hammond. Form and Function in Multilayer Assembly: New Applications at the Nanoscale. *Advanced Materials*, 16:1271, 2004.

[69] J. B. Schlenoff. Retrospective on the Future of Polyelectrolyte Multilayers. *Langmuir*, 25(24):14007, 2009.

[70] K. J. Seu, A. P. Pandey, F. Haque, E. A. Proctor, A. E. Ribbe, and J. S. Hovis. Effect of Surface Treatment on Diffusion and Domain Formation in Supported Lipid Bilayers. *Biophysical Journal Volume*, 92(7):2445, 2007.

[71] A. Brodeur and S. L. Chin. Ultrafast white-light continuum generation and self-focusing in transparent condensed media. *Journal of the Optical Society of America B*, 16(4):637, 1999.

[72] P. K. Jain and M. A. El-Sayed. Surface Plasmon Coupling and Its Universal Size Scaling in Metal Nanostructures of Complex Geometry: Elongated Particle Pairs and Nanosphere Trimers. *Journal of Physical Chemistry C*, 112(13):4954, 2008.

[73] A. v. Reppert. Ultrafast dynamics of azobenzene in polyelectrolyte thin films. *Bachelor thesis*, 2012.

[74] S. Ayrinhac, M. Foret, A. Devos, B. Rufflé, E. Courtens, and R. Vacher. Subterahertz hypersound attenuation in silica glass studied via picosecond acoustics. *Physical Review B*, 83(1):14204, 2011.

[75] A. Bojahr, D. Schick, L. Maerten, M. Herzog, I. Vreyoiu, C. v. Korff-Schmising, C. J. Milne, S. L. Johnson, and M. Bargheer. Comparing the oscillation phase in optical pump-probe spectra to ultrafast x-ray diffraction in the metal-dielectric SrRuO3/SrTiO3 superlattice. *Physical Review B*, 85:224302, 2012.

[76] D. Schick, M. Herzog, H. Wen, P. Chen, C. Adamo, P. Gaal, D. G. Schlom, P. G. Evans, Y. Li, and M. Bargheer. Localized Excited Charge Carriers Generate Ultrafast Inhomogeneous Strain in the Multiferroic BiFeO3. *Physical Review Letters*, 112:97602, 2014.

[77] David R. Lide. *CRC Handbook of Chemistry and Physics: 71st Ed 1990-1991*. CRC Press, 1990.

[78] D. Schick, A. Bojahr, M. Herzog, R. Shayduk, C. von Korff-Schmising, and M. Bargheer. udkm1Dsim - A simulation toolkit for 1D ultrafast dynamics in condensed matter. *Computer Physics Communications*, 185(2):651, 2013.

[79] M. Herzog, D. Schick, P. Gaal, R. Shayduk, C. v. Korff-Schmising, and M. Bargheer. Analysis of ultrafast X-ray diffraction data in a linear-chain model of the lattice dynamics. *Applied Physics A*, 106:489, 2011.

[80] D. Schick, A. Bojahr, M. Herzog, P. Gaal, I. Vrejoiu, and M. Bargheer. Following Strain-Induced Mosaicity Changes of Ferroelectric Thin Films by Ultrafast Reciprocal Space Mapping. *Physical Review Letters*, 9:95502, 2013.

[81] S. Nie, X. Wang, H. Park, R. Clinite, and J. Cao. Measurement of the Electronic Grüneisen Constant Using Femtosecond Electron Diffraction. *Physical Review Letters*, 96:25901, 2006.

[82] G. Tas and H. J. Maris. Electron Diffusion in Metals Studied by Picosecond Ultrasonics. *Phys. Rev. B*, 49(21):15046, 1994.

8 Appendix

Weighted Volume of a GNR

To calculate the weighted volume V' of a particle's environment, each volume fraction dV is multiplied by the intensity E^2 of the induced electric dipole field. The integrated value is normalized to the intensity of the external electric field E_0^2.

$$V' = \frac{1}{E_0^2} \int_V E^2 \, dV \tag{8.1a}$$

$$E^2 = \left(\frac{p}{4\pi\epsilon_0}\right)^2 \cdot \frac{3\cos^2\theta + 1}{r^6} \tag{8.1b}$$

In spherical coordinates, the integral of equation 8.1a is calculated as follows

$$V' = \int_\theta \int_\phi \int_r \left(\frac{p}{4\pi\epsilon_0}\right)^2 \cdot \frac{3\cos^2\theta + 1}{r^6} r^2 \sin\theta \, dr \, d\phi \, d\theta \tag{8.2a}$$

$$= \left(\frac{p}{4\pi\epsilon_0}\right)^2 \int_\theta \int_\phi \int_r \frac{7\sin\theta + 3\sin(3\theta)}{4r^4} \, dr \, d\phi \, d\theta \tag{8.2b}$$

$$= \left(\frac{p}{4\pi\epsilon_0}\right)^2 \int_\theta \int_\phi -\left(7\sin\theta + 3\sin(3\theta)\right)\left[\frac{1}{12r^3}\right]_r \, d\phi \, d\theta \tag{8.2c}$$

$$= \left(\frac{p}{4\pi\epsilon_0}\right)^2 \int_\theta -\left(7\sin\theta + 3\sin(3\theta)\right)\left[\frac{1}{12r}\right]_r \left[\phi\right]_\phi \, d\theta \tag{8.2d}$$

$$= \left(\frac{p}{4\pi\epsilon_0}\right)^2 \left[7\cos\theta + \cos(3\theta)\right]_\theta \left[\frac{1}{12r^3}\right]_r \left[\phi\right]_\phi \tag{8.2e}$$

Spherical Calotte as Cap of a GNR

To calculate the polymer fraction of the particle's environment, the total weighted volume is split into two parts: V'_{bulk} and V'_{cover}. The first part describes the (infinite) half space of polymer, in which the particle is subsided. The second part is the cover layer, that embeds the particle completely. Table 8.1 lists the intervals of the parameters r, ϕ, and θ that are necessary to determine the value of V'.

In the special case of $R_c = R$, the spherical calotte is a half sphere. So the following

8 Appendix

V'	r	ϕ	θ
V'_{bulk}	$H \to \infty$	$-\cos^{-1}\left(\frac{h}{H}\right) \to \cos^{-1}\left(\frac{h}{H}\right)$	$\sin^{-1}\left(\frac{h}{H}\right) \to \cos^{-1}\left(\frac{\sqrt{R_c^2-R^2}}{H}\right)$
V'_{cover}	$R \to H$	$0 \to 2\pi$	$0 \to \cos^{-1}\left(\frac{\sqrt{R_c^2-R^2}}{H}\right)$
V'_{total}	$R \to \infty$	$0 \to 2\pi$	$0 \to \cos^{-1}\left(\frac{\sqrt{R_c^2-R^2}}{H}\right)$

Table 8.1: Intervals of parameters in spherical coordinates

formulas for V' are also applicable to spherical particles.

$$
\begin{aligned}
V'_{bulk} = \left(\frac{p}{4\pi\epsilon_0}\right)^2 &\left[7\frac{\sqrt{R_c^2-R^2}}{H} - \sin\left(3\sin^{-1}\frac{\sqrt{R_c^2-R^2}}{H}\right) - 7\sqrt{1-\frac{h}{H}}\right. \\
&\left. - \cos\left(3\sin^{-1}\frac{h}{H}\right)\right]\left[-\frac{1}{12H^3}\right]\left[2\cos^{-1}\left(\frac{h}{H}\right)\right]
\end{aligned}
\tag{8.3a}
$$

$$
\begin{aligned}
V'_{cover} = \left(\frac{p}{4\pi\epsilon_0}\right)^2 &\left[7\frac{\sqrt{R_c^2-R^2}}{H} - \sin\left(3\sin^{-1}\frac{\sqrt{R_c^2-R^2}}{H}\right) - 7 - 1\right] \\
&\cdot\left[\frac{1}{12H^3} - \frac{1}{12R^3}\right]\left[2\pi\right]
\end{aligned}
\tag{8.3b}
$$

$$
\begin{aligned}
V'_{total} = \left(\frac{p}{4\pi\epsilon_0}\right)^2 &\left[7\frac{\sqrt{R_c^2-R^2}}{H} - \sin\left(3\sin^{-1}\frac{\sqrt{R_c^2-R^2}}{H}\right) - 7 - 1\right] \\
&\cdot\left[-\frac{1}{12R^3}\right]\left[2\pi\right]
\end{aligned}
\tag{8.3c}
$$

Cylindric Part

In cylindrical coordinates, the integral of equation 8.1a is

$$
V' = \int_z\int_\phi\int_r \left(\frac{p}{4\pi\epsilon_0}\right)^2 \cdot \frac{1}{r^6}r\,\mathrm{d}r\,\mathrm{d}\phi\,\mathrm{d}z
\tag{8.4a}
$$

$$
= \left(\frac{p}{4\pi\epsilon_0}\right)^2 \int_z\int_\phi\int_r \frac{1}{r^5}\,\mathrm{d}r\,\mathrm{d}\phi\,\mathrm{d}z
\tag{8.4b}
$$

$$
= \left(\frac{p}{4\pi\epsilon_0}\right)^2 \left[-\frac{1}{4r^4}\right]_r\left[\phi\right]_\phi\left[z\right]_z
\tag{8.4c}
$$

As described for the spherical caps, the surrounding volume is split into two parts. The intervals are given in table 8.2.

V'	r	ϕ	z
V'_{bulk}	$H \to \infty$	$-\cos^{-1}\left(\frac{h}{H}\right) \to \cos^{-1}\left(\frac{h}{H}\right)$	$0 \to L$
V'_{cover}	$R \to H$	$0 \to 2\pi$	$0 \to L$
V'_{total}	$R \to \infty$	$0 \to 2\pi$	$0 \to L$

Table 8.2: Intervals of parameters in cylindrical coordinates

The values of V' for the cylindrical middle part of the GNRs are

$$
\begin{aligned}
V'_{bulk} &= \left(\frac{p}{4\pi\epsilon_0}\right)^2 \left[\frac{1}{4H^4}\right]\left[2\cos^{-1}\left(\frac{h}{H}\right)\right]\left[L\right] \\
&= \left(\frac{p}{4\pi\epsilon_0}\right)^2 \frac{L}{2H^4}\cos^{-1}\left(\frac{h}{H}\right)
\end{aligned}
\tag{8.5a}
$$

$$
\begin{aligned}
V'_{cover} &= \left(\frac{p}{4\pi\epsilon_0}\right)^2 \left[\frac{1}{4H^4} - \frac{1}{4R^4}\right]\left[2\pi\right]\left[L\right] \\
&= \left(\frac{p}{4\pi\epsilon_0}\right)^2 \frac{\pi L}{2}\left(\frac{1}{H^4} - \frac{1}{R^4}\right)
\end{aligned}
\tag{8.5b}
$$

$$
\begin{aligned}
V'_{total} &= \left(\frac{p}{4\pi\epsilon_0}\right)^2 \left[\frac{1}{4R^4}\right]\left[2\pi\right]\left[L\right] \\
&= \left(\frac{p}{4\pi\epsilon_0}\right)^2 \frac{\pi L}{2R^4}
\end{aligned}
\tag{8.5c}
$$

List of Abbreviations

A - absorption	
AFM	Atomic force microscope
Al	Aluminum (transducer layer)
BBO	Beta-barium borite
CTAB	Cetrimonium bromide
DL	Double layer
FFT	Fast Fourier transform
FWHM	Full width at half maximum
GNR	Gold nanorod
GNS	Gold nanosphere
ITO	Indium tin oxide
LbL	Layer-by-layer
LSMO	Lanthanum strontium manganite ($LaSrMnO_3$)
LSPR	Localized surface plasmon resonance
PAH	Polyallylamine hydrochloride
PEI	Polyethylenimine
PAzo	Poly[1-[4-(3-carboxy-4-hydroxyphenylazo) benzenesulfonamido]-1,2-ethanediyl, sodium salt
PE	Polyelectrolyte
POR	Porphyrin
PSS	Polystyrene sulfonate
R	Reflection
SEM	Scanning electron microscope
SRO	Strontium ruthenate ($SrRuO_3$)
T	Transmission
TDBS	Time-domain Brillouin scattering

Danksagung

Ich bedanke mich bei Professor Matias Bargheer für die vielen Jahre, die ich in seiner Arbeitsgruppe *Ultraschnelle Dynamik kondensierter Materie* wirken und letztendlich promovieren konnte, sowie für die zahlreichen Diskussionen, Ideen und Hilfestellungen.

Professorin Svetlana Santer gilt mein Dank für die Begutachtung dieser Arbeit. Darüber hinaus gab sie mir die Möglichkeit, alle für diese Arbeit nötigen AFM-Messungen in ihrer Laboren durchzuführen.

Professor Andreas Fery danke ich für seine sehr spontane Bereitschaft, diese Arbeit zu begutachten.

Für die Hilfen bei der Probenpräparation und den Messungen im Labor bedanke ich mich bei meinen Kollegen Alexander von Reppert und Elena Pavlenko. Mein besonderer Dank gilt Qianling Cui. Sie stellte die verwendeten Gold-Nanorods her und war mir eine große Hilfe in allen chemischen Fragen. Dr. Carsten Henkel danke ich für seine Unterstützung bei der theoretischen Beschreibung von Gold-Nanopartikeln in einer Polymermatrix.

Die Arbeitsgruppe von Professor Neher stellten mir Spektrometer, Elektronenmikroskop und Aufdampfanlage für die Charakterisierung und Herstellung meiner Proben zur Verfügung. Auch hierfür möchte ich mich ausdrücklich bedanken - besonders bei Frank Jaiser, der mir an den Geräten oft eine Hilfe war.

Darüber hinaus möchte ich mich bei allen Mitgliedern der UDKM bedanken. Obwohl immer wieder neue Kollegen dazu kamen und alte gingen, so blieb das Arbeitsklima stets freundlich und familär.

Mein abschließender Dank gilt Julia, die mir in diesen Tagen mit der kleinen Elisa das größte aller Geschenke gemacht hat. Danke!

Selbstständigkeitserklärung

Hiermit erkläre ich, dass ich die vorliegende Arbeit selbständig und nur unter Verwendung der angegebenen Literatur und Hilfsmittel angefertigt habe. Ich erkläre weiterhin, dass diese Arbeit keiner anderen Fakultät vorgelegt und von keiner anderen Fakultät abgelehnt wurde.

Berlin, 10.04.2015

_____

Steffen Mitzscherling